DOWNSCALING AND VALIDATING SATELLITE-BASED SOIL MOISTURE PRODUCTS OVER THE MAASAI MARA IN KENYA

JING LIU
February 2019

SUPERVISORS:
Dr. Y. Zeng
Prof Dr. Z. Su

ADVISOR:
D.T. Rwasoka (Donald)

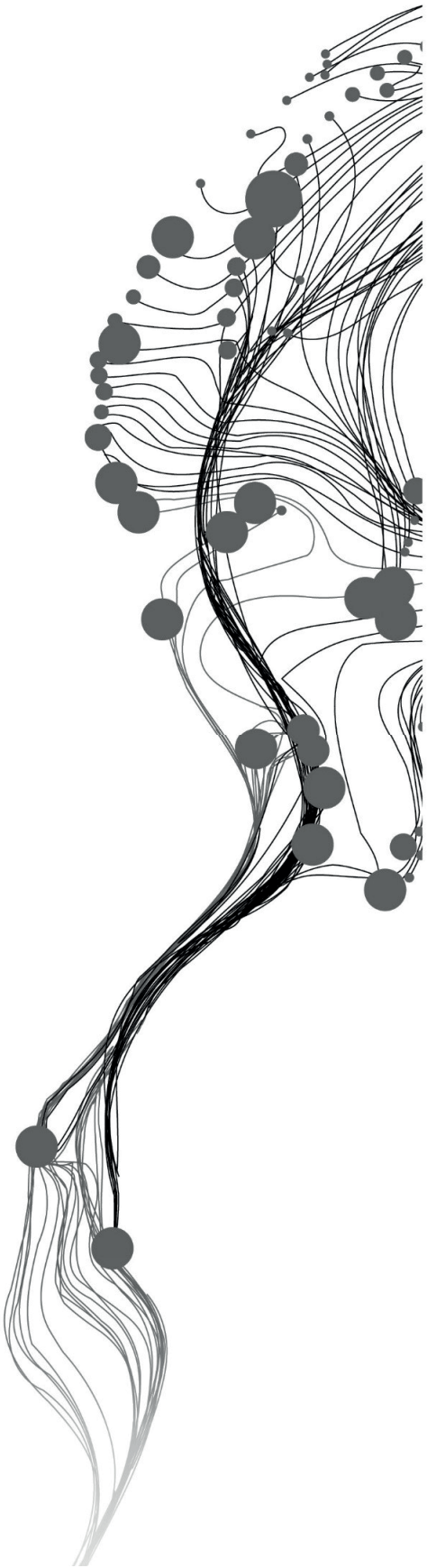

DOWNSCALING AND VALIDATING SATELLITE-BASED SOIL MOISTURE PRODUCTS OVER THE MAASAI MARA IN KENYA

JING LIU
Enschede, The Netherlands, February 2019

Thesis submitted to the Faculty of Geo-Information Science and Earth Observation of the University of Twente in partial fulfilment of the requirements for the degree of Master of Science in Geo-Information Science and Earth Observation.
Specialization: Water Resources and Environmental Management

SUPERVISORS:
Dr. Y. Zeng
Prof Dr. Z. Su

ADVISOR:
D.T. Rwasoka (Donald)

THESIS ASSESSMENT BOARD:
Dr. ir. S. Salama (Chair)
Dr. Carsten Montzka (External Examiner, Forschungszentrum Juelich GmbH)

ABSTRACT

Soil moisture (SM) is an essential environmental and climate variable, which influences energy and water exchanges between the soil and atmosphere. Thus, the estimation of SM is important and yet it is the challenge as well. Satellite remote sensing offers a window of opportunity to provide spatial SM maps. The microwave remote sensing instruments, such as SMAP, SMOS and ASCAT, are widely used to retrieve the SM over a global range. However, most of the microwave products have a relatively coarse resolution (tens of kilometers), which limits their use in regional hydrologic modelling and hazard prediction. Therefore, in this study, a sub-grid SM variability downscaling method was used to downscale SMAP, SMOS and ASCAT products to 1km resolution.

The SM spatial variability is mainly affected by the soil texture heterogeneity, which can be used as a proxy for downscaling. A high-resolution soil map from the Soil Grids was used to provide soil texture information for downscaling. A relationship between the SM variability and the mean SM as a function of the mean and standard deviation of Van Genuchten-Mualem (VGM) model hydraulic parameters was then established. This relationship was used in downscaling. The original and downscaled SM products were validated using both point measurements and areal Cosmic-Ray Neutron Probe (CRNP) estimated SM data over Maasai Mara in Kenya.

Triple collocation was applied to assess the random error among three satellite SM products. SMAP showed the least error followed by ASCAT and SMOS. These three satellite SM products perform differently because of four main factors: sensor, orbit, algorithm and auxiliary data. Moreover, the SMAP and SMOS SM products showed similar SM patterns whilst the ASCAT SM product is mainly dependant on the porosity data. A convex relationship was seen between the mean SM and SM variability and this trend is mainly controlled by the pore size distribution factor of the soil. However, since the study area is relatively homogeneous, SM variability was noted to be very small. Causing the similar SM value between downscaled result and original products. Therefore, the quality of original products has a decisive effect on the downscaled result.

Compared with the point data, the CRNP SM shows wetter trend because its measurement depth is more than 10cm. For original products, the validation result indicates that all three satellites cannot meet the required accuracy of 0.04 cm3 cm-3. ASCAT shows the best performance (ubRMSE=0.061) followed by SMAP (ubRMSE=0.069), and the last one is SMOS (ubRMSE=0.103). In addition, ASCAT performs better over dense vegetation area. While SMAP has less error in the moderate vegetation land cover and bare land. The downscaled result gives better or at least the same performance as original products, but with clearly soil property pattern. Therefore, satellite-based SM products can be downscaled by predicting the sub-grid SM variability within the coarse resolution pixels.

Keywords: Soil moisture, SMAP, SMOS, ASCAT, Soil Grids, soil moisture variability, downscaling

ACKNOWLEDGMENTS

I would like to express my sincere appreciation to my supervisors: Dr. Y. Zeng and Prof Dr. Z. Su for their patient guidance and suggestions.

I would like also to thanks D. T. Rwasoka, for your advice and assistance.

My grateful thanks also extended to Dr.ir. S. Salama and Ir. A.M. van Lieshout, for their advices and comment during the proposal and mid-term presentation.

Also, thanks to Hong Zhao for your help during research.

I want to thank my friends Samuel and Asrat, for their advice and encouragement when I was struggling.

Thanks to all the friends and teachers I met in ITC, leaving an unforgettable memory in my life, I feel very happy to study here.

Finally, sincerely thanks to my parents and sister, without your support and encouragement I cannot get such a fantastic experience in the Netherlands, love you all.

TABLE OF CONTENTS

LIST OF FIGURES

LIST OF TABLES

LIST OF ABBREVIATIONS

ASCAT	Advanced SCATterometer
CRNP	Cosmic-ray Neutron Probe
DCA	Dual Channel Algorithm
DEM	Digital Elevation Model
EASE	Equal-Area Scalable Earth
ECMWF	European Centre for Medium-Range Weather Forecasts
EUMETSAT	European Organization for the Exploitation of Meteorological Satellites
ESA	European Space Agency
FAO	Food and Agriculture Organization
FC	Field Capacity
FDR	Frequency Domain Reflectometry
GMAO	Global Modeling and Assimilation Office
HCC	Hydraulic Conductivity Curve
HPA	High-Power Amplifier
HWSD	Harmonized World Soil Database
IGBP	International Geosphere-Biosphere Programmer
ISRIC	International Soil Reference and Information Centre
LAI	Leaf Area Index
L-MEB	L-band Microwave Emission of the Biosphere
LPRM	Land Parameter Retrieval Algorithm
LST	Land Surface Temperature
LULC	Land Use Land Cover
MERRA	Modern-Era Retrospective analysis for Research and Applications
MODIS	Moderate Resolution Imaging Spectroradiometer
METOP	Meteorological Operational
NASA	National Aeronautics and Space Administration
NDVI	Normalized Difference Vegetation Index
NDWI	Normalized Difference Water Index
NLDAS	North American Land Data Assimilation System
NMDB	Neutron Monitor Database
NSIDC	National Snow and Ice Data Center
PTF	Pedo-transfer Function
RFI	Radio Frequency Interferences
SAR	Synthetic Aperture Radar
SCA	Single Channel Algorithm
SM	Soil Moisture
SMOS	Soil Moisture and Ocean Salinity
SMAP	Soil Moisture Active Passive
TB	Brightness temperature
TDR	Time Domain Reflectometry
TU-Wien	Vienna University of Technology
UMD	University of Maryland
VGM	Van Genuchten-Mualem
WRC	Water Retention Curve

1. INTRODUCTION

1.1. Background

Soil moisture (SM) is an essential variable of the environment, which influences the energy and water exchange between ground and atmosphere (Mccoll et al., 2017; Robinson et al., 2008). Although soil water content only occupies a small part of total water in the earth, it plays an essential role in hydraulic, meteorological, agricultural and water balance application (Ren et al., 2010; Vereecken et al., 2016). SM can be retrieved from point measurement, model assimilation, remote sensing and real measurement from cosmic ray neutron probes (Ahlmer et al., 2018; Montzka et al., 2017; Nasta et al., 2018; Ren et al., 2010). Nowadays, remote sensing instruments, especially microwave remote sensing sensors, are widely used to produce global scaled SM pattern, such as Soil Moisture Active Passive (SMAP) (Colliander et al., 2017), Soil Moisture and Ocean Salinity (SMOS) (Kerr et al., 2012) and Advanced SCATterometer (ASCAT) (Wagner et al., 2010).

Each satellite has its own algorithm and quality, understanding and evaluation of these algorithm and quality are needed before their use. SMAP and SMOS, L-band microwave sensors, primarily measure the brightness temperature (TB) of the land surface. The TB is then converted into soil water content (Miernecki et al., 2014). The lower frequency microwave (1.4GHz) has strong penetrative power which can reduce the effect of vegetation and increase sensitivity of sensor to deeper soil layer (Lannoy et al., 2013). ASCAT uses a C-band (5.7GHz) scatterometer, an active microwave system, to retrieve SM (Fascetti et al., 2016). Evidence shows ASCAT is sensitive to the vegetation dynamics, which may affect its performance (Al-Yaari et al., 2014). Many researches have validated the accuracy of these three satellite products using in-situ measurement network around the world (Colliander et al., 2017; Djamai et al., 2015; Griesfeller et al., 2016). These authors stated that the performance of these satellites has an acceptable result compared to accuracy requirement (0.04 cm3 cm-3). However, the performance may vary with time and place in term of different season, soil texture and land cover.

Currently, most of the satellite SM products have a relatively coarse resolution (tens of kilometer). At this resolution, the products are difficult to use in the regional hydrological model and hazard prediction like flood and drought detection (Peng et al., 2017). Applying a downscaling method to generate high-resolution SM map can be an efficient solution to this challenge. Combining the coarse resolution microwave products with high-resolution mapping sensor, such as synthetic aperture radar (SAR) and optical/thermal microwave is commonly used during downscaling (Srivastava et al., 2013; Velde et al., 2014). Also, some researchers used model-based or geoinformation-based method to downscale coarse SM products. (Kaheil et al., 2008; Mascaro et al., 2010; Ranney et al., 2015). To understand and evaluate the SM variance within the coarse pixels is the essential part for downscaling.

Nowadays, a new downscaling method was developed, which uses high-resolution soil characteristics mapping like soil texture to retrieve the SM variability. It is a function of standard deviation and mean SM based on hydrological model(Montzka et al., 2018). Researches shown that soil texture is a dominant factor of SM spatial change (Lawrence & Hornberger, 2007; Wang et al., 2015). Most papers elaborated that the relationship between mean SM and SM variability should be convex. This means the lower SM variability occurs under relatively wet and dry (Vereecken et al., 2007; Qu et al., 2015). Other research indicated this situation only occurs when the soil texture is fine (Hupet & Vanclooster, 2002). Also, some shown different results, such as that SM variability will increase with the mean SM (Martinez et al., 2013).

In order to disaggregate the SM products to finer resolution based on the SM variability, higher resolution proxy map is needed, such as field capacity, radar backscatter and land surface temperature. (Im et al., 2016; Peng et al., 2015).

Validation of satellite products faces the challenge of scale mismatch, which requires a high density of ground-based measurement network to provide large-scale SM (Crow et al., 2012). To obtain continuous and accurate SM data, Time Domain Reflectometry (TDR) and Frequency Domain Reflectometry (FDR) are most frequently used to detect the soil water content (Lekshmi et al, 2014). However, these SM sensors can only measure a small volume of soil. So, it is difficult to represent the surrounding area especially in the heterogeneous case. This will reduce reliability when relating point-based data to satellite data during validation. Finding the new technique to reduce the scaling gap between satellites and point measurement could be an efficient way to solve this problem.

The Cosmic-Ray Neutron Probe (CRNP) can be used to monitor field-scale average SM, which can then be used for validating satellite SM products (Montzka et al., 2017). This CRNP receives the low-energy neutrons within the soil; the neutrons significantly reduce when meeting hydrogen atoms. Because the most hydrogen atoms are from the water within the ground, the number of neutrons is inversely related to soil water content. Based on this concept the SM can be retrieved from neutron counts(Desilets & Zreda, 2003; Dong et al., 2014; Zreda et al., 2012). However, CRNP is affected by air pressure, air humidity and incoming cosmic-ray flux. To reduce these environmental influences, calibrating the original cosmic-ray counts is required.

The footprint of CRNP is around several hundred meters and up to one meter in the soil, which depends on soil water content (Köhli et al., 2015; Schrön et al., 2017). Compared to point measurements, CRNP provides a relatively larger area of average SM value. Therefore, using CRNP data to validate satellite SM is an efficient way to fill the spatial gap between point measurement and coarse resolution satellite-based SM products (Montzka et al., 2017). However, the measurement depth may not match the satellites products, since CRNP received the neutrons up to one meter. Both point data and CRNP data have their own advantages and disadvantages in this case.

In this study, a method based on soil texture is used to downscale the satellite products from coarse resolution to fine resolution (1 km); then CRNP and point measurement data from Maasai Mara region in Kenya is used to validate both the original and downscaled SM satellite products.

1.2. Research problem

The first problem is based on the performance of satellite SM products used in this research. To evaluate the SM products reliability is the primary challenge before its application. The algorithm and auxiliary data used for each satellite should be clarified in order to understand the mechanism for different satellite SM products. The point SM measurement data is widely used to validate the satellite SM products. However, it can only represent a small volume of water, which is not suitable for an area with high heterogeneity. Therefore, using the field-scaled SM to validate satellite SM products becomes a more efficient way. Instead of point data, CRNP records the average SM over several hundred meters of radius, which can fill the gap between point measurement and satellite pixel-based SM.

Another issue related to the satellite products is that SM retrieved from satellites provide large spatial resolution (tens of kilometers), which makes it difficult to use for catchment scale application. Downscaling the coarse scale SM products to finer resolution is thus a better solution. The essential

concept for downscaling is to understand what the SM variability within the coarse resolution SM pixels. Evidences show that the SM variability mainly depend on the soil texture (Gwak & Kim, 2017; Wang et al., 2015). According to this, soil texture can be investigated as the basis of a spatial downscaling approach for coarse resolution SM products.

1.3. Objective

The main objective of this study is to downscale different satellite SM products (SMAP, SMOS, ASCAT) to fine resolutions (1km) and to validate both original and downscaled satellite products with cosmic-ray neutron probe (CRNP) and point measurement stations.

Specific objectives are:

i. To do the inter-comparison among SMAP, SMOS and ASCAT SM products;
ii. To analyze the relationship between sub-grid SM variability and mean SM;
iii. To downscale different satellite SM products, using sub-grid SM variability;
iv. To validate the original and downscaled satellite SM with CRNP and SM point measurements;

1.4. Research questions

i. Why three SM satellite products have different performances?
ii. What is the relationship between SM variability and mean SM?
iii. What is the effect on the downscaled result when using sub-grid SM variability downscaling method?
iv. What is the performance for each satellite product when compared with ground measurement data?

1.5. Innovation

SM variability is considered to downscale the satellite SM products over Maasai Mara region in Kenya based on Soil Grids dataset.

1.6. Thesis structure

This thesis contains seven chapters. The first chapter illustrates background, research problem, objective and research questions for the thesis and literature review delivered in chapter two. The third chapter gave information about the study area and dataset. Next chapter pointed to the methodology used in this research and followed by the result and discussion part. Chapter six gives the conclusion of this study.

2. LITERATURE REVIEW

Although microwave sensors are suitable for SM detection, the coarse resolution limits the use of SM products under specific aspects, such as small watershed hydrological and agricultural models. Downscaling is an effective way to improve the spatial resolution of the coarse resolution SM products. Based on the previous review by Peng et al. (2017), the downscaling methods can be divided into three classes, first class is that of satellite-based methods; the second one is model-based method, and the last one is the geoinformation-based methods.

The satellite-based method uses the high-resolution image such as SAR and MODIS to merge with coarse resolution SM products (Chakrabarti et al., 2015; Das et al., 2015; Djamai et al., 2016; Hajj et al., 2018; Xu et al., 2018). The model-based method focuses on the statistical model calculation method, and hydrological model assimilation, but in-situ data and bias correction may need in this case (Kaheil et al., 2008; Mascaro et al., 2010). The last way based on the geoinformation like photography and vegetation cover, this method is quite simple, but lots of input data is required to establish the relationship with SM (Ranney et al., 2015).

Recently, the downscaling method still based on the previous concept but with some improvements. High-resolution images from satellites are prevalently used to downscale the coarse resolution products like the Sentinel-1 and MODIS products. Li et al. (2018) provide a model to reduce the effect of vegetation when using SAR data to downscale the SMOS products. More researchers using machine learning (like Markov model, Random forest, Ensemble learning method) and statistical method (like area to area regression kriging method) to combine both MODIS and topographic data in order to improve the performance of downscaled result (Abbaszadeh et al., 2018; Jin, Ge et al., 2018; Kwon et al., 2018; W. Zhao et al., 2018). Except for the satellite-based method, some static parameters also can be used in the SM downscaling. In this research, the soil texture map was used as proxy data to downscale both active and passive products based on Montzka et al., (2018). Other parameters like topographic and land cover are also widely used to downscale coarse resolution products but more plays as the additional factors in satellite-based or model-based method (Fang et al., 2018; Mishra et al., 2018; Montzka et al., 2018).

Table 2.1 Summary of latest SM products downscaling method

Name	Source	Input data	Main methodology	Result
Sentinel-1 based method	(Li et al.,2018)	SMOS, SAR, Crop type, Soil data	The retrieved SM from SAR minimized the error by water-cloud model, then used to downscale the SMOS products	The downscaled result shown similar proformance with original SMOS products and this method can be used in C-band products
Fandom forest method	(Zhao et al.,2018)	SMAP, LST, NDVI, EVI, NDWI, albedo (MODIS), DEM	Using different combination of the input data to establish relationship between SM, then to compare the result	All the combination show slightly better profermance compared with the original products
Ensemble learning method	(Abbaszadeh et al,2018)	SMAP, LST, NDVI (MODIS), Soil data, Precipitation, DEM	The same idea as previous one	The proposed method is better than single form disaggretion approach and it can used in different climite zone
Geographically Weighted Area-to-Area Regression Kriging	(Jin et al.,2018)	AMSR-2, LST, NDVI (MODIS), DEM	Area-to-area regeression kriging method combine the 1km resolution MODIS data to 25km AMSR-2 SM products	This method is better than quadratic regression model and Area-to-point regression kriging method
Gaussian-mixture nonstationary hidden Markov model	(Kwon et al.,2018)	AMSR-2, Precipitation, Temperature	Using the input data to build a set of predictors, then through Markov model and cross validation to give stochastic assimulation of SM	Precipitation is the dominant factor of the SM, however the temperature parameter will the result; This method is better than ordinary regression model
Downscaling by predicting Sub-grid variability	(Montzka et al.,2018)	SMAP, SMOS, ASCAT, Soil map	Statistical method was used to derive the SM variability as a function of mean SM based on Soil Grids map, then the static field capacity (FC) with 1km resolution was used to downscale the corese resolution SM map	Validation shows similar result as original products and this situation could improve by using dynamic proxy data instead of FC
Downscaling using temperature and vegetation data	(Fang et al.,2018)	AMSR-2, NLDAS (SM, temperature), MODIS (NDVI, LST)	More classes of NDVI used to derive the relationship between SM and LST by NLDAS, then coarse resolution AMSR-2 was downscaled by MODIS 1km data	This method had better profermance compare with original one but the precipitation events will effect the downscaling algorithm
Downscaling using TIR surface evaporation data	(Mishra et al.,2018)	SMAP, ALEXI model, NLDAS2 (temperature, SM)	Similar as the DISPATHC method, but actual SEE obtained from TIR-based ALEXI model, the used to downscale different SMAP products	Similar validation result appears for both original and downscaled result, but it is more suitable for bare and medium dense vegetation cover land.

3. STUDY AREA AND DATASET

3.1. Study area

The study area is in Massai Mara National Park in the Kenya, Africa. The Maasai Mara covers around 1510 square kilometers with the elevation range from 1500 to 2180 meters, which is a large wild animal reserve located in Narok County. It is the most northern part of Mara Serengeti ecosystem, which covers an approximate 25000 square kilometers. The Serengeti Park bounds mara Serengeti in Tanzania on the south and Siria cliff on the west. Koyiaki and Olkinyei are pastorally located on the north part of this ecosystem while Siana pastoral on the east (Bhola et al., 2012). The temperature in this area changes from 12 to 30 Celsius, while the average rainfall is 1000 mm per year. Rainy season is from November to May and there are two peaks during this period. The short-time rainfall from November to December and long duration rains stays within March until May. The dry season is from June to October (Ogutu et al., 2011). Considering the terrain type within the study area, almost all covered by the grassland.

Figure 3.1 indicates the location of the study area. The left-upper corner shows the Kenya country boundary and Narok county location; the left-down corner shows the picture of CRNP in Maasai Mara park; the right-side map shows the Narok county map together with CRNP site. The country boundary map can be download from http://www.diva-gis.org/gdata.

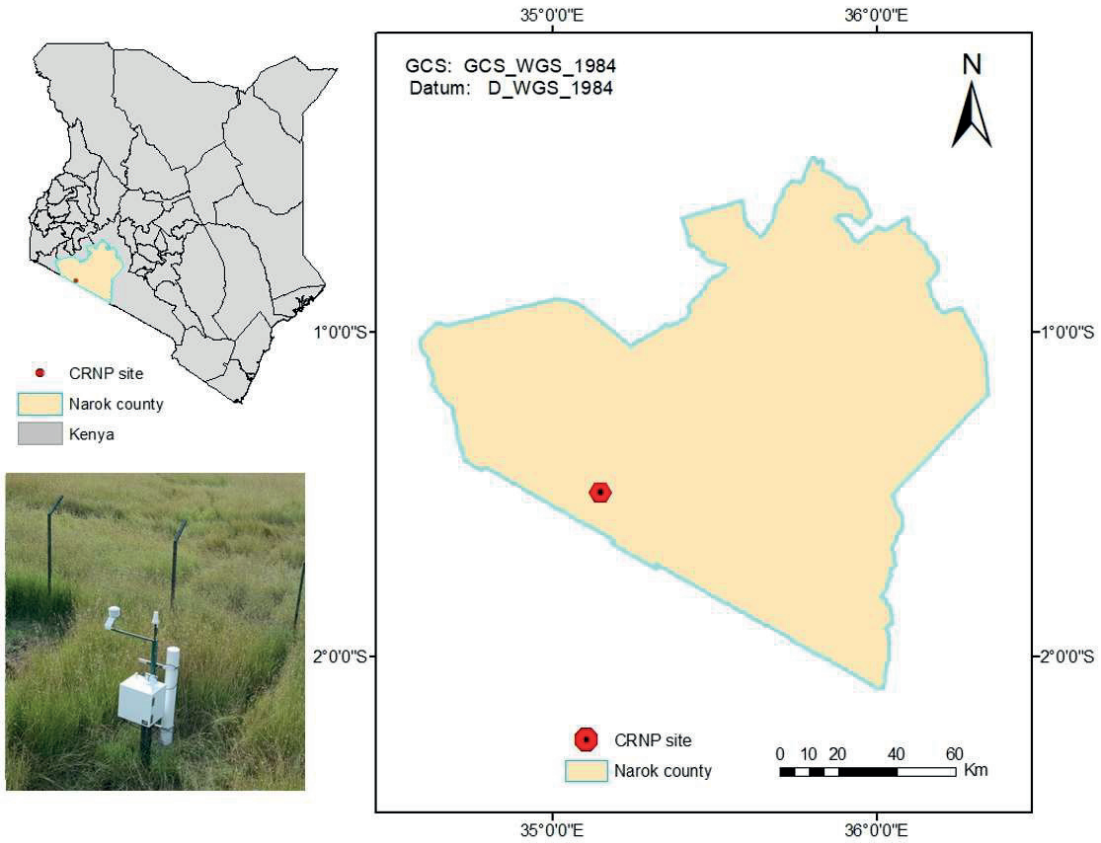

Figure 3.1 Location of Narok country and CRNP site in Kenya

3.2. In-situ SM data

The satellite products were validated against the SM network being developed in the Maasai National Park. The work was began as part of the ongoing ITC Ph.D. research. The network consists of both point SM, soil temperature measurement as well as a Cosmic-Ray Neutron Probe (CRNP). Figure 3.2 shows the current layout of the network used in this thesis, with ten stations and a CRNP site within the study area.

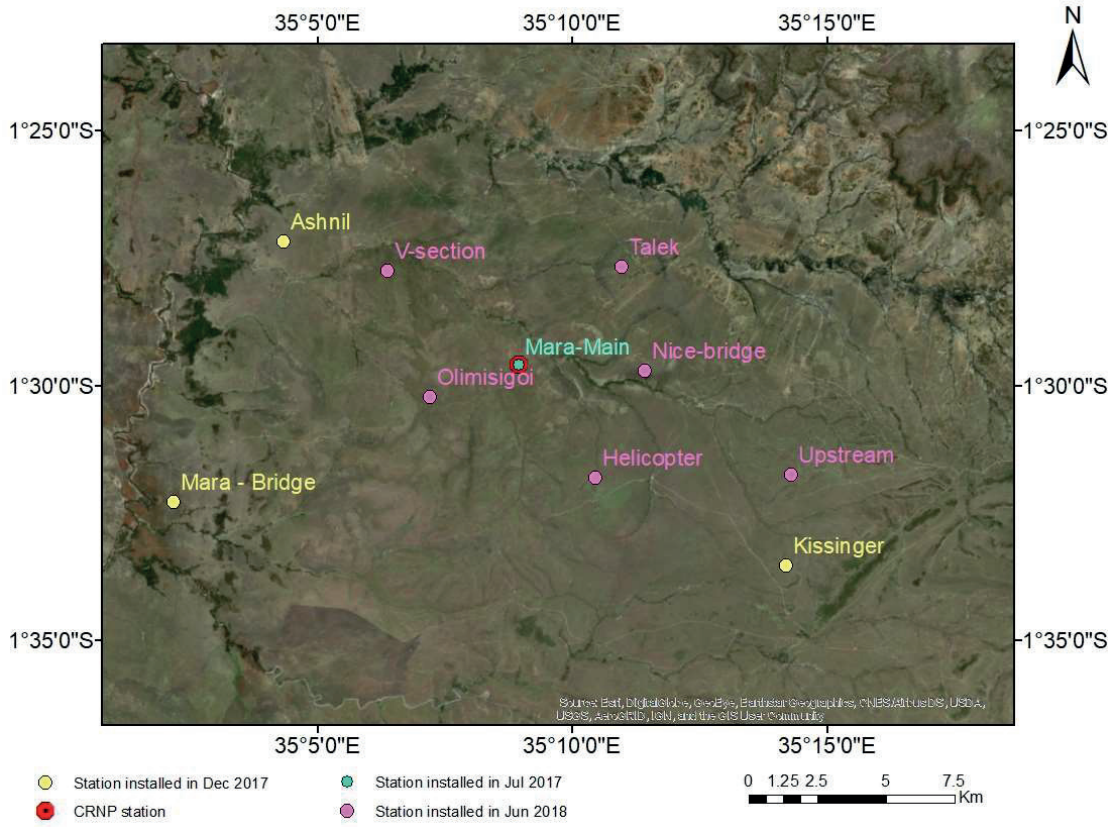

Figure 3.2 The study area of Maasai Mara park based on google earth map

3.2.1. Point measurement data

There are ten SM profile stations in the study area, one of the profiles is located (the light blue dot) just a few meters beside the CRNP; three of them (the yellow dots) have a similar working period with CRNP, and rest six (the pink dots) only have less than six months working period. At each station, SM measurements are done at five different depth, i.e: 5, 10, 20, 40 and 80 cm. Due to the penetration abilities of the microwave, only the top layer field data was used to validation the SM products (Owe & Van De Griend, 1998).

The Decagon 5TM sensor was used to determine the SM in this study. It measures the dielectric constant using frequency domain technology then convert to volumetric SM. Table 3.1 gives the comparison information of ten points measurement stations. The Mara-main station has the longest working period together with CRNP site which was destroyed by warthogs for some period towards the end of 2017. Other three station (Kissinger, Ashnil and Mara-bridge) installed from December 2017. However, the Kissinger had a problem with logger, and warthogs also destroyed the other two stations from June to

July. The rest six stations installed from June 2018, only less than six months data obtained. Almost all stations covered by grassland except Kissinger and Olimisigoi, sparse trees can be found around these two sites.

Table 3.1 Detail information about SM measurement stations.

Name	Latitude	Longitude	Period	Land cover	Data gap
Mara-Main	-1.49332	35.14918	Jul-17 to Dec-18	Grassland	Sep-2017 to Dec-2017
Talek	-1.46117	35.18276	Jun-18 to Dec-18	Grassland	
V-section	-1.46249	35.10616	Jun-18 to Dec-18	Grassland	
Upstream	-1.52919	35.23824	Jun-18 to Dec-18	Grassland	
Kissinger	-1.55889	35.23664	Dec-17 to Dec-18	Isolated shrubs & Grassland	Mar-2018 to May-2108
Helicopter	-1.53042	35.17422	Jun-18 to Dec-18	Grassland	
Olimisigoi	-1.50384	35.12008	Jun-18 to Dec-18	Shrubs and Grass	
Ashnil	-1.45291	35.07215	Dec-17 to Dec-18	Grassland	Jun-2108 to Jul-2108
Nice-bridge	-1.49519	35.19034	Jun-18 to Dec-18	Grassland	
Mara-Bridge	-1.53833	35.03615	Dec-17 toDec-18	Grassland	Jun-2108 to Jul-2108

3.2.2. CRNP data

The calibrated CRNP data for the period from June 2017 to December 2018 was used to validate the satellite SM products. The CRNP is located inside the ITC Mara Main Flux and Soil Moisture station. The coordinates for the CRNP is 01.49335 S and 35.14920 E, and land cover over the footprint of CRNP is largely grasslands. Figure 3.3 shows the ITC Mara Maim station (A) and the CRNP instrument (B).

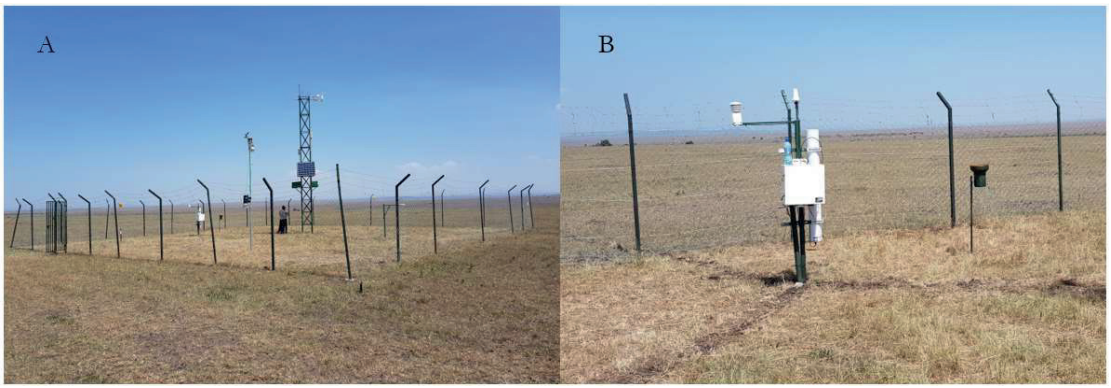

Figure 3.3 ITC Mara Main station (A) and CRNP instrument (B)

The CRNP used a CRS-1000B by HydroInnova. It has a single tube for cosmic-ray sensing. The CRNP is also linked with rain gauge and three SM sensors. The left-top part of Figure 3.3 (B) is a CS215 temperature and relative humidity sensor, in the middle is the satellite antenna. The CRNP powered by a solar panel connected with the eddy covariance tower.

3.3. Spatial products

3.3.1. SMAP

SMAP is one of the first earth observation satellite launched on 31 January 2015 by the National Aeronautics and Space Administration (NASA), which provide different resolution products (36km, 9km, and 3km). SMAP mission combines active radar and passive radiometer using L-band observation to provides a high accuracy of global SM and freeze/thaw state mapping, which can be applied in weather forecasting, hydrological cycle and agriculture (Entekhabi et al., 2010). The low frequencies provide a batch of benefits. Firstly, it will not affect by cloud, providing all-weather sensing; secondly, there is almost no effect from sparse and moderate vegetation land when retrieving the SM because of the high penetrate ability for microwave; thirdly, the property of independent of solar illumination makes it possible to provide observation for both day and night.

In this research, SMAP Enhanced L3 Radiometer global 9 km Equal-Area Scalable Earth Grid (EASE-Grid) SM Product (L3_SMP_E) is used to provide soil water content. This product is available from March 2015 to present, and it can freely be accessed via the National Snow and Ice Data Center (NSIDC) website (https://nsidc.org/data/smap/smap-data.html). The basic algorithm for level 2 and level 3 SMAP SM products is same by using Single channel algorithm (SCA-V) to convert brightness temperature to SM (Entekhabi, Das, & Njoku, 2014). However, for SMAP L3 enhanced products, Backus-Gilbert interpolation method is needed, which can produce the 9 km EASE-grid instead of 36 km. The temporal resolution of L3_SMP_E is one day, with 6:00 am descending and 6:00 pm ascending half-orbit passes. Typically, the product uses input data from 6:00 am in the morning, which helps to reduce the error of output. Because of the less temperature difference between vegetation and soil also the thermal difference among land cover types reaches the minimum (Sm, Sm, & Neill, 2012).

3.3.2. SMOS

Soil Moisture and Ocean Salinity (SMOS) is part of ESA'S earth explore project, which was launched on 2 November 2009. The same as SMAP, SMOS uses L-band microwave observation to receive brightness temperature then convert it to SM, which requires an accuracy of 0.04 m3 m-3 (Al-Yaari et al., 2014). There are two main components for SMOS L3 products. Firstly, state-of-the-art LMEB (L-band microwave emission of the biosphere) model is used as the forward model, which provide the result of microwave emission of varies land covers. The TB calculation based on the forcing auxiliary data and physical parameters. Secondly, the iterative approach used to minimize the cost function between measured and modeled brightness temperature data under a variety of incidence angles. So, except the SM, vegetation parameters also retrieved by finding the best-suited set (Kerr, et al., 2012).

The L3_SM product has an approximate spatial resolution of 25 km with different temporal resolution (daily, 3-day, 10-days and monthly). Daily Level 3 SM product is used in this research. SMOS L3 products used the same physical model as L2, but global products provided instead of swath-based products. The data is freely available through https://smos-diss.eo.esa.int/socat/SMOS_Open. The ascending overpass time for SMOS is 6:00 am and 6:00 pm for descending pass time (Al-Yaari et al., 2014).

3.3.3. ASCAT

ASCAT is a C-band active microwave remote sensing instrument carried by Meteorological Operational (METOP) satellite, which is operated by the European Organization for the Exploitation of Meteorological Satellites (EUMETSAT). ASCAT was designed for measuring wind vector field over the ocean at the beginning. However, evidence showed that it is also suitable for SM retrieval (Wagner et al.,

2013). The frequencies of C-band (5.7 GHz) belong to microwave frequencies, where the dielectric constant for soil and water has a distinguishable difference. For the vegetation-soil condition, the SM retrieval affected by vegetation contents. Therefore, the vegetation correction is arranged before the SM index retrieving. There are also others benefits from ASCAT, for example, it has three different azimuth angles and two separate incidences angle observation system for each pixel, making it possible to correct the effect from vegetation (Wen & Su, 2003).

In this research, the Level 2 SM product is used to obtain SM and can be freely downloaded from https://land.copernicus.vgt.vito.be. It has two different spatial resolution of 50 km (grid spacing 25 km) and 25 km (grid spacing 12.5 km), while 12.5 km spatial sampling product was used in this study. A change detection method developed by Vienna University of Technology (TU-Wien) was used to retrieve the soil water index of the topsoil layer, ranging between 0 (dry) and 100 (wet). The concept for this method is from the ERS mission, then transferred to ASCAT (Brocca et al., 2017). There are some assumptions for ASCAT, firstly, a linear relationship between backscattering coefficient (σ^0) and SM contents and the σ^0 depends on the incidence angle; then, surface roughness and land cover are stable over the time and finally, vegetation has a seasonal influence where the correction is needed.

The output of SMI needs to be converted to volumetric SM unit (cm3 cm-3) by multiplying with global porosity database (Wagner et al., 2010). Figure 3.4 gives the porosity map used for ASCAT within the study area. This map was downloaded from the ESA CCI website for the global range with a spatial resolution of 0.25 degree, then resampled to the same spatial resolution as ASCAT products.

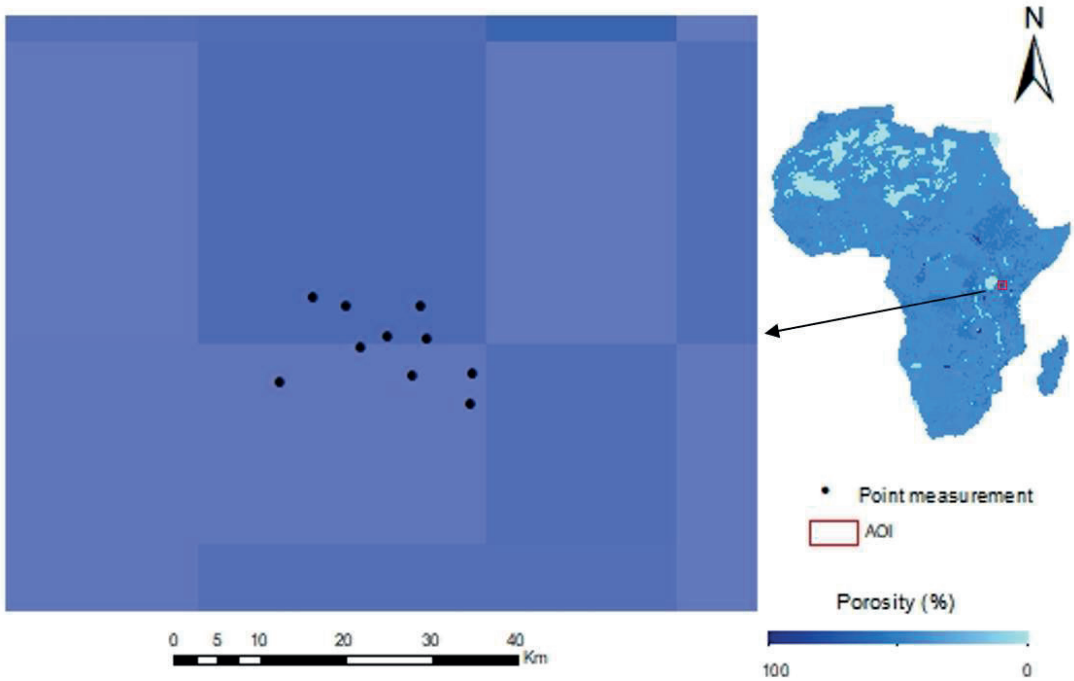

Figure 3.4 Porosity map used in the study area

Table 3.2 Comparison of three satellites

Products	SMAP	SMOS	ASCAT
Platform	SMAP	SMOS	METOP
Lifetime	2015-3-31 to present	2009-11 to present	2016-1-1 to present
Channel	1.4 GHz	1.4 GHz	5.2 GHz
Sensor	SMAP L-band radiometer	SMOS L-band radiometer	Microwave radar
Equatorial crossing time	Descending	Ascending	Descending
Spatial resolution	9 km	25 km	12.5 km
Temporal resolution	Daily	Daily	Daily

Figure 3.5 illustrates the location of three satellite pixels and the point measurement. All the points located inside one SMOS pixel (pick box) which has the biggest spatial resolution of 25km compare with the other two satellites. The yellow and green boxes are coarse pixel for ASCAT (12.5 km) and SMAP (9km) respectively. And the red box is the study area of this research.

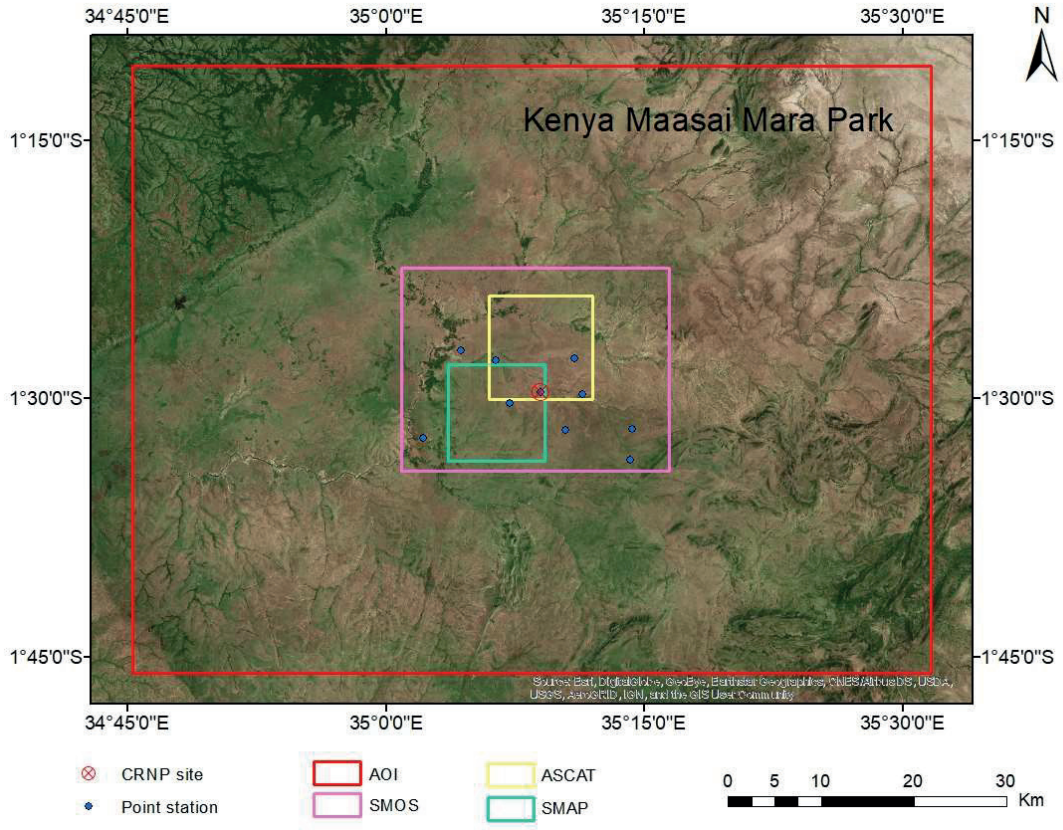

Figure 3.5 Points measurement and satellite pixel locations in Maasai Mara Park; the red box is the study area.

3.3.4. Soil Grids

Gridded soil data can be used to understand the SM properties over an area and the International Soil Reference and Information Centre (ISRIC) provides two versions of Soil Grids, which can be freely downloaded from http://data.isric.org/. The first version has a resolution of 1 km and 250 m for the second one; both versions products provide soil profile dataset over six different depths from 0 to 200 cm

(Jin et al., 2018). The gridded soil dataset contains different soil properties like soil texture (%), bulk density (kg m-3), sand and clay fractions (%), soil pH, soil organic carbon (g kg-1), cation exchange capacity (cmol/kg-1) and depth to bedrock (cm) (Hengl et al., 2014). In this research, five factors (clay, silt and sand fraction, bulk density and soil organic carbon) of 1 km spatial resolution were used to estimate the hydraulic parameters of the VGM model (show in Figure 3.6).

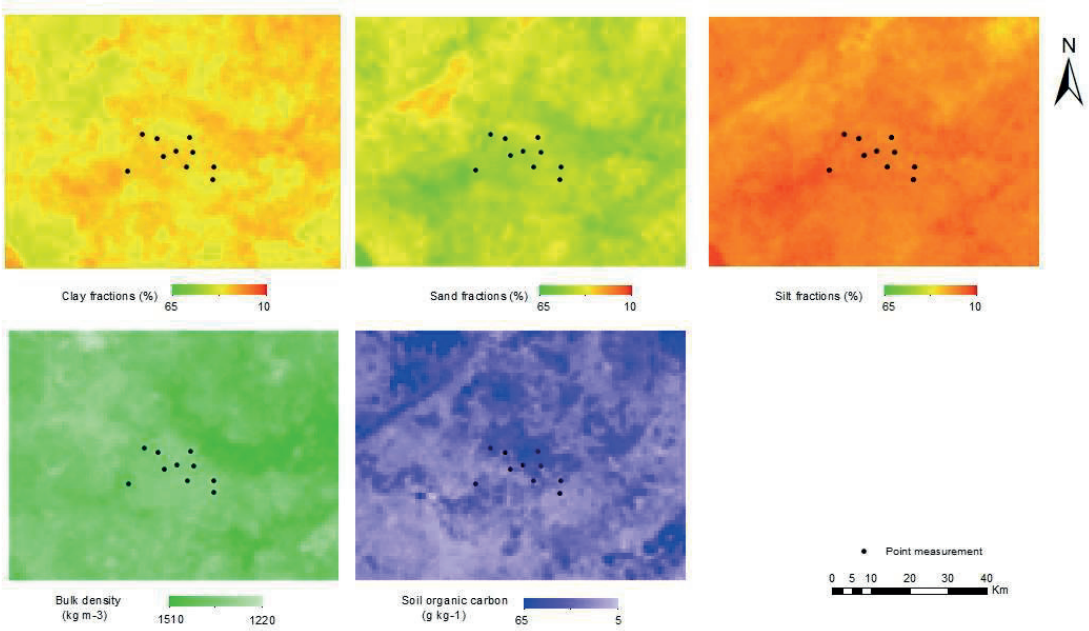

Figure 3.6 Soil grids maps

4. RESEARCH METHODOLOGY

4.1. Overall methodology flowchart

Figure 4.1 summarizes the main idea of the methodology used in this study. Soil information map is download from ISRIC website which contains the clay, silt and sand fraction, bulk density value, soil organic carbon content. Hydraulic parameters for VGM model are derived from SM information and then used to obtain the relationship between mean SM and SM variability based on the closed-form expression. Next, SM variability of each coarse scale pixel can be calculated. Then, field capacity at 1km spatial resolution can be used as proxy data for downscaling. The last procedure is to validate different satellite SM products using CRNP and point measurement SM data.

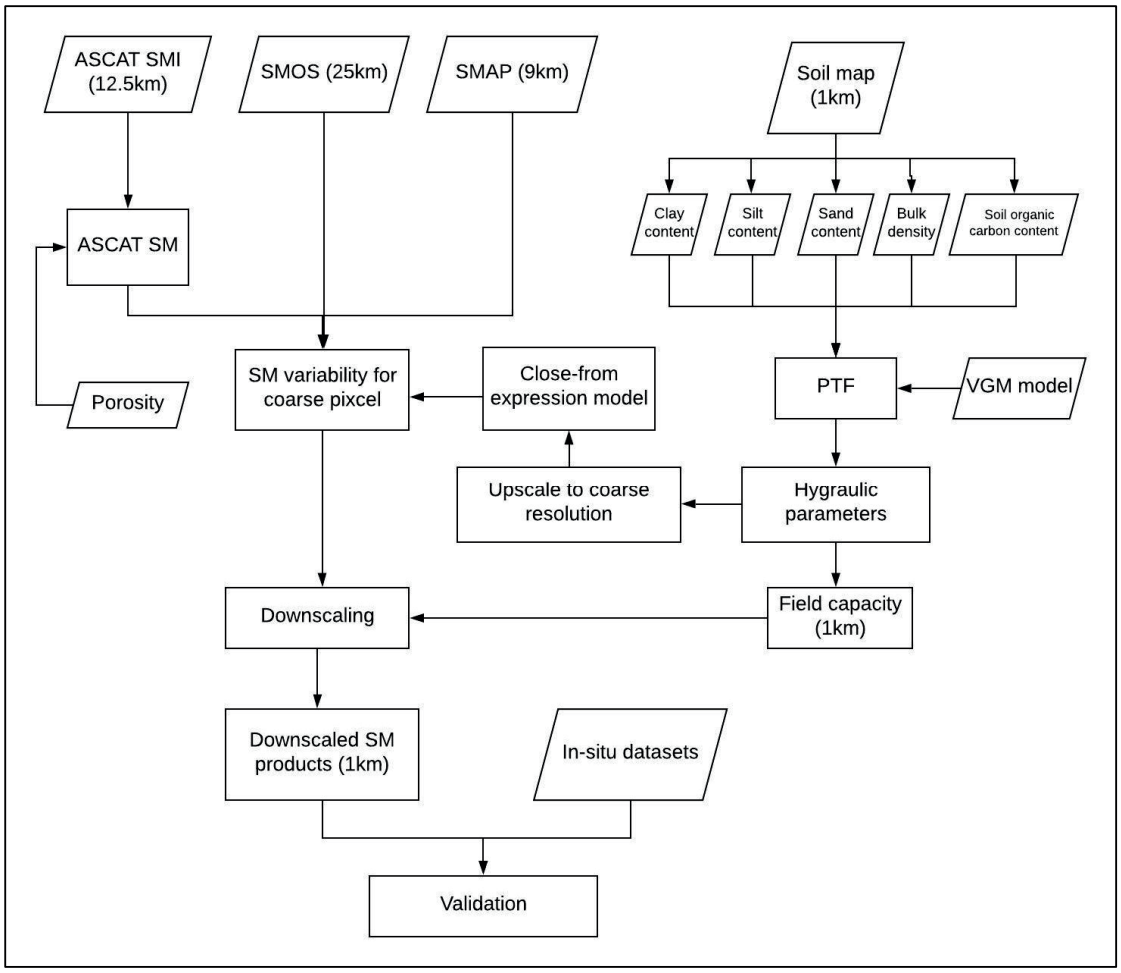

Figure 4.1 Flowchart for methodology followed in this study

4.2. Pre-processing for SM retrieved from CRNP counts

In this research, the calibrated CRNP data is used. The calibration part has a short description as below, which indicates the N0 method for retrieving the SM from CRNP counts.

4.2.1. Correction of CRNP counts

The CRNP counts are affected by air pressure, air humidity and incoming cosmic-ray flux. It is necessary to correct the raw counts data before retrieving the SM. Different influence factors are used to correct initial counts (Desilets & Zreda, 2003; Zreda et al., 2012).

$$N_c = N_{raw} \times F_i \times F_p \times F_w \quad 4\text{-}1$$

Where N_{raw} is the original neutron counts (cph); N_c is the corrected neutron counts; F_i is the incoming cosmic-ray flux correction factor; F_p is the air pressure correction factor; F_w is the atmosphere water vapor corrector factor.

The incoming ray correction factor was calculated based on the Neutron data recorded in Namibia, Africa albeit most corrections being with neutron monitor data from JUNG (jungfraujoch). This was done because Namiba was considered to closer to the Mara and Cut-off Rigidity of the site was closer to that of the site. Absolute humidity was calculated from 2 metre relative humidity data from a CS215 sensor that is part of the Cosmic Ray system.

4.2.2. SM retrieved from CRNP counts using N_0 method

There is a simplified method to convert CRNP counts to SM based on shape-defining function from MCNPX model (Desilets et al., 2010). The raw CRNP counts data can be seen in Figure 4.2.

$$\theta(N) = \frac{a_0}{\left(\frac{N}{N_0}\right) - a_1} - a_2 \quad 4\text{-}2$$

Where θ (N) is gravimetric water content (kg kg-1); N is corrected CRNP counts (cph); N_0 is the counting rate over dry soil under the same condition (cph); αi are fitting parameters. These parameters can be determined as 0.0808, 0.372 and 0.115 respectively for a genetic silica soil matrix.

$$\theta(N) = \theta_p + \theta_{or} \quad 4\text{-}3$$

Where θ_p is the gravimetric water content (kg kg-1) and θ_{or} is the organic water content (kg kg-1).

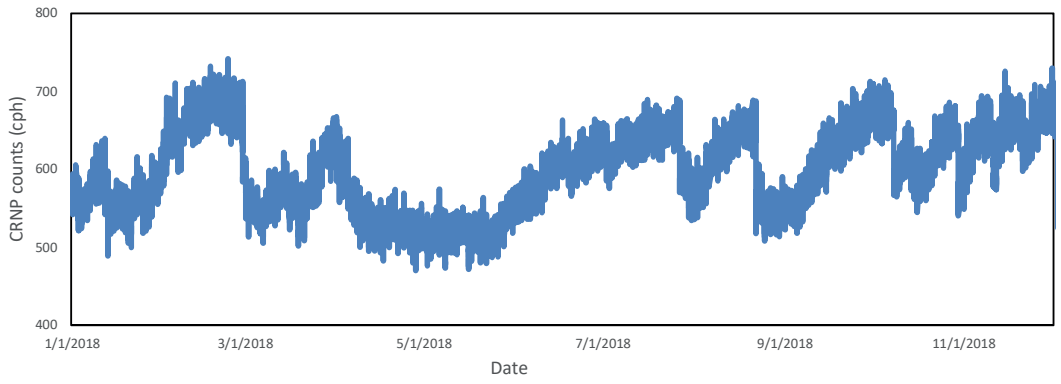

Figure 4.2 CRNP calibrated counts time series plot

Gravimetric soil moisture was obtained 144 core rings sampled around the CRNP. The samples were taken using four concentric rings around the CRNP at distances of: 10, 25, 75, and 175 metres, and at the following degree angles: 0, 60, 120, 180, and 240. Six (6) samples were collected at each sampling point, over the 0-30 cm depth region. Samples were taken for each 5 cm region of the sampling depth. Because the CRNP has been shown to have varying spatial sensitivities, the calibration was done using both depth

and distance weighting (Köhli et al., 2015; Schrön et al., 2017). Samples further away had a lesser weight than those closer to the cosmic ray.

Considering that the CRNP is sensitive to all hydrogen pools in the sampling volume (Desilets et al., 2010), there is need to account for other hydrogen pools that do not 'evaporate' at 105 degree Celsius used in the gravimetric soil moisture method. Thus, soil organic matter and root biomass had to be accounted for. They were accounted for as in other work on CNRP calibration (Hawdon, 2014; International Atomic Energy Agency., 2017; Baatz et al., 2007). Lab measured Total Organic Carbon (TOC) at each sampling point was first converted to Soil Organic Matter (SOM) using the often-used coefficient of 1.724, although there is debate around the validity of this conversion coefficient. The SOM was then scaled to the volume of the soil in the sampling ring because it was lab determined as grammes of TOC per 100 grammes of soil. The SOM was then converted to the water equivalent using the standard conversion factor of 0.556 (Hawdon, 2014; Baatz et al., 2014). The water equivalent due to SOM and Root Biomass as added to the gravimetric soil moisture in the calibration process. Other calibration approaches are being investigated, but here data from this No method was used.

4.3. Soil texture

The soil texture triangle is used to define different soil types based on clay, silt and sand content in the study area. The soil information for different in-situ points can be obtained from Soil Grids website. Based on the Soil Grids information, ten measurement points belongs to sandy clay loam and clay loam. Figure 4.3 illustrating the difference in soil texture within the study area. Left one shows the different soil types of the whole study area with the resolution of 1km; right one gives the ten stations information.

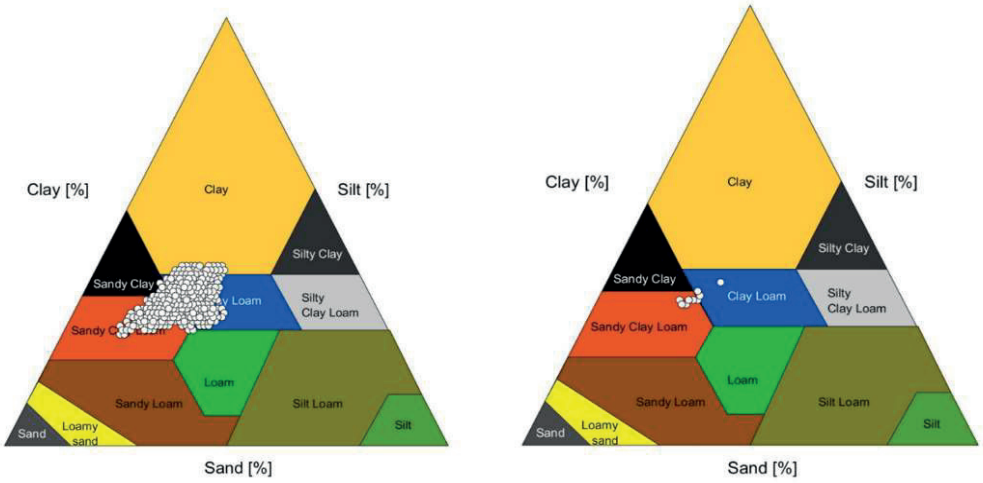

Figure 4.3 Soil texture triangles for the whole study are and station sites

4.4. Pedotransfer function for VGM model

The water retention curve (WRC) is an important input for the hydraulic model, but it is difficult to measure. There are some empirical equations, which can be used to present the WRC, such as Brooks-Corey or Gardner-Russo model. In this research, the Van Genuchten-Mualem model (VGM) is used, which shows a better result compared with other models (Schaap & van Genuchten, 2006; Zhao et al., 2018). The pedotransfer function (PTFs) is often used to transfer soil survey information such as sand, silt, clay percentage and bulk density to soil hydraulic parameters. In this study the VGM model is used to predict the WRC and hydraulic conductivity curve (HCC), so parameters in this model ($\alpha, n, \theta_s, \theta_r, K_s, L$)

need to be solved based on PTF. There are several well-known PTFs (Rawls & Brakensiek, 1985; Vereencken, 1988; Wösten et al., 1999), based on statistical analysis by Wagner et al (2001) the PTF developed by Wösten shows better proformance, which is used in this study.

$$\theta_s = 0.7919 + 0.001691(C) - 0.29619(BD) - 0.000001491(S)^2 + 0.0000821(OM)^2 + 0.02427/(C) + 0.01113/(S) + 0.01472\ln(S) - 0.0000733(OM)(C) - 0.000619(BD)(C) - 0.001183(BD)(OM) - 0.0001664(topsoil)(S) \quad 4\text{-}4$$

$$\theta_r = 0 \quad 4\text{-}5$$

$$\alpha = \exp[-14.96 + 0.03135(C) + 0.0351(S) + 0.646(OM) + 15.29(BD) - 0192(topsoil) - 4.671(BD)^2 - 0.000781(C)^2 - 0.00687(OM)^2 + 0.0449/(OM) + 0.0663\ln(S) + 0.1482\ln(OM) - 0.04546(BD)(S) - 0.4852(BD)(OM) + 0.00673(topsoil)(C)] \quad 4\text{-}6$$

$$n = 1.0 + \exp[-25.23 - 0.02195(C) + 0.0074(S) - 0.1940(OM) + 45.4(BD) - 7.24(BD)^2 + 0.0003658(C)^2 + 0.002885(OM)^2 - 12.81/(BD) - 0.1524/(S) - 0.01598/(OM) - 0.2876\ln(S) - 0.0709\ln(OM) - 44.6\ln(BD) - 0.02264(BD)(C) + 0.0896(BD)(OM) + 0.00718(topsoil)(C)] \quad 4\text{-}7$$

$$K_S = \exp[7.75 + 0.0352(S) + 0.93(topsoil) - 0.976(BD)^2 - 0.000484(C)^2 - 0.000322(S)^2 + 0.001/(S) - 0.0748/(OM) - 0.643\ln(S) - 0.01398(BD)(C) - 0.1673(BD)(OM) + 0.02986(topsoil)(C) - 0.03305(topsoil)(S)] \quad 4\text{-}8$$

Where C is the percentage of clay (%); S is the percentage of silt (%); OM is the percentage organic matter (%); BD is the bulk density (g/cm2); topsoil is qualitative variable has the value of 1 (depth 0-30 cm) or 0 (depth >30 cm); θ_s is the saturated water content (cm3 cm-3); θ_r is the residual water content (cm3 cm-3); α is air entry parameter (cm-1); K_s is the saturated hydraulic conductivity (cm d-1) and n (-) is the pore size distribution parameter.

4.5. Estimation of SM variability

The concept for this method is to describe how SM variability depends on mean SM using stochastic analysis based on VGM model (Qu et al., 2015). From the VGM model, water retention curve (WRC) can be written as:

$$S_e = \frac{1}{(1 + (\alpha|h|)^n)^m}, h < 0 \quad 4\text{-}9$$

$$\theta = \theta_r + S_e(\theta_s + \theta_r) \quad 4\text{-}10$$

$$m = 1 - \frac{1}{n} \quad 4\text{-}11$$

Where S_e is the effective saturation (-); h is the pressure head (cm); θ_r is the residual water content (cm3 cm-3); θ_s is the saturated water content (cm3 cm-3); θ is the actual SM (cm3 cm-3); α is air entry parameter (cm-1) and n (-) is the pore size distribution parameter.

And the hydraulic conductivity curve (HCC):

$$K(S_e) = K_s S_e^L \left[1 - \left(1 - S_e^{\frac{1}{m}}\right)^m\right]^2, h < 0 \quad 4\text{-}12$$

Where K_s is the saturated hydraulic conductivity (cm d-1); K is the hydraulic conductivity (cm d-1); L is the pore connectivity parameter.

The method proposed by Qu et al., (2015) is based on a stochastic analysis of steady-state unsaturated flow proposed by Zhang et al., (1998). Zhang et al., (1998) described the constitutive relationship of both Brooks-Corey and Gardner-Russo model to derive the relationship between SM and hydraulic head. Based on this, Qu et al. applied VGM model to establish the relationship between mean SM and SM variability as a function of the hydraulic parameters. From the beginning, a second-order stationary stochastic process assumed by different variables and hydraulic parameters and these parameters can be decomposed into the mean and perturbations. Based on this, the mean and perturbation of SM can be written as a function of all VGM parameters and a linear relationship can be found between SM perturbation and the perturbation of VGM parameters. After calculating the covariance between different parameters and assuming the VGM parameters are not correlated, which can significantly simplify the intermediate computing process. The final relationship between SM variability and VGM parameters obtained by substituting the covariance of pressure head and hydraulic parameters. Equations are shown below.

$$\sigma_\theta^2 = b_0^2 \left\{ b_1^2\sigma_\alpha^2 + b_2^2 \left[\frac{\sigma_f^2\rho_f}{(1+\alpha_2\rho_f)\alpha_2} + \frac{\alpha_1\sigma_\alpha^2\rho_\alpha}{(1+\alpha_2\rho_\alpha)\alpha_2} + \frac{\alpha_3\sigma_n^2\rho_n}{(1+\alpha_2\rho_n)\alpha_2}\right] + b_3^2\sigma_n^2 + b_4^2\sigma_{\theta_s}^2 + 2b_1b_2\left(-\frac{\alpha_1\sigma_\alpha^2\rho_\alpha}{1+\alpha_2\rho_\alpha}\right) + 2b_2b_3\left(-\frac{\alpha_3\sigma_n^2\rho_n}{1+\alpha_2\rho_n}\right)\right\} \quad 4\text{-}13$$

Where ρ is the vertical correlation length of the respective parameters; a_i *and* b_i coefficients are obtained from the mean value of different parameters.

$$a_1 = \frac{\left(\frac{5}{2} - \frac{1}{2\overline{n}}\right)(\overline{\alpha}\overline{h})^{\overline{n}}}{1 + (\overline{\alpha}\overline{h})^{\overline{n}}} \frac{\overline{n}}{\overline{\alpha}} \quad 4\text{-}14$$

$$a_2 = \frac{\left(\frac{5}{2} - \frac{1}{2\overline{n}}\right)(\overline{\alpha}\overline{h})^{\overline{n}}}{1 + (\overline{\alpha}\overline{h})^{\overline{n}}} \frac{\overline{n}}{\overline{h}} \quad 4\text{-}15$$

$$a_3 = \frac{\left(\frac{5}{2} - \frac{1}{2\overline{n}}\right)(\overline{\alpha}\overline{h})^{\overline{n}}}{1 + (\overline{\alpha}\overline{h})^{\overline{n}}} \ln(\overline{\alpha}\overline{h}) + \frac{\ln(1 + (\overline{\alpha}\overline{h})^{\overline{n}})}{2\overline{n}^2} - \frac{2}{\overline{n}^2 - \overline{n}} \quad 4\text{-}16$$

$$b_0 = (\overline{\theta_s} - \overline{\theta_r})\left\{\frac{\overline{\alpha}\overline{h}}{[1 + (\overline{\alpha}\overline{h})^{\overline{n}}](\overline{\alpha}\overline{h})^{\overline{n}}\overline{n}}\right\} \quad 4\text{-}17$$

$$b_1 = \frac{\overline{n}\,(\overline{\alpha}\overline{h})^{\overline{n}} + 1 - \overline{n}}{\overline{\alpha}} - \frac{[\,\overline{n}\,(\overline{\alpha}\overline{h})^{\overline{n}} + 1](\overline{\alpha}\overline{h})^{\overline{n}}}{1 + (\overline{\alpha}\overline{h})^{\overline{n}}} \frac{\overline{n}}{\overline{\alpha}} \quad 4\text{-}18$$

$$b_2 = \frac{\overline{n}\,(\overline{\alpha}\overline{h})^{\overline{n}} + 1 - \overline{n}}{\overline{h}} - \frac{[\,\overline{n}\,(\overline{\alpha}\overline{h})^{\overline{n}} + 1](\overline{\alpha}\overline{h})^{\overline{n}}}{1 + (\overline{\alpha}\overline{h})^{\overline{n}}} \frac{\overline{n}}{\overline{h}} \quad 4\text{-}19$$

$$b_3 = -\frac{1}{\overline{n}} - \ln(\overline{\alpha}\overline{h}) - \ln(\overline{\alpha}\overline{h})\frac{[\,\overline{n}\,(\overline{\alpha}\overline{h})^{\overline{n}} + 1](\overline{\alpha}\overline{h})^{\overline{n}}}{1 + (\overline{\alpha}\overline{h})^{\overline{n}}} \quad 4\text{-}20$$

$$b_4 = \overline{n}\,(\overline{\alpha}\overline{h})^{\overline{n}} + 1 \quad 4\text{-}21$$

$$f = \ln K_s \quad 4\text{-}22$$

This closed-form expression established a relationship between SM variability and mean SM, mean hydraulic parameters, the standard deviation of hydraulic parameters and the vertical correlation length for the VGM model. The relationship between average pressure head and mean SM value show as below.

$$\overline{\theta} = (\overline{\theta_s} - \overline{\theta_r})\left(\frac{\overline{\alpha}\overline{h}}{1 + (\overline{\alpha}\overline{h})^{\overline{n}}}\right)\left(\frac{\overline{n}\,(\overline{\alpha}\overline{h})^{\overline{n}} + 1}{\overline{n}\,(\overline{\alpha}\overline{h})^{\overline{n}}}\right) + \overline{\theta_r} \quad 4\text{-}23$$

The coarse scale parameter $\overline{\theta_s}, \overline{\theta_r}, \overline{\alpha}\ and\ \overline{h}$ are obtained by fitting the minimum sum of square of all sub-grids' pixel value within the coarse pixel.

4.6. Downscaling satellite products from sub-grid SM variability

The $\sigma_\theta(\overline{\theta})$ function can be used to retrieve the SM variability at each grid cell. In addition, to downscale the coarse resolution satellite SM products, proxy data such as surface temperature and radar backscatter can be used (Hajj et al., 2018; Xu et al., 2018). The proxy data has a higher resolution, which need to be normalized before using. Then, the result combined with the SM variability is used to downscale coarse SM products (Montzka et al., 2018). The disaggregation method can be performed as below.

$$\widetilde{\theta_{i,J}} = \overline{\theta} + \sigma_\theta(\overline{\theta})\frac{P_{i,j} - \overline{P}}{\sigma_p} \quad 4\text{-}24$$

Where $\widetilde{\theta_{i,J}}$ stands for SM value at the fine scale resolution; $\overline{\theta}$ is the average value within the coarse pixel; $\sigma_\theta(\overline{\theta})$ is the soil variability at the specific mean SM condition; $P_{i,j}$ is the proxy data at fine resolution grid, which also shows the location of this fine sub-grid; $\overline{P}$ is the mean value of proxy date; σ_p representative the standard deviation of the proxy. The resolution of proxy date is similar with the sub-grid soil properties which are used to retrieve SM variability.

4.7. Quantification of errors

4.7.1. Standard validation

The downscaled satellite SM products were validated against cosmic-ray neutron probe and SM station data to evaluate the performance. The mean bias, root mean square error (RMSE), unbiased root mean square error (ubRMSE) and Pearson correlation coefficient (R) were computed.

The bias ($-\infty \sim +\infty$) measures the average difference between satellite and in-situ data. However, the negative and positive error may offset in this case. RMSE (0~$+\infty$)shows the spatial variance of SM difference between two datasets while ubRMSE (0~$+\infty$) indicated the unbiased spatial variance of SM difference. R (-1~1) illustrates the linear correlation between two datasets.

$$Bias = \frac{\sum_{i=1}^{N}(\theta_{c,i} - \theta_{s,i})}{N} \quad 4\text{-}25$$

$$RMSE = \sqrt{\frac{\sum_{i=1}^{N}\left(\theta_{c,i} - \theta_{s,i}\right)^2}{N}} \quad 4\text{-}26$$

$$ubRMSE = \sqrt{\frac{\sum_{i=1}^{N}((\theta_{c,i} - Bias) - \theta_{s,i})^2}{N}} \quad 4\text{-}27$$

$$\mathrm{R} = \frac{\mathrm{N}\sum(\theta_{s,i}\theta_{c,i}) - \sum\theta_{s,i}\sum\theta_{c,i}}{\left[N\sum({\theta_{s,i}}^2 - \left(\sum(\theta_{s,i})\right)^2\right]\left[N\sum{\theta_{c,i}}^2 - \left(\sum X\theta_{c,i}\right)^2\right]} \quad 4\text{-}28$$

Where $\theta_{s,i}$ (cm3/cm3) stands the satellites data; $\theta_{c,i}$ (cm3/cm3) means the in-situ measurement data; N is the number of datasets.

4.7.2. Triple collocation (TC)

The triple collocation (TC) method was used here to understand the random error of these SM satellites products. This method was invented by Stoffelen (1998), and initially used as wind speed error estimation. Subsequently, it successfully applied to analyze the random error and uncertainty among SM products without the true dataset (Chen et al., 2018; Scipal et al., 2010). Assuming the linear relationship between SM and observation dataset: $\theta_i = \alpha_i + \beta_i\theta_T + \varepsilon_i$, θ_T stands for the true SM value while θ_i $(\mathrm{i} = \mathrm{X,Y,Z})$ indicates the triplets; $\alpha_i\ and\ \beta_i$ are additive and multiplicative bias; ε_i represents the zero-mean random error of each triplets (Gruber et al., 2016). In this study, TC analysis was done among SMAP (X), SMOS (Y) and ASCAT (Z) products, and taking SMAP as the reference dataset, which means the α_X=0 and β_X =1. The error variance can be presents as:

$$\begin{aligned}\sigma_{\varepsilon x}^2 &= \sigma_X - \frac{\sigma_{XY}\sigma_{XZ}}{\sigma_{YZ}}\\ \sigma_{\varepsilon y}^2 &= \sigma_Y - \frac{\sigma_{XY}\sigma_{YZ}}{\sigma_{XZ}}\\ \sigma_{\varepsilon z}^2 &= \sigma_Z - \frac{\sigma_{YZ}\sigma_{XZ}}{\sigma_{XY}}\end{aligned} \quad 4\text{-}29$$

Where $\sigma_X, \sigma_Y\ and\ \sigma_Z$ are data variance; $\sigma_{XY}, \sigma_{XZ}\ and\ \sigma_{YZ}$ are data covariance; $\sigma_{\varepsilon x}, \sigma_{\varepsilon y}\ and\ \sigma_{\varepsilon z}$ are error variance. Another performance metrics used is the signal-to-noise ratio (SNR). It measures the ratio between signal power and noise power. The SNR was formulated as:

$$\begin{aligned}SNR_X &= -10\log(\frac{\sigma_X\sigma_{YZ}}{\sigma_{XY}\sigma_{XZ}} - 1)\\ SNR_Y &= -10\log(\frac{\sigma_Y\sigma_{XZ}}{\sigma_{XY}\sigma_{YZ}} - 1)\\ SNR_Z &= -10\log(\frac{\sigma_Z\sigma_{XY}}{\sigma_{YZ}\sigma_{XZ}} - 1)\end{aligned} \quad 4\text{-}30$$

This is a logarithmic measure and returns the unit of decibel (dB). When SNR is equal to 0, it means the signal variance is equal to the noise variance. And each ±3 dB indicate twice or half signal variance of noise variance.

5. RESULT AND DISCUSSION

5.1. Inter-comparison of satellite products

5.1.1. Descriptive inter-comparison

It is considered that radiometer brightness temperature and radar backscatter linked in some aspects, for example, both are sensitive to the land cover and surface roughness change (Pierdicca et al., 2013). Many factors influence the quality of the SM products and these parameters can be classified. Some parameters change through the time, for example, the land surface temperature, soil ice fraction and vegetation water content; some may change through the spatial distribution like DEM. Furthermore, parameters can change through both temporally and spatially such as the land cover condition. Based on the Dorigo et al. (2017) research, four main factors (sensor, orbit, algorithm and environmenral) may cause the error of satellite products for both active and passive. These factors can be used to do the inter-comparison among three satellite products. Table 5.1 gives an overall summary of these factors. For the environmental aspect, only some critical elements were chosen here based on the real situation in Kenya.

Table 5.1 Main factors affect the quality of three satellite SM products

Comparison between active and passive SM products			
Category	**Factor**	**Effect on SM**	**Comparison between active and passive SM products**
Sensor	Observation wavelength	The penetration depth highly linked with wavelength. The shorter wavelength is more sensitive to vegetation, which produces a higher error when retrieving the SM	The wavelength used by passive is L-band while C-band for active. Therefore, SMAP and SMOS may have less effect by surface roughness than ASCAT
	Instrument	Directly affects the SM retrieval	Radiometer and SCATterometer are used for passive and active products
	Incident angle and azimuth angle	Affect the received signal strength, then impact the SM retrieval	Both brightness temperature and backscatter received from different land cover and surface roughness condition, having a close link with incidence angle.
Orbit	Passing time	The surface temperature and vegetation water content will change within one day, which affect the SM but was not fully considered into the retrieval model	If only considering the three satellites used in this study, 6:00 AM is passing time for passive products and 9:30 AM for active. The former one is more suitable for SM retrieval (Se et al.,2012)
Environmental	Vegetation cover	Reduce the signal from the soil while increase emission by itself, which cause more uncertainty during SM retrieving process	Vegetation cover has a significant effect on both active and passive products. The active sensor maybe more sensitive to vegetation because of the lower penetration capacity by C-band wavelength

LST	LST directly affect the SM retrieval	LST mainly influences the surface emissivity that impacts on the observed brightness temperature and used to derive the surface state flag (SSF) for ASCAT (active) product
RFI	Abnormal increase of brightness temperature by RFI, resulting in the SM value decrease	Only affect the passive products because passive products are based on direct emissions from the surface
Topography	Affect the signal strength of both backscatter and brightness temperature, and causing the heterogeneous SM within pixel size	Complex topography produces a geometric error for both active and passive products

Comparison of three satellites			
Products	**Main algorithm**	**Advantage**	**Disadvantage**
SMAP	Single channel algorithm (current baseline)	Compared with other algorithms (DCA and LPRM), the SCA has the best performance (Miernecki et al., 2014)	Need to calibrate the relationship between optical depth and vegetation index (Miernecki et al., 2014)
SMOS	L-MEB model, Iterative approach	Depending on the multi-angle system and iterative approach, the best fit for multiple parameters can be found instead of only SM.	The high-resolution auxiliary map will cause the heterogeneity inside the pixel, which influence the SM retrieval process; time-consuming because of each view angle need to be applied by the antenna patterns (Fernandez-Moran et al., 2017)
ASCAT	Change detection method	Moving time window calculation method improved the stability of the SM result	The porosity data needed to transfer SMI to volumetric SM. There is no accurate porosity map in the global range, which cause the error (Brocca et al., 2011)

5.1.2. Auxiliary data comparison

To retrieve the SM, a set of ancillary data are needed for each product. These data can be separated into two groups, static and dynamic data. Static data does not change over time e.g. DEM, permanent open water fraction, permanent masks (land/water/urban/forest/mountain) and soil properties. Dynamic data need an update from seasonally to daily, such as soil temperature, precipitation, land cover, vegetation parameters and surface roughness. All these data with different resolutions are pre-mapped to the same resolution of each satellite before using, and the table below shows a comparison of ancillary data used in three different satellites.

Table 5.2 Auxiliary data used for SMAP, SMOS and ASCAT

Parameters	SMAP	SMOS	ASCAT
Static auxiliary data			
Open water fraction	MODIS44W 250m	ECOCLIMAP	GLWD (2004) and GSHHS data
Urban/rural mask	Global Rural-Urban Mapping Project (GRUMP) dataset	-	-
DEM	GMTED-2010	GETASSE30 DEM (SRTM30 DEM, ACE DEM, and Mean Sea Surface (MSS) data composite)	GTOPO30

Soil texture	FAO (Food & Agriculture Organization), HWSD (Harmonized World Soil Database), STATSGO (State Soil Geographic— US), NSDC (National Soil Database Canada), and ASRIS (Australian Soil Resources Information System) soil databases.	FAO	FAO, HWSD
Permanent ice	MODIS IGBP	ECOCLIMAP	ERA40 data
Max annual LAI	-	ECOCLIMAP	-
Porosity	-	-	HWSD
Dynamic auxiliary data			
Land cover	MODIS IGPB	ECOCLIMAP, IGBP, ESL	-
Surface roughness	Land cover lookup table	Land cover lookup table	Land cover lookup table
Precipitation	ECMWF	ECMWF	ECMWF
Vegetation parameters	Land cover lookup table	ECMWF	Land cover lookup table
Crop type	Combination of USDA cropland data layer, AAFC-Canada, ECOCLIMAP-Europe, FAO	-	-
Soil temperature	GSFC GMAO	ECMWF	ERA-interim
Surface air temperature	GSFC GMAO	ECMWF	ECMWF
Vegetation water content	MODIS NDVI	ECMWF	-
Frozen land surface fraction	-	-	ECMWF ERA-40
Snow	IMS-NOAA	ECMWF	SSM/I
LAI	-	MODIS	-
RFI	-	SMOS L2	-
Sea ice cover	-	ECMWF	-

5.1.3. The relationship between auxiliary data and retrieved SM for three satellites

5.1.3.1. Spatial distribution of main auxiliary data and SM

a. Soil texture

The same soil texture map was used as static auxiliary data for three satellites. The soil map is from the Food and Agriculture Organization of the United Nations (FAO) website, which contains 26 different kinds of world classes of soil type. There are five classes within the study area. East part of the study area is cambisols (blue and red part). The middle part is vertisols soil type which is very common in Kenya, consists of expansive clay minerals. The green area is lithosols soil type, it is a kind of shallow soils generally due to the steep slope, also can be confirmed from the slope map. The other two small areas are ferrasols (white area) and nitosols (duck blue area) respectively, both these two types of soil occur in tropical areas with lush vegetation.

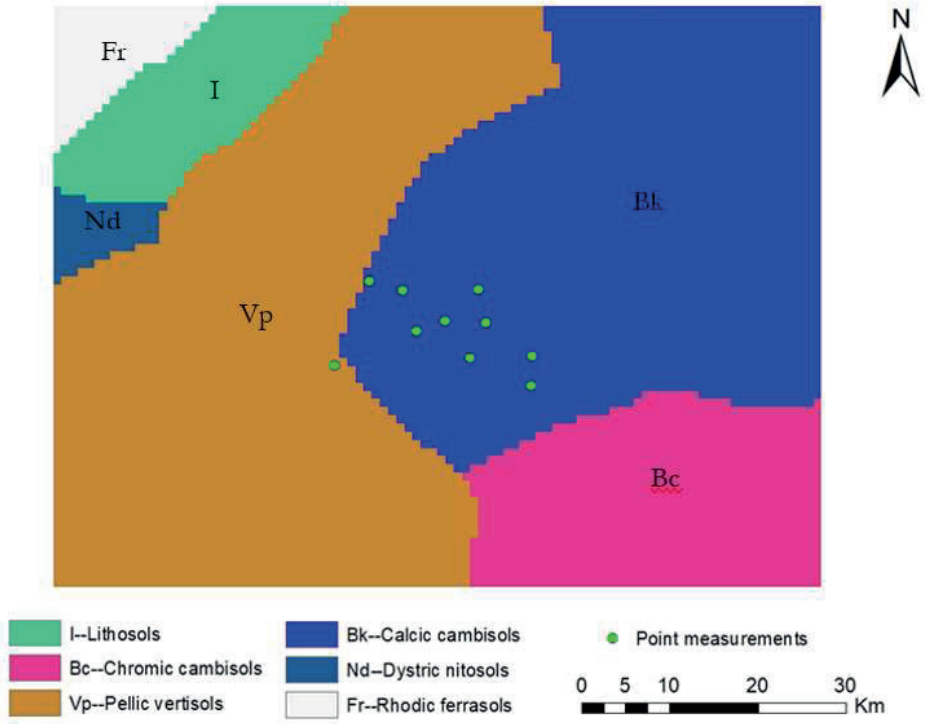

Figure 5.1 Soil texture auxiliary map from FAO within the study area

b. DEM

SMAP uses GMTED2010 dataset with three different spatial resolution of 30, 15 and 7.5 arc-seconds. The Global Earth Topography and Sea Surface Elevation at 30 arc-second resolution (GETASSE30 DEM) dataset is used as SMOS auxiliary elevation data, and it is a composite dataset from SRTM30 dataset, ACE dataset, Mean Sea Surface (MSS) data and EGM96 ellipsoid. For ASCAT, the 30-arc resolution (around 1km) GTOPO30 dataset is adopted. The comparison of three DEM maps show as below. All three DEM maps have a similar trend, with a lower value in the center of the study area and relatively high value in the east part and north-west area. However, compare with the ASCAT DEM map, SMAP and SMOS have almost the same spatial distribution. The elevation change within the study area is around 1000 meters, but mainly concentrate in the east part. All the points are in the lower ground, so the elevation difference among these sites is not significant.

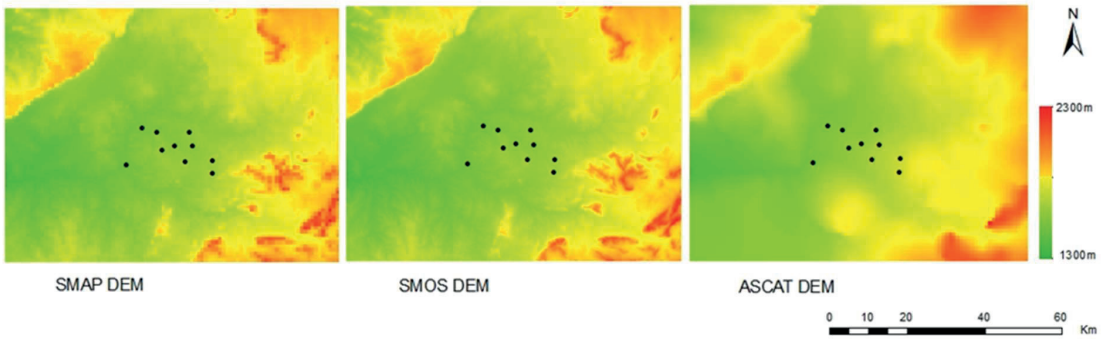

Figure 5.2 DEM auxiliary map comparison among three satellites within the study area

After converting the DEM to slope in ArcGIS, the more dynamic change can be seen from SMOS and SMAP compared with ASCAT within the whole study area. However, almost the same slope (around zero) appears in the centre area base on Figure 5.3.

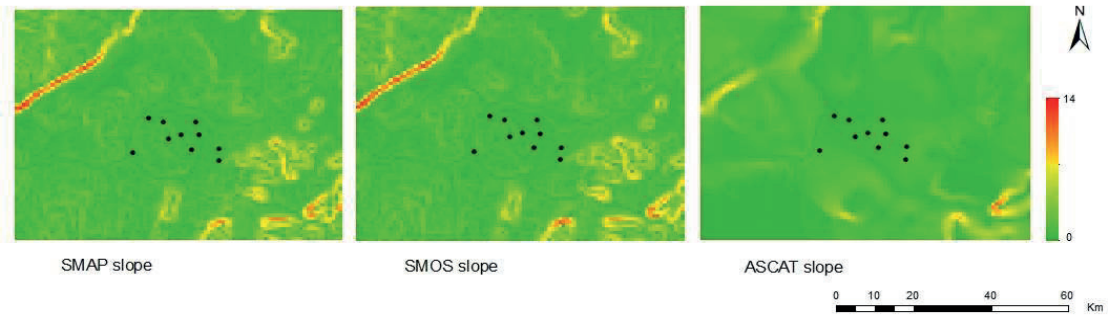

Figure 5.3 Slope auxiliary map comparison among three satellites within the study area

c. Land cover

For SMAP and SMOS, the land cover map is not static auxiliary data, it changes each year. However, within this research period of one and a half years, it was considered to be static. There are two global land cover-map with fine resolution. One is the International Geosphere-Biosphere Programme (IGBP) defined surface classifications and the other one is the University of Maryland (UMD) global land cover. The land cover map used by SMAP is MODIS IGBP with 17 classes and 500m resolution. SMOS uses ECOCLIMAP map which has 1km resolution. The ECOCLIMAP mainly used the UMD global land cover map except for permanent ice and open water area, which keep the same with IGBP (Champeaux et al., 2005). For both SMAP and SMOS, the land cover map was resampled to the same as the footprint of satellites before using as the input auxiliary data.

The MODIS IGBP map from Figure 5.4 shows that around 90 percent of the study area covered by grassland. According to the information collected by Donald T. Rwasoka, almost all the point measurement stations covered by grassland, which matches the IGBP map. Moreover, the SMOS auxiliary land cover map is more complex. It contains eight different kinds of land cover type. There are three main types (grassland, savanna and grass with sparse shrubs), although these three land cover types have similar properties, the denser vegetation can be seen from ECOCLIMAP compared with IGBP.

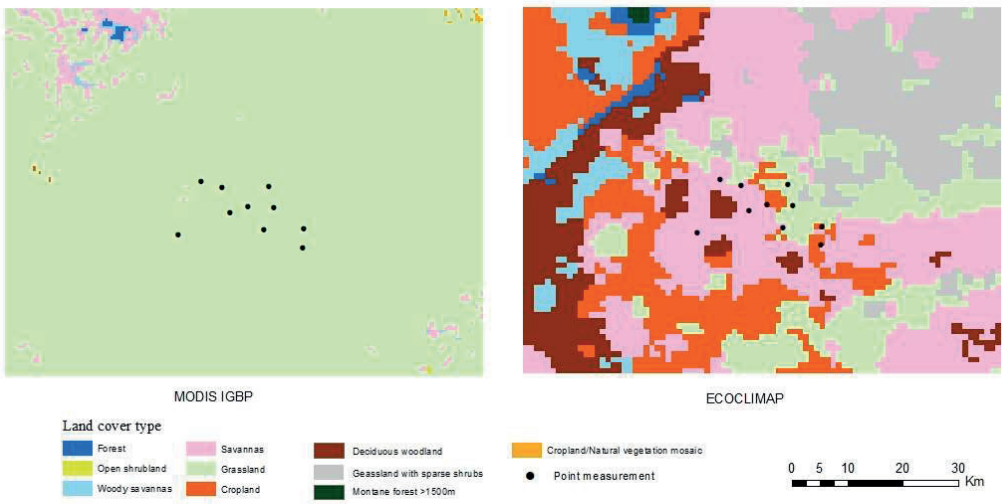

Figure 5.4 Land cover map comparison, left is MODIS IGBP map and right is ECOCLIMAP land cover map

For ASCAT, the land cover map is obtained from the Harmonized World Soil Database (HWSD). It completes and updates the FAO and International Institute for Applied Systems Analysis (IIASA) soil map by combing existing regional and national soil information. Then created seven land use land cover (LULC) results. Three LULC map (grass, forest and total cultivated map) were used in study area. This result agrees with SMAP land cover auxiliary map, most of the area covered by grassland, while in the south-west part shows a difference. In the ASCAT land cover map, the forest land cover can be seen in the left down corner.

Therefore, if only consider the land cover situation over ten in-situ measurement stations, SMAP and ASCAT auxiliary land cover maps provide a better result, which can match the real condition.

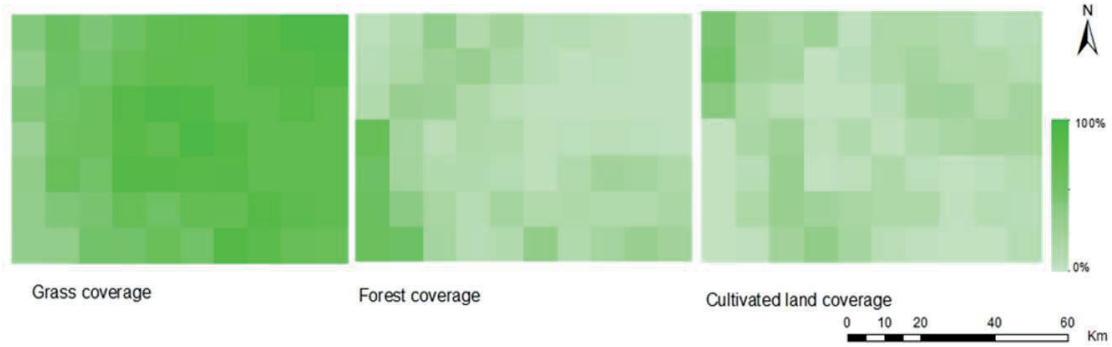

Figure 5.5 ASCAT auxiliary land cover maps from HWSD

d. Precipitation

ECMWF precipitation is used by the three satellites as the primary precipitation data, it shows a better performance after validation using in-situ data (Entekhabi et al., 2014). Monthly average maps are prepared to show the relationship between SM and precipitation within the study area. Dry, moderate and wet season were selected in this case, for September, January and April respectively. A clear difference can be seen from these three precipitation maps.

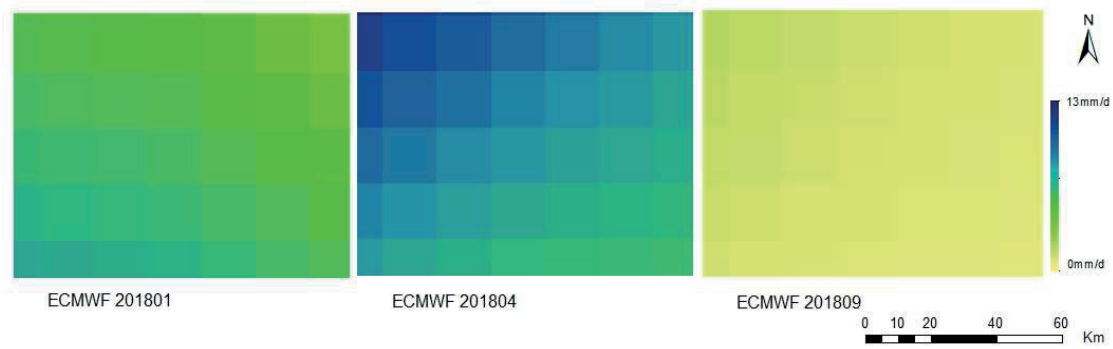

Figure 5.6 ECMWF monthly averaged precipitation map

e. Surface temperature

The surface temperature auxiliary data used for SMAP, SMOS and ASCAT is different. MERRA dataset with hourly temporal resolution is for SMAP. For SMOS and ASCAT, the same ECMWF reanalysis data is used (Entekhabi et al., 2014). The result shown that MERRA and ECMWF surface temperature during September have a similar spatial distribution, however, the MERRA dataset has a relatively higher dynamic change. During January and April, there are slight differences between these two datasets. While linking ECMWF surface temperature map with the precipitation map, we can see more precipitation cause lower

surface temperature. The range for the surface temperature change is quite small, only from 290k to 297k. Nevertheless, this only represents these three specific months, not for other time periods.

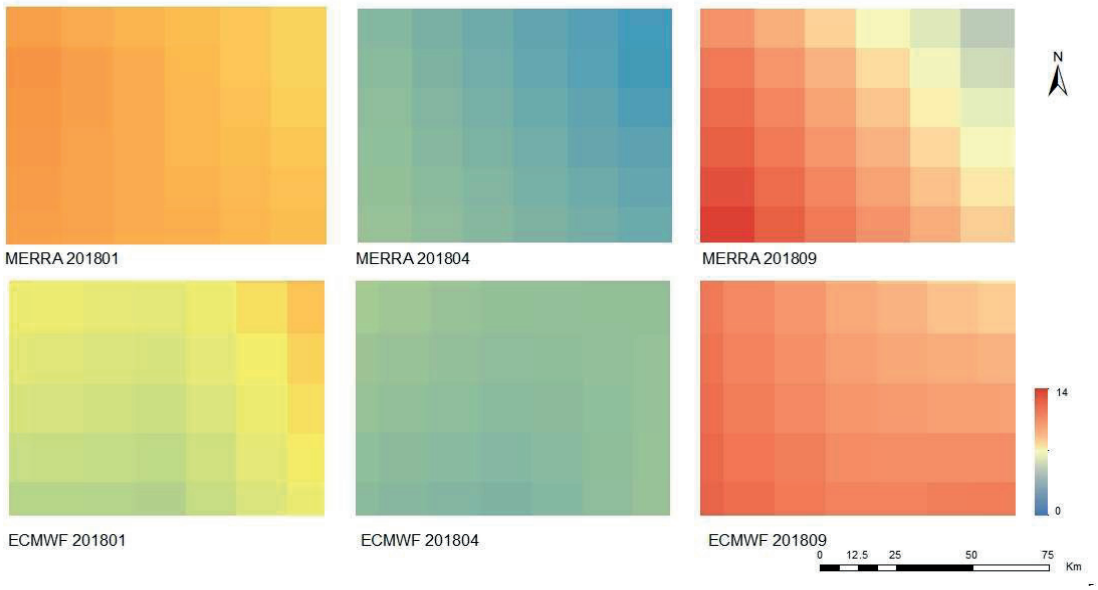

Figure 5.7 MERRA and ECMWF monthly average surface temperature map

f. Monthly SM patterns

The monthly averaged SM map is used here to compare the spatial SM distribution between the three satellites. In order to link with the dynamic auxiliary data, the same months were chosen here (January, April and September indicate the median, wet and dry month). In general, SMAP and SMOS show a similar spatial pattern, which has a strong link with precipitation map especially during wet and dry season. From April and September precipitation maps, more rainfall appeared in the north-west part of the study area, which can match the higher SM value occurs in the same region. However, the ASCAT has a different SM pattern; a higher SM value occurs in the south-east area. Compared with these three months, a similar distribution can be seen from the ASCAT SM map with relatively higher value occurs in the south-east part and lower SM appears in the west part. Considering the ASCAT used the same precipitation and temperature data as SMOS, this difference may be caused by the porosity data, which used to convert the SMI to SM by ASCAT.

Except for the dynamic auxiliary data influence, the similar spatial distribution between SMAP and SMOS is more linked with the algorithm used by passive products. This also linked with the precipitation map distribution. While it is difficult to identify the relationship from ASCAT. Moreover, these maps are based on the monthly averaged SM value, which cannot represent the specific daily change.

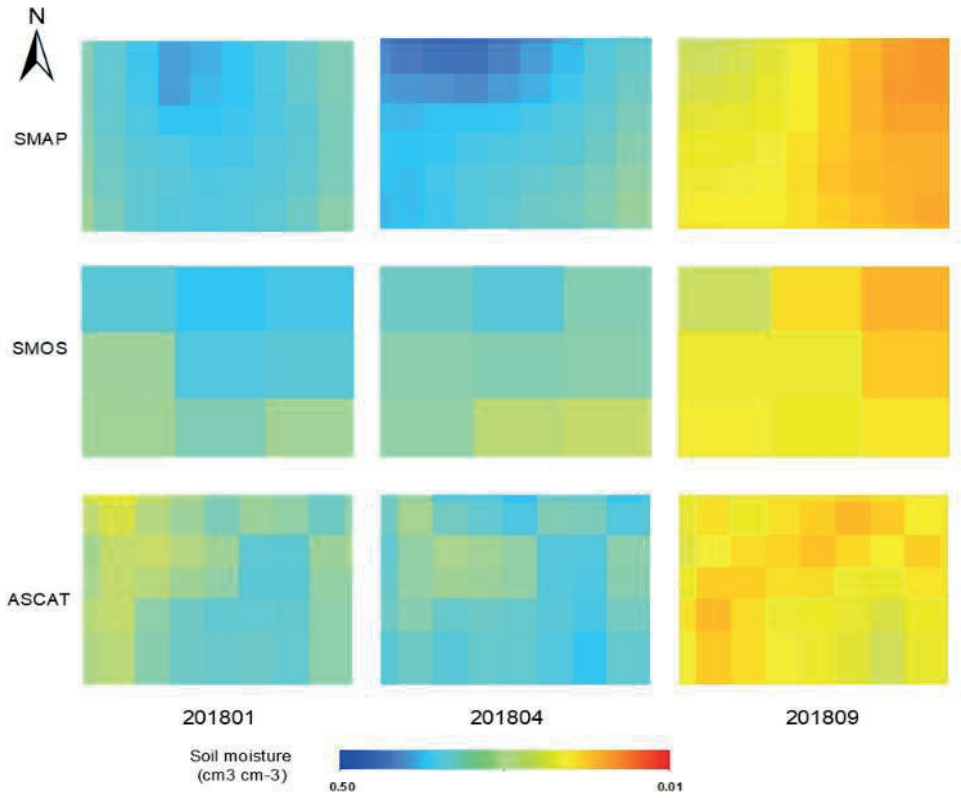

Figure 5.8 SM monthly average spatial distribution maps for three satellites

5.1.3.2. Temporal change between dynamic auxiliary data and SM

The monthly averaged dynamic map was used to compare the spatial pattern of SM distribution. To clearly show the relationship between SM and precipitation/temperature, the monthly means was calculated and inter-compared in this subsection.

Figure 5.9 indicated the precipitation change from June 2017 to December 2018 together with the SM change. All these three satellites have a good response to the rainfall event. The SMAP has a higher mean SM value especially during the rainy season from March to May. While ASCAT shows a relatively lower SM trend during the dry season. Besides, SMAP and SMOS SM change have almost the same trend within the whole year. However, the difference between these two satellites is bigger during the rainy season and smaller during the dry period. One reasonable explanation is that two passive products have different response to the rainfall event, and another reason is the effect of vegetation cover. During the wet season, dense vegetation occurs while causing uncertainty for the SM retrieval.

Different from the precipitation auxiliary data, the surface temperature data used by SMAP is different from SMOS and ASCAT. From Figure 5.10, a lower surface temperature trend can be seen from MERRA dataset (used by SMAP) compared with ECMWF (used by SMOS and ASCAT). This may be one of reasons causing SMAP being of higher SM than the other two satellites. Generally, the SM value and surface temperature have the opposite trend. However, this relationship did not exactly happen during each month. For example, in January, a relatively higher temperature and SM value occurs, which means the surface temperature may not be the dominant factor to control the SM change.

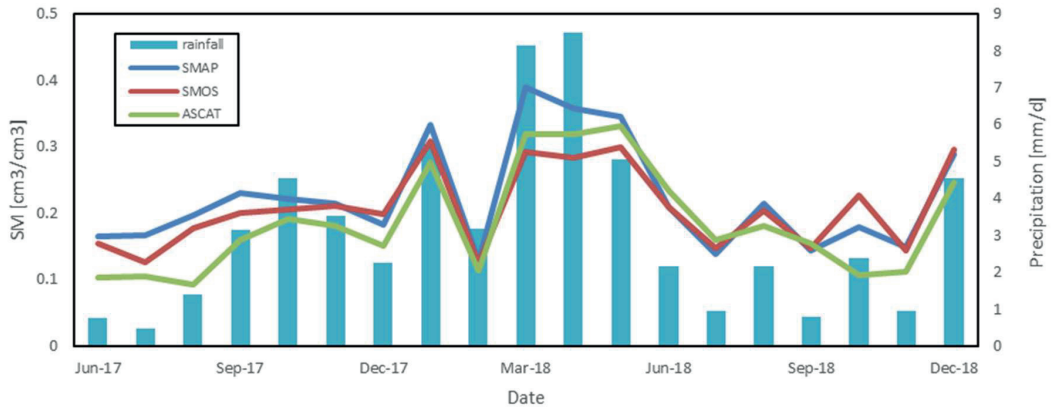

Figure 5.9 Monthly mean precipitation and SM for three satellites

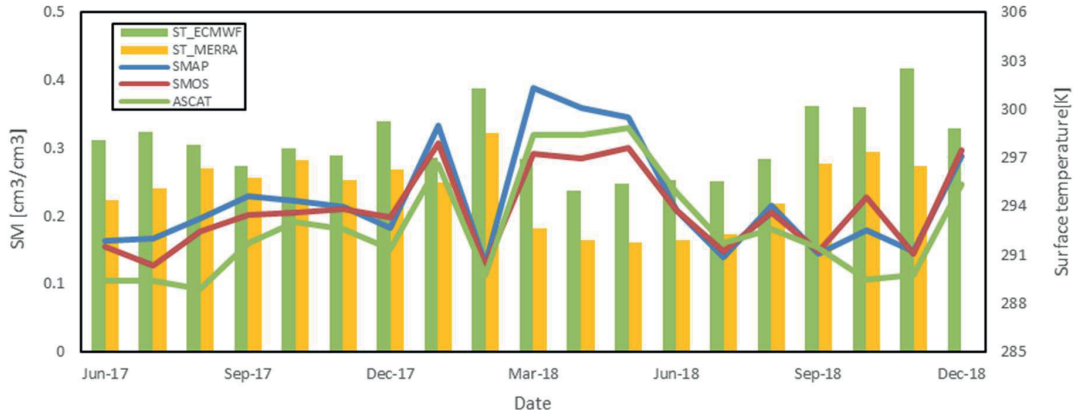

Figure 5.10 Monthly mean surface temperature and SM for three satellites

The microwave sensor was proved with higher penetration depth and it is more sensitive to the SM change (Lannoy et al., 2013; Miernecki et al., 2014). All these products are influenced by the vegetation and surface roughness. The inter-comparison mainly compared the algorithm and auxiliary data used for the three satellites. There are similarities between SMAP and SMOS. ASCAT used the C-band scatterometer to retrieve the SM. The change detection method can only get the SMI instead of SM value, which may induce extra uncertainties and errors. For the auxiliary data part, the big difference happened for the land cover map used by the three satellites. As mentioned before, vegetation has a strong effect on the retrieved SM. Therefore, the accuracy of the land cover map is significantly important for getting SM estimates correct.

5.2. SM variability result

5.2.1. The relationship between SM variability and soil texture

The hydraulic parameters are obtained from PTF based on soil grids map. Then Levenberg-Marquardt (LM) algorithm was applied to calculate the best fit of these parameters within each coarse pixel for different satellite products. The standard deviation of these parameters also calculated. Because of the homogeneity of the study area, the soil information dynamic change like clay, silt and sand content is not significant. After calculating the upscaled coarse pixel soil information, there are two main types within the study area: clay loam (CL) and sandy clay loam (SCL). Soil texture result can be seen in Figure 5.11.

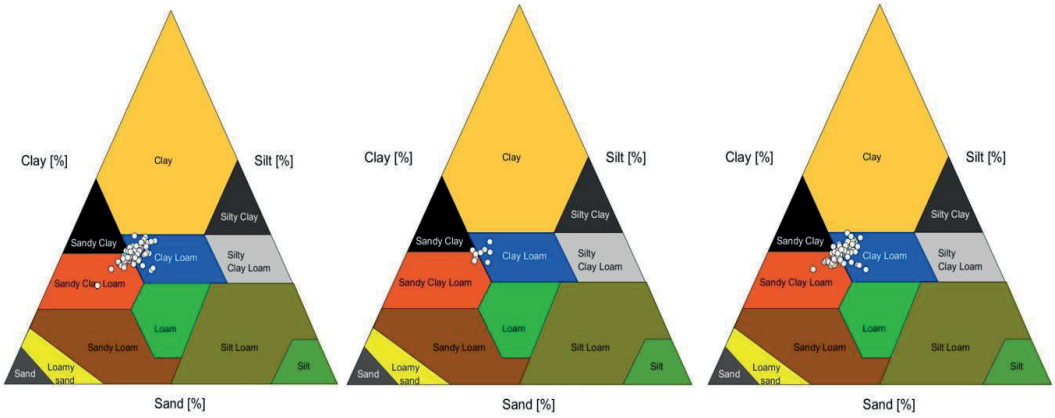

Figure 5.11 Soil type within coarse resolution satellite products. From left to right are SMAP, SMOS and ASCAT respectively.

The PTF result for different satellites can be separated into two parts, CL and SCL. Table 5.3 indicates that the hydraulic parameters have similar result for each soil type.

Table 5.3 Mean and standard deviation of VGM parameters obtained by Wösten et al. (1999) PTF method

Soil texture	Hydraulic parameters							
	α (cm-1)	n (-)	f (cm d-1)	θ_s (cm3 cm-3)	σ_α (-)	σ_n (-)	σ_f (-)	σ_{θ_s} (-)
CL_SMAP	0.050	1.108	3.607	0.442	0.004	0.008	0.210	0.008
CL_SMOS	0.050	1.110	3.626	0.442	0.005	0.009	0.264	0.010
CL_ASCAT	0.049	1.108	3.576	0.442	0.004	0.008	0.216	0.008
CL_average	**0.050**	**1.109**	**3.603**	**0.442**	**0.004**	**0.008**	**0.230**	**0.009**
SCL_SMAP	0.057	1.122	3.895	0.434	0.003	0.009	0.180	0.010
SCL_SMOS	0.004	1.114	3.700	0.432	0.004	0.010	0.268	0.015
SCL_ASCAT	0.057	1.121	3.850	0.432	0.004	0.009	0.194	0.010
SCL_average	**0.039**	**1.119**	**3.815**	**0.433**	**0.004**	**0.009**	**0.214**	**0.012**

To analyze the relationship between soil type and SM variability, the average SM variability was calculated for two main soil types based on the same mean SM condition. Eight mean SM values from 0.05 to 0.4 (0.05, 0.1, 0.15, 0.2, 0.25, 0.3, 0.35, 0.4) was used to evaluate the SM variability for CL and SCL of different products. It is worth noting that this result cannot represent the true variability for these two different soil types, since the soil type may change after counting the mean value. But, it can give some sense of how the SM variability change under different conditions. Figure 5.12 illustrates the SM variability under different mean SM condition for three products.

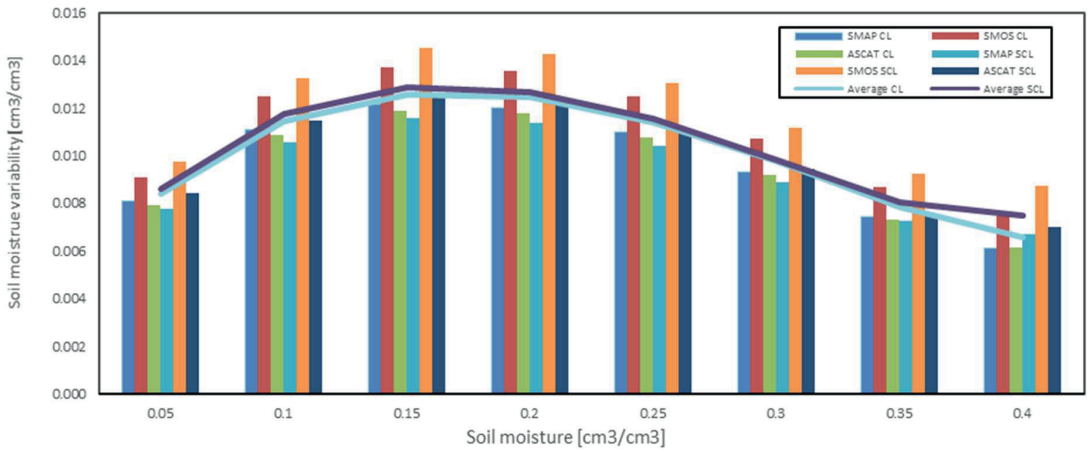

Figure 5.12 Diagram of SM variability change under CL and SCL soil type

The result shows that the SM variability has the same convex trend for these two soil types, which calculated based on coarse pixel of each satellite. The biggest SM variability occurs under 0.15 to 0.2 (cm3 cm-3) mean SM condition. The average result for CL and SCL indicated that the similar SM variability happened within the whole study area. Compared with three satellite products, SMOS has the biggest SM variability. According to Qu et al. (2015) research, the SM variability is mostly linked with the standard deviation of parameter n, here, a slightly bigger result of this value also occurs for SMOS which is consistent with previous research.

5.2.2. SM variability based on selected grids point

As reported in the previous part, the SM variability has the relationship with mean SM. For different satellite products with different spatial resolutions, the SM variability within each coarse pixel has been calculated. Because the soil texture within the study area is quite similar, only one specific pixel that contains the CRNP site is used to compare the SM variability change for the three products. The result was shown in Figure 5.13.

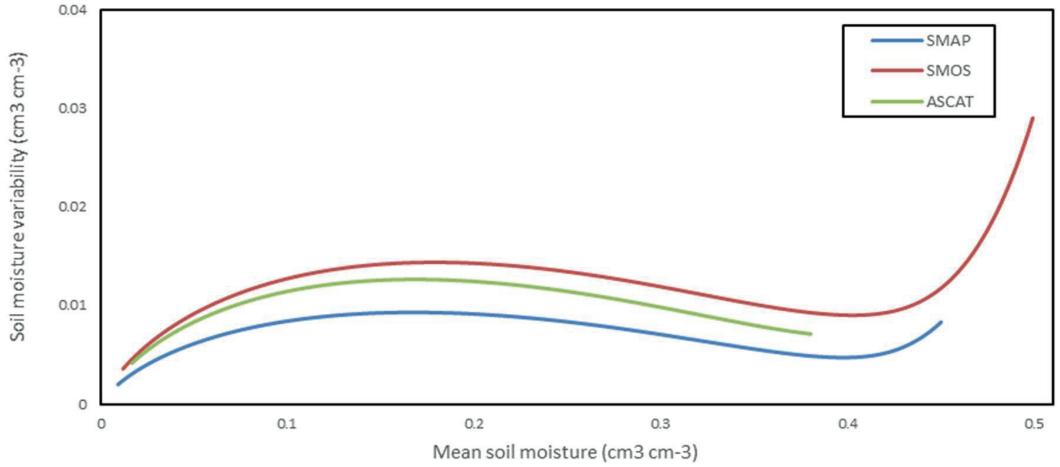

Figure 5.13 Relationship between SM variability and mean SM for SMAP, SMOS and ASCAT within a coarse pixel.

When the mean SM is smaller than 0.4 cm3 cm-3, all these curves showed a similar convex trend. So, low SM variability appears under dry condition; then it increases with the mean SM peaked in 0.17cm3 cm-3

followed by the decrease. Although three SM products share a similar trend, the SMOS has the most significant variability under the same situation whereas SMAP has the smallest change. Considering the same soil texture for these three satellite pixels. A possible explanation for this result may be the spatial resolution difference among three satellites, where SMOS has the largest resolution and SMAP is the smallest one. The peak of SM variability for SMOS is around 0.15, for SMAP and ASCAT are 0.1 and 0.13 respectively. Compared with the research by Montzka (2018), who analyzed the SM variability over the global range, the result is quite similar in this area. When the mean SM is bigger than 0.4 cm3 cm-3, the soil water content is almost reaching the saturated value and a sharp rise in the variability can be seen for SMOS and SMAP.

5.2.3. Sensitivity analysis of hydraulic parameters

The VGM hydraulic parameters were calculated based on the PTF provided by Wösten et al. (1999). There are four parameters in the VGM model used to obtain the SM variability: α, n, θ_s and $f(\ln k_s)$. θ_s is saturated water content (cm3 cm-3); k_s stands for saturated hydraulic conductivity (cm d-1); α and n are air entry parameter and pore size distribution parameters respectively. The mean VGM parameters were calculated for each satellite product at their original spatial resolutions.

Since all three SM products has almost the same trend, only SMOS was used to do the sensitivity analysis in this research. The sensitivity analysis was based on the original dataset. Then change one parameter and keep others the same to evaluate different performances of these parameters. The original dataset shows as below:

Table 5.4 SMOS specific pixel hydraulic parameters

Soil texture			**PTF result**			
Clay (%)	Silt (%)	Sand (%)	α(-)	n(-)	f(cm d-1)	θ_s(cm3 cm-3)
33.5	21.0	45.5	0.054	1.114	3.738	0.439

Figure 5.14 indicates that parameter n is most sensitive to the SM variability change followed by θ_s, then α and the last one is f. This result agrees with Vereecken et al. (2007) on the analysis of Brooks-Corey model, where λ was found the most sensitive parameter. Both n and λ control pore size distribution that is directly influencing the shape of WRC. The relationship between mean SM and SM variability changes mainly because of the n value. Under the lower n value condition, there tend to have a negative relationship between mean SM and SM variability, while it changes to positive under higher n value and the convex relationship can be seen in the medium condition. These results reflect those of Wang et al. (2015), who also found that the SM variability has positive link with mean SM under coarse soil texture. The SM variability has a similar trend with the changing θ_s value. For the rest two parameters, almost no change can be detected with different mean SM conditions, especially for f. The SM variability has a second increase after mean SM value of 0.4 cm3 cm-3. However, this result is questionable as the SM content at this area seldom reached the saturation.

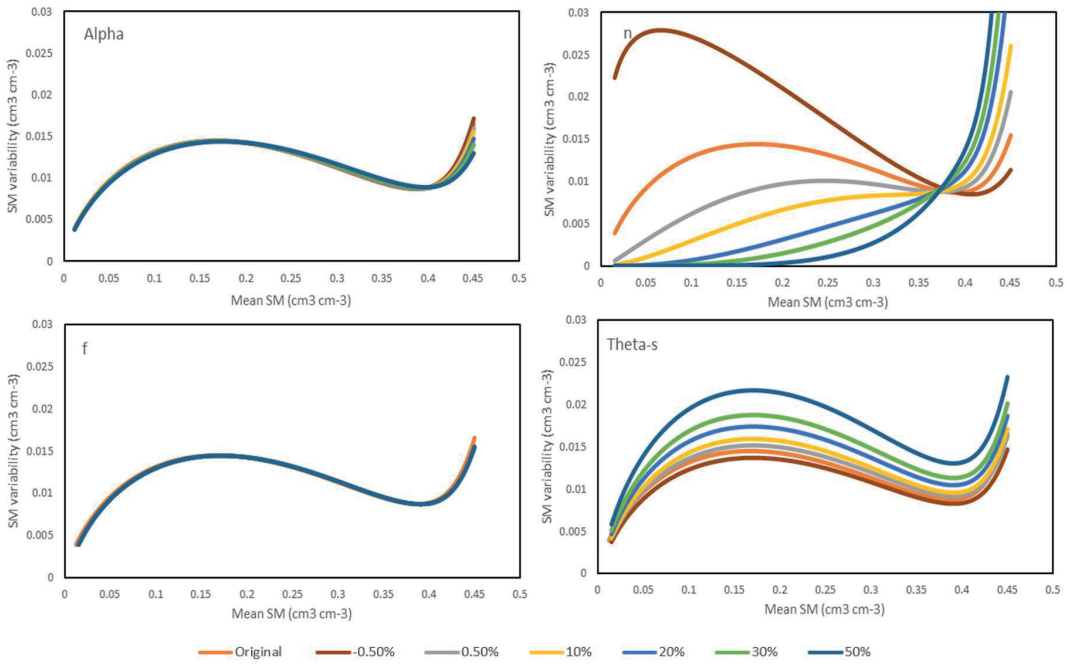

Figure 5.14 Sensitivity analysis result for hydraulic parameters

In this study, the accuracy of the soil map and PTF is crucial as the hydraulic parameters have a strong link with the SM variability especially for n value. A convex relationship obtained between mean SM and SM variability for CL and SCL, this finding was also reported by Qu et al (2015). However, as the study area is relatively homogeneity, the convex relationship as derived here may not represent the conditions with other soil types. The SM variability under different soil types has distinct performances according to Wang et al. (2015), which mainly depends on the soil water holding capacity. Besides, the environmental condition also plays an essential role in the SM variability change, which was not fully considered in this method.

5.3. Downscaling and comparison result

5.3.1. SM downscaling result

Field capacity (FC) was used as the proxy data to downscale different satellite products to 1km resolution. FC refers to the amount of water remaining in the soil after the excess water drained away and the downward rate of water has decreased. This state usually occurs 2 to 3 days after precipitation or irrigation in homogeneous soil. FC may be affected by soil texture, soil structure, organic matter content in the soil, land cover and so on. Even within the same type of soil, the FC may be different because of the distinct climate or land use. Figure 5.15 shows the FC spatial distribution within the study area. The range of value is from 0.25 to 0.40 (m3/m3), and the upper region shows a higher value compared with the lower part area.

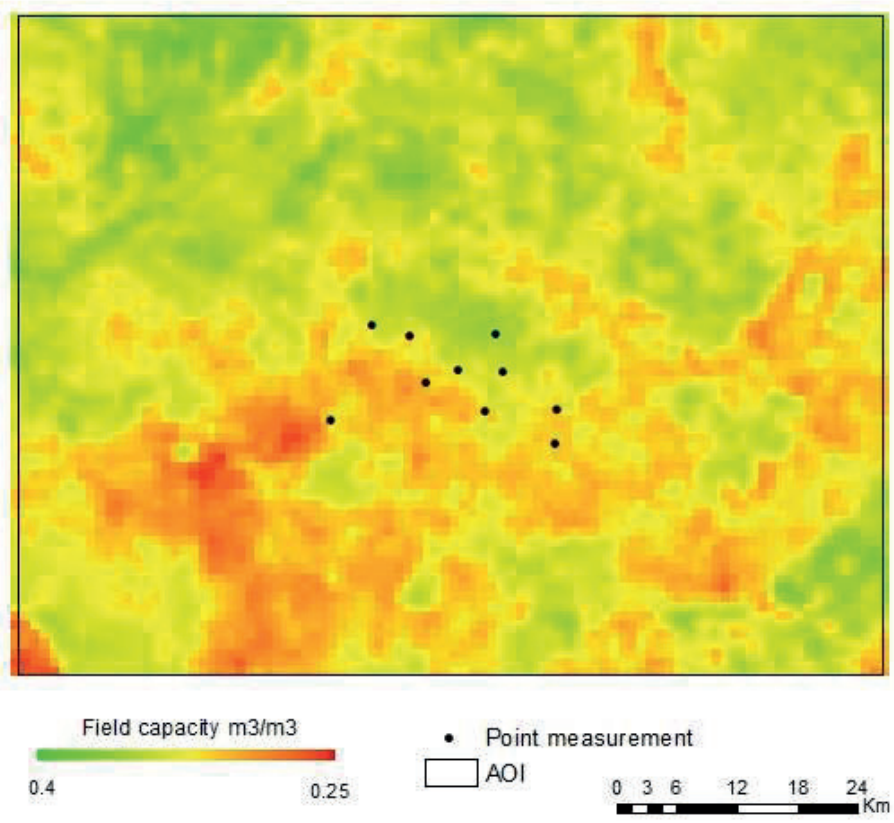

Figure 5.15 Field capacity map calculated from Soil Grids using PTF within study area

Figure 5.16 illustrates the mean SM of original, downscaled and downscaled-interpolated result. In this figure, the first column is the original map, the second column is the downscaled result and the last one is the interpolated map. The SM pattern is difficult to identify on the coarse resolution SM map. Especially for SMOS with large spatial resolution. While the downscaled result shows detailed sub-grids SM pattern within the coarse pixels. However, because of the SM difference between neighbor pixels are very significant for the coarse resolution SM map. The apparent gap still can be seen from the high-resolution map after downscaling. Because of the average SM value was calculated within the whole period, this difference is not outstanding. If we check the Appendix A for daily SM map, the sharp difference between different pixels is much more significant, especially for SMOS. Therefore, the further method needs to be

used to smooth the sharp edges at the coarse pixel border. A simple interpolation method applied here based on the SM variability change between the grid center.

$$\widetilde{\theta_{I,(i,j)}} = \overline{\theta_I} + \sigma_{I,\theta}(\overline{\theta}) \frac{P_{i,j} - \overline{P}}{\sigma_p} \quad 5\text{-}1$$

Where $\overline{\theta_I}$ and $\sigma_{I,\theta}(\overline{\theta})$stand for the mean SM and SM variability between grid centers respectively.

Compared with these three different mean SM maps, SMAP shows higher value compared with others. The SM had a gradually change from north-west to the south-east, from wet SM pattern to the relatively dry pattern. SMOS presents a similar SM spatial distribution as SMAP. However, a totally different spatial distribution and a drier trend can be found in the ASCAT SM map. When linked with the porosity map, the area with higher porosity gives a relatively higher SM value in this mean SM map. This means the porosity data plays a crucial role during the SM retrieval of ASCAT (also see SM maps for different month in Appendix A). In general, all these three satellite products can capture the seasonal change of SM in Kenya. The wet season appears around March and April, with the relatively high value of SM in April. And. During August and October, the SM value is much lower.

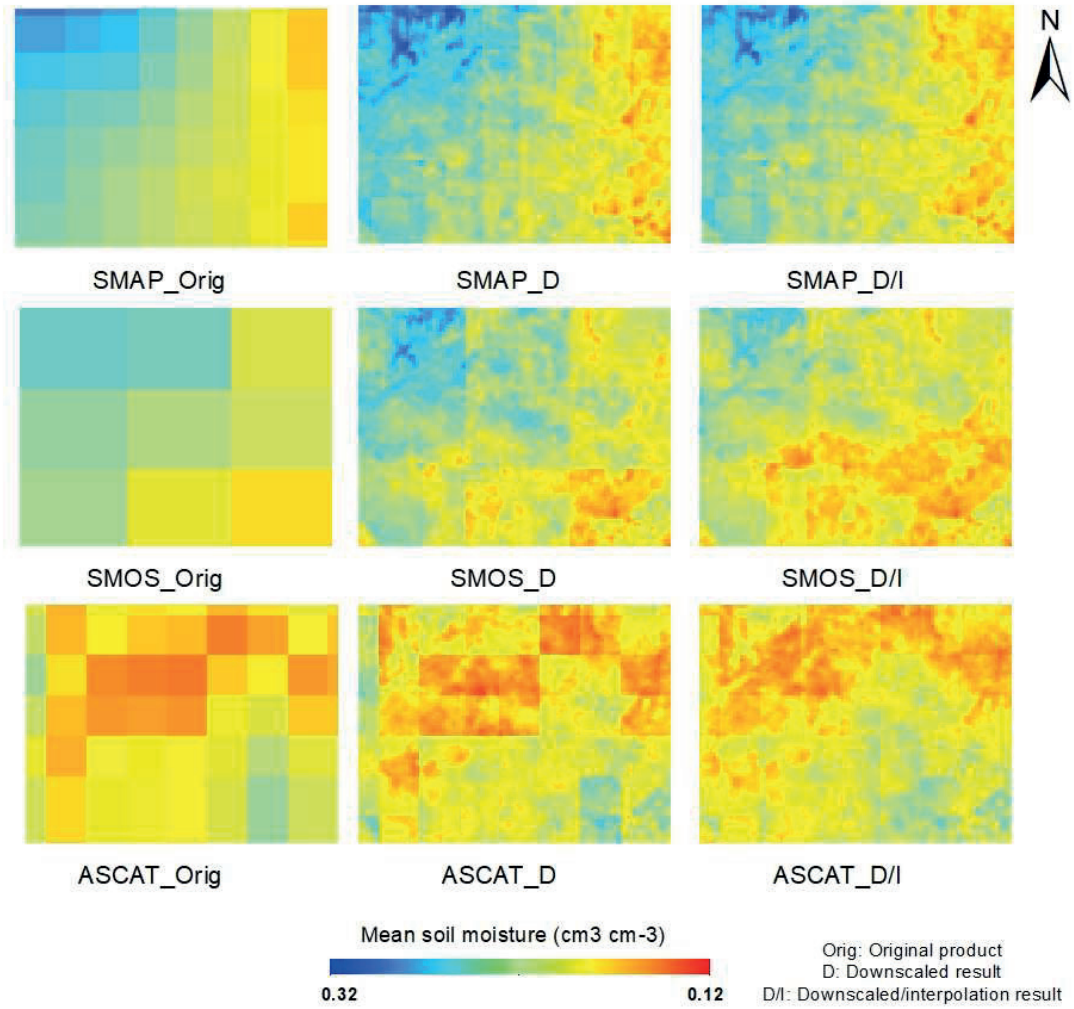

Figure 5.16 Mean SM spatial distribution for original, downscaled and D/I result

5.3.2. Correlation coefficient between satellite products

The Pearson correlation coefficient (R) was calculated for both original and downscaled result between two satellites. In Figure 5.17, the top three images are for original products while others are downscaled correlation result.

Considering the R between original products, SMAP and ASCAT have the strongest link with each other. The R value between them is more than 0.65 within the whole study area. SMAP and SMOS also show good relationship, especially for the eastern part. When linked with the land cover map (Figure 5.4), more different land cover types appear in the west part of the SMOS. This situation cannot match with SMAP land cover map, maybe a reason causing the low correlation between SMAP and SMOS in the west part of the study area. ASCAT and SMOS are not correlated at all. Since the ASCAT SM has a tight link with porosity data, the relatively low relationship may be caused by inaccurate porosity data.

For the relationship between the downscaled products, the correlation has the similar spatial pattern compared with original products. The value increased within the whole study area. For example, SMAP and SMOS are poorly correlated in the south-west part, but it becomes better after downscaling (the R improves from 0.2 to 0.4). This is also true for the ASCAT vs SMOS map. The same FC map used as the downscaling data may cause the similar SM changing trend for the sub-grid soil of three satellite products, causing higher R values among the three downscaled SM products.

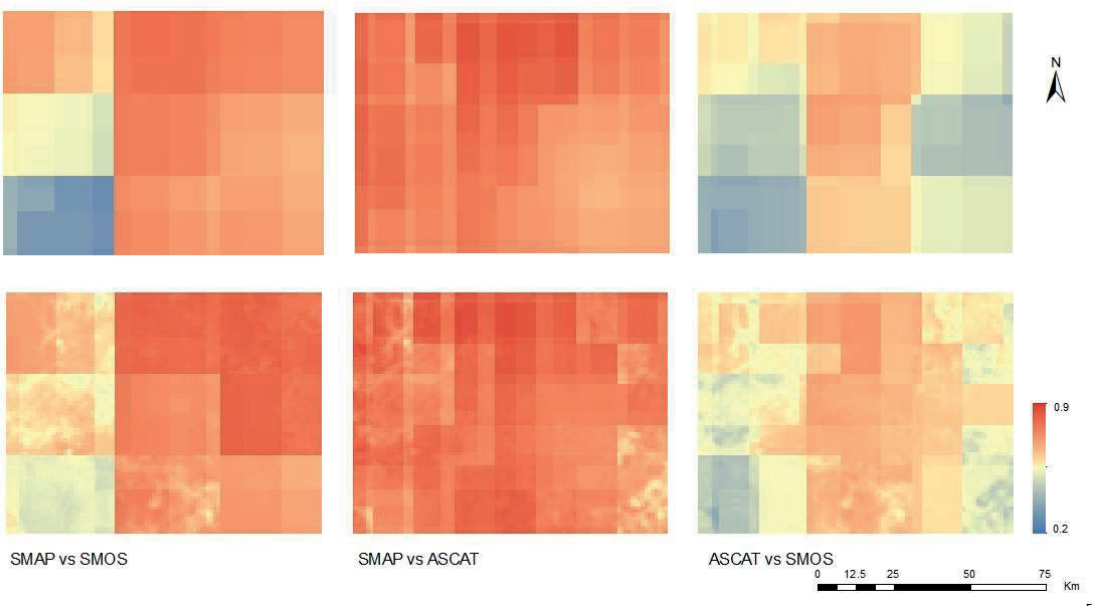

Figure 5.17 Correlation of coefficient map between two original and downscaled satellites

5.3.3. Triple collocation analysis among three satellites

Figure 5.18 shows the TC result for SMAP, SMOS and ASCAT. The upper images are error variance results for three satellite products and below are SNR result. Normally, TC method is used among satellite, modeling and in-situ measurement data. But here, considering three satellites used the different algorithms and input data, the TC analysis is also possible to be applied. TC result indicates that SMAP has the lowest error variance pattern among the three products with an average value around 0.03 (cm3 cm-3). ASCAT shows poorer result than SMAP with the average error variance of 0.06 (cm3 cm-3). The error variance for both SMAP and ASCAT are better than SMOS within the whole study area.

For the SNR map, the value of zero means signal variance is equal to the noise variance. Each ±3 dB gives the twice or half ratio between signal variance and noise variance. As shown in the output map, all these three satellites tend to have a negative value of the SNR, it means the noise outweighs the signal. SMAP has a higher SNR value compared with SMOS and ASCAT. And, it is pretty much coinciding with its error variance map.

The SNR map for SMOS has a relatively good performance in the east part of the study area and a significant low performance in the south-west corner. This phenomenon also appears in the R map. A very poor correlation finds in the same area with SMOS to the other two products. The specific reason for this result may be attributed to the land cover map used in SMOS. It is interesting to note that the SNR pattern of SMOS cannot match its error covariance map, especially in the northern part. Based on Gruber et al. (2016) research, the SNR may also be dominated by the sensitivity pattern. The higher sensitivity value indicates a stronger response to the SM change. In this case, probably SMOS is not sensitive to catch the SM dynamic, also more abnormal values cause the higher error variance in SMOS.

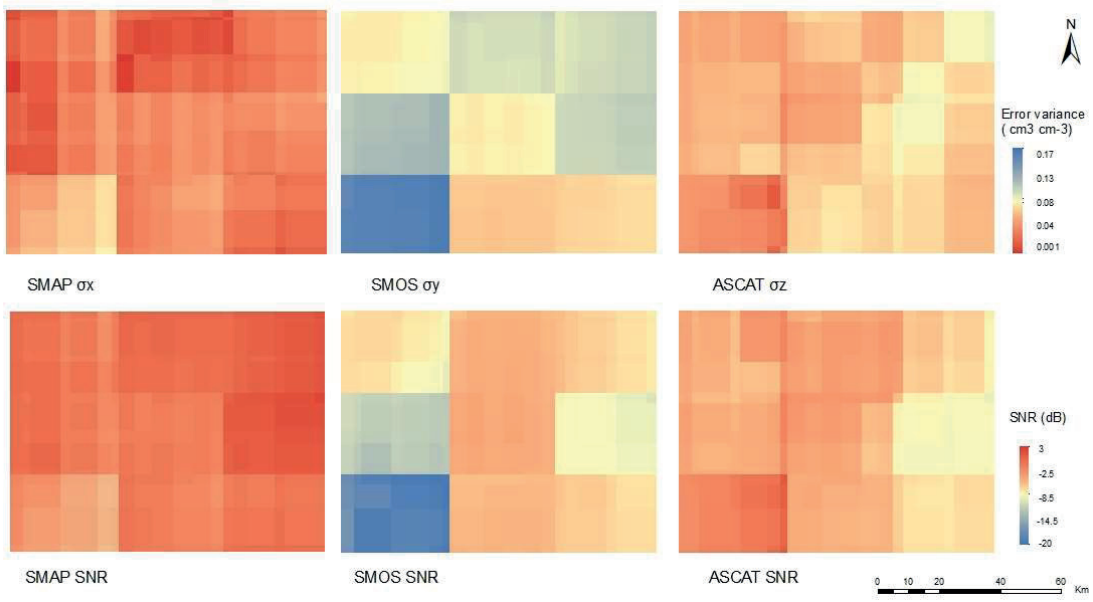

Figure 5.18 TC result for original products

To clarify the SM change for the downscaled SM, TC was also applied to the downscaled result. Compared with original products, the error variance for three products become smaller within the whole study area. SNR value also has slightly increased. Especially for the SMOS, some extremely worse values were reduced. Considering the spatial pattern between the error variance and SNR. Almost all downscaled products keep the same in both maps. It implicated that the downscaling leads a consistent spatial pattern of SM distribution for three products.

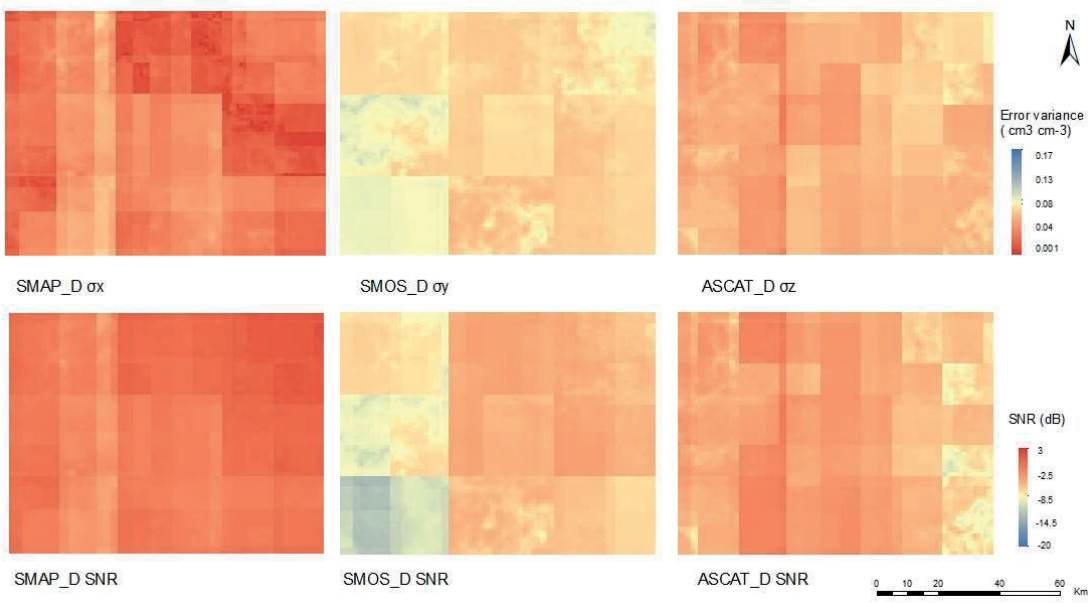

Figure 5.19 TC result for downscaled results

The downscaled result indicates that sub-grid variability and FC porosity data can be used to disaggregate the SM products. From a coarse resolution to 1km resolution. For SMAP and SMOS, the similar SM spatial distribution happened in most cases. While ASCAT SM spatial distribution is more dependent on the porosity data. The correlation coefficient between different products become better after downscaling. Because the satellite products have a similar changing trend of the SM by using the FC proxy data. However, the SM retrieved value by SMOS on the bottom left corner may contain more abnormal values. Based on the TC analysis, downscaled result reduced the noise power. Because the VGM model used in this method has a relatively reasonable saturated SM. This concept helps to ignore some extremely high SM value when downscaling, causing the increase of SNR result, which is obvious for SMOS.

5.4. Validation result

5.4.1. Validation against point measurement data

The original products and downscaled result for three satellites were validated against point measurement. This used to analyze the performance of each satellite within the period from June 2017 to December 2018. Table 5.5 shows the validation metrics of R, bias, RMSE and ubRMSE for three products against the in-situ measurements of ten stations.

Table 5.5 Validation metrics of SMAP, SMOS and ASCAT products in ten stations. Orig is the original coarse products, D is the downscaled result, and D/I is the interpolated result.

Product	Station	R			Bias			RMSE			ubRMSE		
		Orig	D	D/I	Orig	D	D/I	Orig	D	D/I	Orig	D	D/I
SMAP	Mara-main	0.807	0.805	0.798	-0.056	-0.062	-0.051	0.092	0.095	0.090	0.073	0.073	0.074
	Mara-bridge	0.860	0.859	0.866	-0.037	-0.041	-0.027	0.077	0.079	0.074	0.068	0.068	0.069
	Ashnil	0.762	0.765	0.764	-0.108	-0.097	-0.090	0.134	0.124	0.117	0.078	0.077	0.075
	Kissinger	0.735	0.735	0.734	-0.014	0.000	0.010	0.075	0.073	0.070	0.074	0.073	0.070
	Upstream	0.729	0.726	0.709	-0.041	-0.026	-0.017	0.065	0.057	0.049	0.050	0.050	0.046
	Olimisigol	0.691	0.690	0.690	0.014	0.023	0.033	0.056	0.059	0.062	0.054	0.055	0.052
	Nice-bridge	0.467	0.467	0.466	-0.020	-0.024	-0.021	0.081	0.082	0.080	0.078	0.078	0.077
	Helicopter	0.449	0.445	0.445	0.013	0.030	0.035	0.072	0.071	0.072	0.064	0.064	0.063
	Talek	0.362	0.366	0.382	0.012	-0.009	-0.005	0.104	0.095	0.094	0.071	0.071	0.069
	V-section	0.167	0.166	0.175	-0.112	-0.104	-0.095	0.138	0.132	0.123	0.080	0.081	0.078
	Average	**0.603**	**0.603**	**0.603**	**-0.035**	**-0.031**	**-0.023**	**0.089**	**0.087**	**0.083**	**0.069**	**0.069**	**0.067**
SMOS	Mara-main	0.528	0.530	0.664	-0.046	-0.040	-0.013	0.099	0.106	0.070	0.099	0.098	0.069
	Mara-bridge	0.579	0.594	0.641	-0.021	-0.011	0.019	0.092	0.088	0.069	0.089	0.088	0.067
	Ashnil	0.604	0.605	0.626	-0.087	-0.090	-0.068	0.132	0.134	0.107	0.099	0.099	0.083
	Kissinger	0.533	0.533	0.545	-0.039	-0.029	0.017	0.107	0.105	0.083	0.100	0.100	0.082
	Upstream	0.424	0.427	0.362	-0.070	-0.059	-0.017	0.117	0.110	0.070	0.093	0.093	0.068
	Olimisigol	0.315	0.314	0.349	0.011	0.031	0.058	0.099	0.104	0.093	0.099	0.099	0.073
	Nice-bridge	0.183	0.183	0.316	-0.033	-0.040	-0.004	0.125	0.127	0.093	0.120	0.120	0.093
	Helicopter	0.144	0.145	0.294	-0.016	-0.003	0.031	0.104	0.104	0.072	0.103	0.103	0.065
	Talek	0.090	0.094	0.244	-0.004	-0.033	-0.007	0.114	0.118	0.077	0.114	0.113	0.077
	V-section	0.052	0.052	0.161	-0.117	-0.122	-0.103	0.113	0.164	0.130	0.110	0.110	0.080
	Average	**0.345**	**0.348**	**0.420**	**-0.042**	**-0.040**	**-0.009**	**0.110**	**0.116**	**0.087**	**0.103**	**0.103**	**0.075**
ASCAT	Mara-main	0.756	0.762	0.746	-0.008	0.009	-0.024	0.064	0.064	0.075	0.064	0.063	0.072
	Mara-bridge	0.855	0.855	0.852	-0.001	-0.001	-0.002	0.064	0.063	0.063	0.064	0.065	0.067
	Ashnil	0.879	0.879	0.881	-0.043	-0.045	-0.065	0.066	0.067	0.084	0.050	0.050	0.053
	Kissinger	0.795	0.795	0.798	-0.030	-0.026	-0.035	0.064	0.062	0.064	0.057	0.057	0.054
	Upstream	0.461	0.463	0.450	-0.060	-0.055	-0.063	0.087	0.084	0.087	0.063	0.063	0.060
	Olimisigol	0.657	0.659	0.655	0.021	0.032	0.031	0.065	0.069	0.068	0.061	0.061	0.060
	Nice-bridge	0.743	0.743	0.748	0.008	0.013	-0.024	0.055	0.056	0.059	0.054	0.054	0.054
	Helicopter	0.535	0.535	0.505	0.003	0.007	0.000	0.071	0.071	0.064	0.071	0.071	0.064
	Talek	0.649	0.650	0.645	0.041	0.026	-0.004	0.069	0.062	0.058	0.055	0.056	0.058
	V-section	0.424	0.427	0.497	-0.069	-0.073	-0.090	0.098	0.101	0.112	0.070	0.070	0.067
	Average	**0.675**	**0.677**	**0.678**	**-0.014**	**-0.011**	**-0.028**	**0.070**	**0.070**	**0.074**	**0.061**	**0.061**	**0.061**

The Mara-main station has the longest measurement compared with others, which was used here to do the time series analysis. For other stations' information please see Appendix B. Figure 5.20 illustrates the time series plot in Mara-main station for three different satellites together with their downscaled result. Compared with SMAP and SMOS, ASCAT catches the SM changing trend very well within the study period. This is because of the temporal resolution for SMAP and SMOS satellites are two or three days while the ASCAT has daily retrieved SM value.

Focusing the original products performances in Table 5.5, SMAP shows the best correlation coefficient of 0.807 which is followed by ASCAT (0.756), while SMOS is only 0.528 in this station. Considering the bias value for each satellite, a wet bias can be seen for all three satellites. There is higher bias for SMAP and SMOS with a value around 0.05 cm3 cm-3. For the ubRMSE result, all these three satellites cannot meet the accuracy requirement of 0.04 cm3 cm-3. However, SMAP and ASCAT have shown similar value around 0.07cm3 cm-3 while SMOS gave the most significant error. Some reasons causing the different

performances for three satellites based on the inter-comparison analysis as before. For the ASCAT satellite, the error mainly obtained from inaccurate porosity data used when converting the SMI to SM. While for the passive sensor, the model and auxiliary data difference all have the contribution to the distinct errors.

In Kenya, there are two rainy periods. The longer one occurs during April to June and short one is from October to December. This is also indicated from section 5.1, monthly precipitation time series plot. During the rainy season from March to June, SMAP has more error than the dry season and is concentrated in the time of rainfall event. This situation appeared for each station (see from Appendix B). It means SMAP tends to quickly respond to the rainfall and it is sensitive to the precipitation event. Besides, the biomass of vegetation increases during the wet season, which can significantly affect the SM result when using L-band microwave retrieval algorithms. Based on the tau-omega model used for SMAP, the vegetation will attenuate the signal from the soil. However, due to the huge amount of vegetation and the self-emission by itself. The microwave sensor will receive the signal from vegetation instead of the soil. In this case, the water content in the vegetation will count as the SM, resulting in the increase of SM value during rainfall period. This finding is consistent with that of Ma et al. (2017), which compared the active, passive and combined active passive SM performance over north-west part of China. They found the SM retrieval over bare soil has higher accuracy compared to dense vegetation land cover.

The same issue happened in SMOS, a wet trend can be seen during the wet season caused by the same reason as SMAP. However, there is more noise shown in the SMOS time series plot. From April to May, higher dynamic changes of SMOS occurs, the retrieved SM cannot catch the in-situ measurement change. Besides the wet season, extremely large value also appears from June to December. This situation can match the TC analysis result in the previous section, as SMOS has relatively low SNR and high error variance. Evidence shows the SMOS may be affected by radio frequency interference (RFI). RFI will affect the brightness temperature, then to cause the lower SM retrieval result. But this situation mainly happened in Europe and Asia, which may not be the real reason in this study (Muñoz-Sabater et al., 2014). Another reasonable explanation is based on the algorithm used by SMOS. The L-MEB model used by SMOS divided the surface cover into sparse, medium and dense vegetation. And empirical parameters are expected. Therefore, optical thickness derived from vegetation cannot respond to the seasonal change, causing the error accumulation during the iterative algorithm and making higher dynamic change of SM (Schlenz et al., 2012).

For ASCAT, a good correlation found from January to October. The ASCAT SM value has a very good match with in-situ measurement data and it also has a relatively small range change of SM value (from 0 to 0.4 cm3 cm-3). However, if we see the relationship between ASCAT SM and in-situ data around each rainfall event. ASCAT tend to overestimate the SM value during wet season. This may be caused by both the wet soil condition and roughness surface of the land. While during the dry season, there are lots of underestimated cases, even some zero value appears mostly between October to December. This situation matches Figure 5.8, and the mean SM is very low in these months which cannot respond to rainfall event. The mechanism for this phenomenon is not clear. But if we check the Appendix B, this phenomenon did not appear in Kissinger and Upstream stations. And, a clear overestimation occurs in these two stations from June to October. As such, if linked back to the porosity map, we again concluded that the spatial SM distribution of ASCAT is mainly dependent on porosity data.

In general, the passive satellites have a relatively poor performance during wet seasons because of the vegetation influence. ASCAT has the smallest dynamic change compared with SMAP and SMOS and it

can catch the temporal variability of in-situ measurement data. For SMOS, too much noise affect the accuracy of the original product.

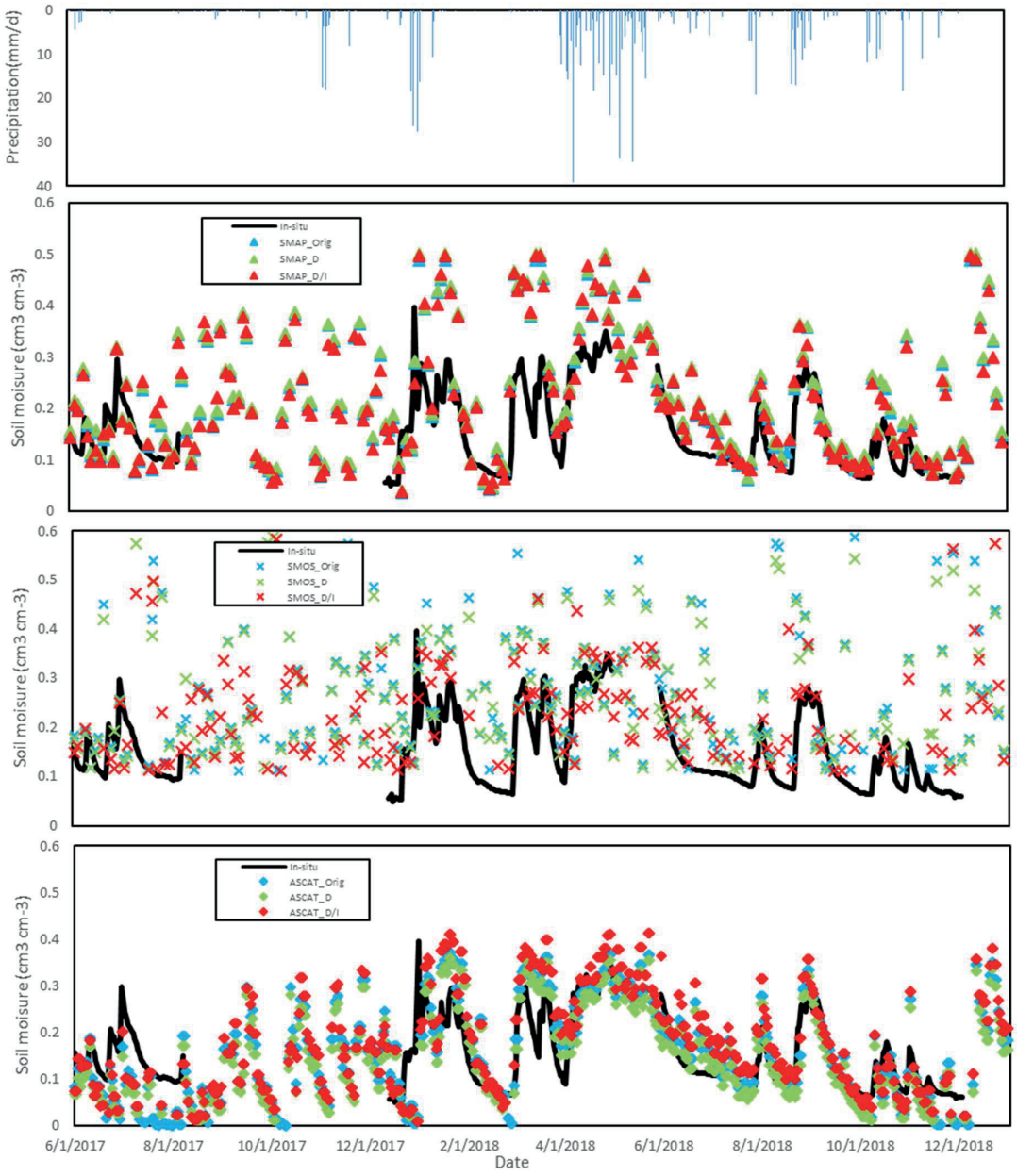

Figure 5.20 Time series plot for SMAP, SMOS and ASCAT against point data in the Mara-main station

According to downscaled result in Table 5.5 the performance of SMAP keep the same ubRMSE as original product while SMOS and ASCAT had a slight increase. This difference is very small which can almost be neglectable. Thus, after downscaling, there is almost no change in the performance of each satellite product. It is encouraging to compare this figure with research by Montzka et al., (2018), who found that there is no remarkable difference among original, downscaled and downscaled interpolated results.

From the time series plot (Figure 5.20), SMAP and ASCAT satellites have a quite similar result with the original one. The original and downscaled time series plots are almost overlaying each other. While for SMOS, the downscaled result shows a clear gap with the original product mostly under wet SM condition while perform similar for the rest. This result can be linked with the SM variability analysis for SMOS, which has the biggest SM variability compared with SMAP and ASCAT. Also, when the SM is bigger than 0.45, extremely higher SM variability happened to cause the distinct difference between the original product and the downscaled one.

If we now turn to the interpolated result after downscaling, we see similar values for SMAP and ASCAT, while with a significant change for SMOS. A reasonable explanation is that SMOS has the biggest spatial resolution that causes larger gap between grid cells after downscaling, which can also be seen from Appendix A downscaled image results. The interpolated result is strongly influenced by the neighbor pixel value, which will lead to a large difference between the interpolated and original one. Also, for the statistical analysis output, SMOS ubRMSE has a significant decrease from 0.98 to 0.69 cm3 cm-3.

These results indicate that the sub-grid downscaling method depends on the heterogeneity of the soil, if there has more dynamic change of the soil texture, more significant difference can be seen from the downscaled result. However, according to the homogeneous study area in this research, the downscaled result almost keeps the same value as the original products. Therefore, the quality of original products has a decisive effect on the downscaled result.

5.4.2. Validation against CRNP SM data

Table 5.6 gives the validation result for SMAP, SMOS and ASCAT against the CRNP SM and point measurement in Mara-main station. The clearest change between point and CRNP SM is that the bias convert from negative to positive for all products, it means the CRNP SM is much higher than the point measurement in this case. This situation also can be seen from Figure 5.21, although the CRNP SM has the similar trend with point measurement data within the year of 2018, there is a clear gap between the CRNP SM and point measurement data. Under the same condition, the SM retrieved from CRNP has much higher value compared with point measurement.

Considering the ubRMSE difference, the satellites validation result become worse for ASCAT and SMOS, while for the SMAP, a slightly increase can be seen in this station. This is caused by the relatively higher trend of SMAP compared with the other two satellites. For the downscaled result, CRNP SM still keeps a similar result as original one. Because there is only one site measurement, this validation result does not have a good representation.

Table 5.6 Validation metrics for SMAP, SMOS and ASCAT in Mara-main station with CRNP and point SM

Product	Measurement ways	R			Bias			RMSE			ubRMSE		
		Orig	D	D/I	Orig	D	D/I	Orig	D	D/I	Orig	D	D/I
SMAP	CRNP	0.852	0.851	0.841	0.056	0.051	0.062	0.088	0.085	0.094	0.068	0.068	0.071
	Point	0.864	0.863	0.859	-0.067	-0.073	-0.061	0.096	0.101	0.094	0.070	0.070	0.072
SMOS	CRNP	0.226	0.202	0.499	0.040	0.049	0.093	0.146	0.146	0.137	0.140	0.138	0.101
	Point	0.593	0.595	0.716	-0.060	-0.055	-0.024	0.112	0.109	0.071	0.095	0.095	0.067
ASCAT	CRNP	0.841	0.843	0.843	0.105	0.122	0.084	0.121	0.136	0.104	0.061	0.061	0.062
	Point	0.858	0.860	0.852	-0.022	-0.004	-0.042	0.050	0.050	0.070	0.050	0.050	0.056

Figure 5.21 illustrates the time series plot of CRNP retrieved SM with different satellites products. Combined with the time series plot from previous section the only difference is that the CRNP SM data tend to be relative higher but with the similar trend.

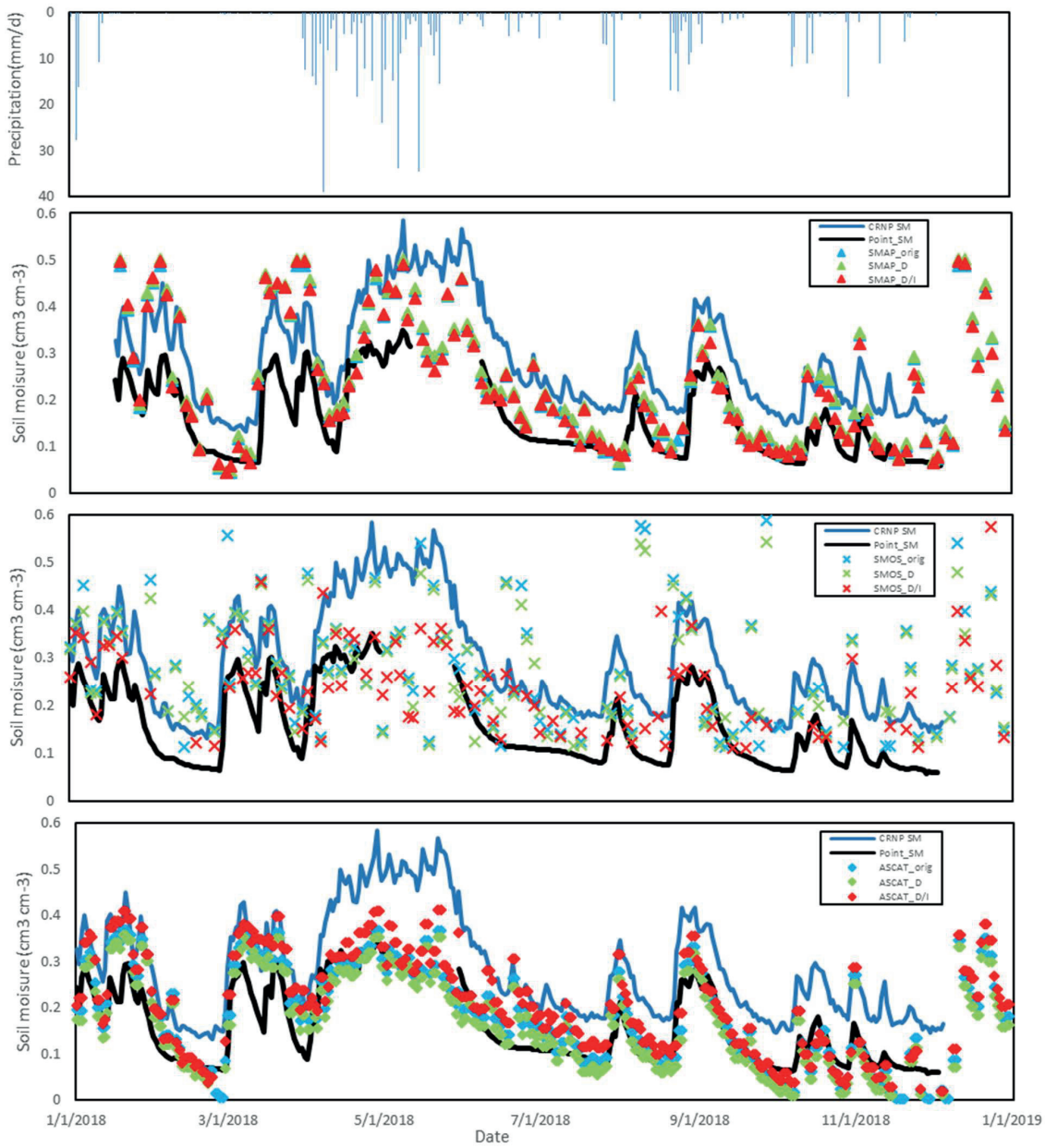

Figure 5.21 Time series plot for SMAP, SMOS and ASCAT against CRNP and point SM data over Mara-main station

The reason behind this situation is that the CRNP is not only measuring the 5cm soil moisture as FDR, its measurement depth depends on the water content in the soil. Previous research by Zreda et al., (2008) found that the effective depth under dry soil is 70cm while 12cm under the wet soil. Based on Zreda et al., Franz et al., (2012) developed a function to quantify the effective depth of CRNP. Equation as:

$$z(\theta) = \frac{5.8}{\theta + 0.0829} \quad (in\ cm) \tag{5-2}$$

Where $z(\theta)$ stands for the effective depth under specific soil moisture condition; θ stands for the retrieved SM from CRNP.

Based on this equation, the effective depth was calculated in the Mara-main station. An inversely relationship can be seen from Figure 5.22, and the smallest depth in this case is still bigger than 10 cm. The satellite penetration depth for ASCAT is around 2cm while for SMOS and SMAP is less than 5cm. Therefore, compared with the satellites, the "penetration depth" for CRNP is much larger causing mismatch with the remote sensing satellite products.

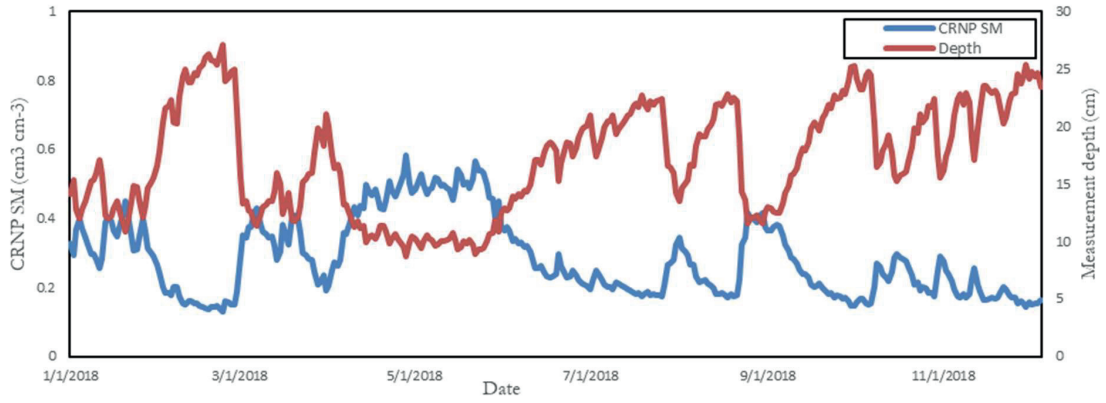

Figure 5.22 Time series plot for CRNP SM and effective depth

Besides the depth mismatch, some problems still need to be solved for CRNP. Most importantly, the detected water content by CRNP is not only existing in the soil moisture. Because the hydrogen atoms also can be found in lattice water, organic matter, water vapor and vegetation, which will influence the fast neutron spread (Zreda et al., 2008) . Although some of these effects can be eliminated by the field soil moisture correction, there is no quantitative formula to solve this problem, correction of these influence factors still stands for a key point for the CRNP application.

5.5. Overall discussion and limitation

5.5.1. Discussion

The sub-grid downscaling method is mainly depending on the SM variability within the footprint for each satellite based on the soil texture. According to Vereecken et al. (2007) who analyzed the SM variability under eleven soil classes, the pore size distribution strongly affects the SM variability and its relationship between soil water content. With the coarse soil texture, SM variability will continually increase with mean SM while it reached the maximum value under the moderate wetness condition for finer soil type. In this research, the results are in agreement with previous findings, as n parameter is the most sensitive parameter for the SM variability and it can control the shape of relationship curve between SM variability and mean SM. However, because of the homogeneity of the study area, this convex relationship obtained from this study area cannot represent other soil texture/types.

Also, based on Vereecken et al. (2007), SM variability is not only affected by the soil texture, but also linked with the environmental conditions. Vereecken et al. (2007) pointed out that the precipitation can significantly influence the range of SM then lead to the different SM variability under the same soil texture condition. The environmental factors like vegetation, evapotranspiration or topography have an influence on the SM variability change (Gray, 2010; Teuling & Troch, 2005; Wang, 2014). The environmental conditions were also considered in this research, as soil-grids maps were obtained not only from soil profiles data but also from MODIS and SRTM (Hengl et al., 2014), which was used to derive hydraulic parameters by PTF.

The coarse resolution SM products can be downscaled by sub-grids variability since the soil texture is a dominant factor to the SM variability change. The downscaling result mainly depends on the heterogeneity of the coarse pixel. The more dynamic change of soil texture within a coarse pixel the clearer downscaled effect can be seen. The downscaled result in this study is not clear as SM variability change within the whole study area is very small with a max value of 0.015cm3 cm-3, which lead to almost the same SM value obtained for the downscaled result. This result is in agreement with Montzka's (2018) findings which showed the SM variability tightly affected by the heterogeneities.

This study also tries to understand why three SM satellite products have different performance? and what is the performance for each satellite product when compared with ground measurement data? There are many factors that cause the different performance for the three satellites (e.g., satellite sensors/instruments, algorithms and input data). It is too difficult to split them to do the analysis. Based on the correlation analysis, SMAP and ASCAT show higher similarities than that between SMAP and SMOS. This situation may be caused by inaccurate retrieved SM value of SMOS in the south-west area since the higher error variance also can be seen in the same region. It means more dynamic change of SMOS compared with SMAP and ASCAT. In addition, the land cover map used for SMOS and SMAP shows the significant difference which can also influence the inconsistent SM result for passive products. The former one used ECOCLIMAP which has 213 classes while latter one applied MODIS IGBP with only 17 classes. This hypothesis supports evidence from previous observation (Al-Yaari et al., 2017).

For the TC analysis, SMAP shows the lowest error variance followed by ASCAT. While SMOS still has the worst performance within the whole area compared with other two satellites. Considering the TC result for ten measurement station, it can reflect part of the validation result. Since the SMAP and ASCAT have relatively better performance while SMOS shows poor result. The TC analysis can be an effective tool to evaluate the remote sensing SM dataset for large area.

Since SMAP and SMOS used L-band observation while ASCAT used the C-band, the passive products should be affected less by the vegetation because of the larger penetration capacity (Lannoy et al., 2013). However, the validation result shows an opposite situation. ASCAT has better performance under the dense vegetation condition while SMAP is suitable for moderate and bare land. Previous work also found the same result by comparing the radiometer and scatterometer system (Brocca et al., 2011; Rüdiger et al., 2009; Rötzer et al., 2012). From Wagner et al. (2010), the higher difference of backscatter under dry and wet condition obtained from grassland and cropland, causing better SM estimate result, which accordant with the result in this research. Al-Yaari et al. (2014)explained the possible reason: firstly, the higher-order surface-vegetation interaction effect may increase the sensitivity of active products on the SM detection; secondly, ASCAT has good ability to catch the seasonal vegetation change.

For the validation result in this research, it is difficult to say whether the CRNP or point measurement data is more reliable. However, considering their applications for validating the satellite products, the measurement depth is an essential point to pay attentions. For the FDR measurement, it directly gives 5cm SM data, but CRNP SM depends on the soil moisture condition of the soil and even under the wet condition the effective depth is bigger than 10cm. Also, CRNP is affected by the environmental factors, causing the inaccurate estimate of the SM value (Zreda et al., 2008). More researchers working on the weighting function to quantify the contribution of different depths and horizontal samples in order to better understand the detail of the CRNP signal (Köhli et al., 2015; Schrön et al., 2017).

Based on this research, ASCAT and SMAP have better performance than SMOS. In addition, SMAP and SMOS tend to have more error under dense vegetation condition while ASCAT underestimated the SM during the dry situation.

5.5.2. Limitation

Some limitations should be noted in this research. Firstly, the downscaling method strongly depends on soil-grids data. However, it is difficult to verify the accuracy of this data, which may cause an unpredictable error during downscaling. Secondly, the homogeneity of the study area and insufficient in-situ data limit the validation activities.

6. CONCLUSION

In this study, the method proposed by Qu et al. (2015) was used to predict the SM variability of SMAP, SMOS and ASCAT SM products within the Massai Mara region in Kenya. This method is based on the stochastic analysis of steady-state unsaturated flow provided by Zhang et al. (1998). Static field capacity map derived from soil map with 1km spatial resolution was used as proxy data to downscale the coarse SM products. Then, both original and downscaled products were validated against the FDR and CRNP SM data.

Based on the inter-comparison analysis among three satellites, there are many factors that affect the quality of SM products (e.g. satellite sensor/instruments, algorithms and auxiliary data). The SMAP and SMOS have similar SM spatial distribution pattern while ASCAT product is dominated by the porosity data. From the TC analysis, SMAP has the best performance followed by ASCAT. While SMOS shown higher noise over south-west part of study area caused by the heterogeneity land cover map.

A convex relationship obtained between mean SM and SM variability under both clay loam and sandy clay loam within the study area. Through sensitivity analysis, the pore size distribution parameter (n) is the most sensitive to the change of SM variability. The highest variability occurs around 0.2 cm3 cm-3 mean SM condition with a relatively low value below 0.015 cm3 cm-3. By comparing the downscaled result with original products, detailed sub-grid SM pattern can be seen. However, the SM value did not change so much compared with original products because of the homogeneity of the study area.

Validation result shows that these three original satellite products cannot meet the required accuracy of 0.04 cm3 cm-3. ASCAT has the best performance with ubRMSE value of 0.061 cm3 cm-3 followed by SMAP with a similar result (0.069 cm3 cm-3), the SMOS has the worst performance with 0.103 cm3 cm-3 ubRMSE. In addition, CRNP tend to retrieve the SM from deeper soil (more than 10cm), which cannot match the measurement depth from satellite SM products. For the downscaled result, slightly better or at least same result were obtained. Therefore, this sub-grid variability method can be used to downscale coarse microwave SM products and the accuracy of downscaled result still mainly depends on the quality of original products.

LIST OF REFERENCES

Aaron Hawdon, D. M. & J. wallace. (2014). Calibration and correction procedures for cosmic-ray neutron soil moisture probes located across Australia. *Water Resources Research*, *50*, 1–17. https://doi.org/10.1002/2013WR014333.Received

Abbaszadeh, P., Moradkhani, H., & Zhan, X. (2018). Downscaling SMAP Radiometer Soil Moisture over the CONUS Using an Ensemble Learning Method. *Water Resources Research*, (55), 2018WR023354. https://doi.org/10.1029/2018WR023354

Ahlmer, A. K., Cavalli, M., Hansson, K., Koutsouris, A. J., Crema, S., & Kalantari, Z. (2018). Soil moisture remote-sensing applications for identification of flood-prone areas along transport infrastructure. *Environmental Earth Sciences*, *77*(14), 1–17. https://doi.org/10.1007/s12665-018-7704-z

Al-Yaari, A., Wigneron, J. P., Ducharne, A., Kerr, Y., de Rosnay, P., de Jeu, R., … Mialon, A. (2014). Global-scale evaluation of two satellite-based passive microwave soil moisture datasets (SMOS and AMSR-E) with respect to Land Data Assimilation System estimates. *Remote Sensing of Environment*, *149*, 181–195. https://doi.org/10.1016/j.rse.2014.04.006

Al-Yaari, A., Wigneron, J. P., Ducharne, A., Kerr, Y. H., Wagner, W., De Lannoy, G., … Mialon, A. (2014). Global-scale comparison of passive (SMOS) and active (ASCAT) satellite based microwave soil moisture retrievals with soil moisture simulations (MERRA-Land). *Remote Sensing of Environment*, *152*, 614–626. https://doi.org/10.1016/j.rse.2014.07.013

Al-Yaari, A., Wigneron, J. P., Kerr, Y., Rodriguez-Fernandez, N., O'Neill, P. E., Jackson, T. J., … Yueh, S. (2017). Evaluating soil moisture retrievals from ESA's SMOS and NASA's SMAP brightness temperature datasets. *Remote Sensing of Environment*, *193*, 257–273. https://doi.org/10.1016/j.rse.2017.03.010

Baatz, R., Bogena, H. R., Hendricks Franssen, H.-J., Huisman, J. A., Qu, W., Montzka, C., & Vereecken, H. (2014). Calibration of a catchment scale cosmic-ray probe network: A comparison of three parameterization methods. *Journal of Hydrology*, *516*, 231–244. https://doi.org/10.1016/j.jhydrol.2014.02.026

Bhola, N., Ogutu, J. O., Piepho, H. P., Said, M. Y., Reid, R. S., Hobbs, N. T., & Olff, H. (2012). Comparative changes in density and demography of large herbivores in the Masai Mara Reserve and its surrounding human-dominated pastoral ranches in Kenya. *Biodiversity and Conservation*, *21*(6), 1509–1530. https://doi.org/10.1007/s10531-012-0261-y

Brocca, L., Crow, W. T., Ciabatta, L., Massari, C., De Rosnay, P., Enenkel, M., … Wagner, W. (2017). A Review of the Applications of ASCAT Soil Moisture Products. *IEEE Journal of Selected Topics in Applied Earth Observations and Remote Sensing*, *10*(5), 2285–2306. https://doi.org/10.1109/JSTARS.2017.2651140

Brocca, L., Hasenauer, S., Lacava, T., Melone, F., Moramarco, T., Wagner, W., … Bittelli, M. (2011). Soil moisture estimation through ASCAT and AMSR-E sensors: An intercomparison and validation study across Europe. *Remote Sensing of Environment*, *115*(12), 3390–3408. https://doi.org/10.1016/j.rse.2011.08.003

Chakrabarti, S., Bongiovanni, T., Judge, J., Nagarajan, K., & Principe, J. C. (2015). Downscaling satellite-based soil moisture in heterogeneous regions using high-resolution remote sensing products and information theory: A synthetic study. *IEEE Transactions on Geoscience and Remote Sensing*, *53*(1), 85–101. https://doi.org/10.1109/TGRS.2014.2318699

Champeaux, J. L., Masson, V., & Chauvin, F. (2005). ECOCLIMAP: A global database of land surface parameters at 1 km resolution. *Meteorological Applications*, *12*(1), 29–32. https://doi.org/10.1017/S1350482705001519

Chen, F., Crow, W. T., Bindlish, R., Colliander, A., Burgin, M. S., Asanuma, J., & Aida, K. (2018). Global-scale evaluation of SMAP, SMOS and ASCAT soil moisture products using triple collocation. *Remote Sensing of Environment*, *214*(March), 1–13. https://doi.org/10.1016/j.rse.2018.05.008

Colliander, A., Jackson, T. J., Bindlish, R., Chan, S., Das, N., Kim, S. B., … Yueh, S. (2017). Validation of SMAP surface soil moisture products with core validation sites. *Remote Sensing of Environment*, *191*, 215–231. https://doi.org/10.1016/j.rse.2017.01.021

Crow, W. T., Berg, A. A., Cosh, M. H., Loew, A., Mohanty, B. P., Panciera, R., … Walker, J. P. (2012). Upscaling sparse ground-based soil moisture observations for the validation of coarse-resolution satellite soil moisture products. *Reviews of Geophysics*, *50*(2), 1–20. https://doi.org/10.1029/2011RG000372

Das, N. N., Entekhabi, D., Member, S., & Njoku, E. G. (2015). An Algorithm for Merging SMAP Radiometer and Radar Data for High-Resolution Soil-Moisture Retrieval. *IEEE Transactions on Geoscience and Remote Sensing*, *49*(5), 1504–1512. https://doi.org/10.1109/TGRS.2010.2089526

De Lannoy, G. J. M., Reichle, R. H., & Pauwels, V. R. N. (2013). Global calibration of the geos-5 l-band microwave radiative transfer model over nonfrozen land using smos observations. *Journal of Hydrometeorology*, *14*(3), 765–785. https://doi.org/10.1175/JHM-D-12-092.1

Desilets, D., & Zreda, M. (2003). Spatial and temporal distribution of secondary cosmic-ray nucleon intensities and applications to in situ cosmogenic dating. https://doi.org/10.1016/S0012-821X(02)01088-9

Desilets, D., Zreda, M., & Ferré, T. P. A. (2010). Nature's neutron probe: Land surface hydrology at an elusive scale with cosmic rays. *Water Resources Research*, *46*(11), 7. https://doi.org/10.1029/2009WR008726

Djamai, N., Magagi, R., Goïta, K., Hosseini, M., Cosh, M. H., Berg, A., & Toth, B. (2015). Evaluation of SMOS soil moisture products over the CanEx-SM10 area. *Journal of Hydrology*, *520*, 254–267. https://doi.org/10.1016/j.jhydrol.2014.11.026

Djamai, N., Magagi, R., Goïta, K., Merlin, O., Kerr, Y., & Roy, A. (2016). A combination of DISPATCH downscaling algorithm with CLASS land surface scheme for soil moisture estimation at fine scale during cloudy days. *Remote Sensing of Environment*, *184*, 1–14. https://doi.org/10.1016/j.rse.2016.06.010

Dong, J., Ochsner, T. E., Zreda, M., Cosh, M. H., & Zou, C. B. (2014). Calibration and validation of the COSMOS rover for surface soil moisture measurement. *Vadose Zone Journal*, *13*(4), 1–8. https://doi.org/10.2136/vzj2013.08.0148

Dorigo, W., Wagner, W., Albergel, C., Albrecht, F., Balsamo, G., Brocca, L., … Lecomte, P. (2017). ESA CCI Soil Moisture for improved Earth system understanding: State-of-the art and future directions. *Remote Sensing of Environment*, *203*, 185–215. https://doi.org/10.1016/j.rse.2017.07.001

El Hajj, M., Baghdadi, N., Zribi, M., Rodríguez-Fernández, N., Wigneron, J. P., Al-Yaari, A., … Calvet, J. C. (2018). Evaluation of SMOS, SMAP, ASCAT and Sentinel-1 soil moisture products at sites in Southwestern France. *Remote Sensing*, *10*(4), 1–17. https://doi.org/10.3390/rs10040569

Entekhabi, D., Das, N. N., & Njoku, E. (2014). Soil Moisture Active Passive (SMAP) Algorithm Theoretical Basis Document SMAP L2 & L3 Radar Soil Moisture (Active) Data Products, 1–82.

Entekhabi, D., Njoku, E. G., O'Neill, P. E., Kellogg, K. H., Crow, W. T., Edelstein, W. N., … Van Zyl, J. (2010). The soil moisture active passive (SMAP) mission. *Proceedings of the IEEE*, *98*(5), 704–716. https://doi.org/10.1109/JPROC.2010.2043918

Fang, B., Lakshmi, V., Bindlish, R., & Jackson, T. J. (2018). AMSR2 soil moisture downscaling using temperature and vegetation data. *Remote Sensing*, *10*(10). https://doi.org/10.1016/0020-7225(73)90076-1

Fascetti, F., Pierdicca, N., Pulvirenti, L., Crapolicchio, R., & Muñoz-Sabater, J. (2016). A comparison of ASCAT and SMOS soil moisture retrievals over Europe and Northern Africa from 2010 to 2013. *International Journal of Applied Earth Observation and Geoinformation*, *45*, 135–142. https://doi.org/10.1016/j.jag.2015.09.008

Fernandez-Moran, R., Al-Yaari, A., Mialon, A., Mahmoodi, A., Al Bitar, A., De Lannoy, G., … Wigneron, J. P. (2017). SMOS-IC: An alternative SMOS soil moisture and vegetation optical depth product. *Remote Sensing*, *9*(5), 1–21. https://doi.org/10.3390/rs9050457

Franz, T. E., Zreda, M., Ferre, T. P. A., Rosolem, R., Zweck, C., Stillman, S., … Shuttleworth, W. J. (2012). Measurement depth of the cosmic ray soil moisture probe affected by hydrogen from various sources. *Water Resources Research*, *48*(8), 1–9. https://doi.org/10.1029/2012WR011871

Gray, R. T. (2010). On the structure of soil moisture time series in the context of land surface models. *Journal of Hydrology*, *83*(1), 38–57. https://doi.org/10.1016/S0022-1694(00)00405-4

Griesfeller, A., Lahoz, W. A., Jeu, R. A. M. d., Dorigo, W., Haugen, L. E., Svendby, T. M., & Wagner, W. (2016). Evaluation of satellite soil moisture products over Norway using ground-based observations. *International Journal of Applied Earth Observation and Geoinformation*, *45*, 155–164. https://doi.org/10.1016/j.jag.2015.04.016

Gruber, A., Su, C., Zwieback, S., Crow, W., Dorigo, W., & Wagner, W. (2016). International Journal of Applied Earth Observation and Geoinformation Recent advances in (soil moisture) triple collocation analysis. *International Journal of Applied Earth Observation and Geoinformation*, *45*, 200–211. https://doi.org/10.1016/j.jag.2015.09.002

Gwak, Y., & Kim, S. (2017). Factors affecting soil moisture spatial variability for a humid forest hillslope.

Hydrological Processes, *31*(2), 431–445. https://doi.org/10.1002/hyp.11039
Hengl, T., De Jesus, J. M., MacMillan, R. A., Batjes, N. H., & Heuvelink, G. B. M. (2014). Correction: SoilGrids1km - Global soil information based on automated mapping. *PLoS ONE*, *9*(12), 114788. https://doi.org/10.1371/journal.pone.0114788
Hupet, F., & Vanclooster, M. (2002). Intraseasonal dynamics of soil moisture variability within a small agricultural maize cropped field. *Journal of Hydrology*, *261*, 86–101. https://doi.org/10.1016/S0022-1694(02)00016-1
Im, J., Park, S., Rhee, J., Baik, J., & Choi, M. (2016). Downscaling of AMSR-E soil moisture with MODIS products using machine learning approaches. *Environmental Earth Sciences*, *75*(15), 1120. https://doi.org/10.1007/s12665-016-5917-6
International Atomic Energy Agency. (2017). *Cosmic Ray Neutron Sensing: Use, Calibration and Validation for Soil Moisture Estimation*.
Jin, Y., Ge, Y., Wang, J., Chen, Y., Heuvelink, G. B. M., & Atkinson, P. M. (2018). Downscaling AMSR-2 soil moisture data with geographically weighted area-to-area regression kriging. *IEEE Transactions on Geoscience and Remote Sensing*, *56*(4), 2362–2376. https://doi.org/10.1109/TGRS.2017.2778420
Jin, Y., Ge, Y., Wang, J., & Heuvelink, G. B. M. (2018). Deriving temporally continuous soil moisture estimations at fine resolution by downscaling remotely sensed product. *International Journal of Applied Earth Observation and Geoinformation*, *68*(December 2017), 8–19. https://doi.org/10.1016/j.jag.2018.01.010
Kaheil, Y. H., Gill, M. K., McKee, M., Bastidas, L. A., & Rosero, E. (2008). Downscaling and assimilation of surface soil moisture using ground truth measurements. *IEEE Transactions on Geoscience and Remote Sensing*, *46*(5), 1375–1384. https://doi.org/10.1109/TGRS.2008.916086
Kerr, Y. H., Member, S., Waldteufel, P., Richaume, P., Wigneron, J. P., Member, S., … Delwart, S. (2012). The SMOS Soil Moisture Retrieval Algorithm. *Ieee Transactions on Geoscience and Remote Sensing*, *50*(5), 1384–1403. https://doi.org/10.1016/0167-2789(89)90206-6
Köhli, M., Schrön, M., Zreda, M., Schmidt, U., Dietrich, P., & Zacharias, S. (2015). Footprint characteristics revised for field-scale soil moisture monitoring with cosmic-ray neutrons. *Water Resources Research*, *51*(7), 5772–5790. https://doi.org/10.1002/2015WR017169
Kwon, M., Kwon, H. H., & Han, D. (2018). A spatial downscaling of soil moisture from rainfall, temperature, and AMSR2 using a Gaussian-mixture nonstationary hidden Markov model. *Journal of Hydrology*, *564*, 1194–1207. https://doi.org/10.1016/j.jhydrol.2017.12.015
Lawrence, J. E., & Hornberger, G. M. (2007). Soil moisture variability across climate zones. *Geophysical Research Letters*, *34*(20), 1–5. https://doi.org/10.1029/2007GL031382
Li, J., Wang, S., Gunn, G., Joosse, P., & Russell, H. A. J. (2018). A model for downscaling SMOS soil moisture using Sentinel-1 SAR data. *International Journal of Applied Earth Observation and Geoinformation*, *72*(July), 109–121. https://doi.org/10.1016/j.jag.2018.07.012
Ma, C., Li, X., Wei, L., & Wang, W. (2017). Multi-scale validation of SMAP soil moisture products over cold and arid regions in Northwestern China using distributed ground observation data. *Remote Sensing*, *9*(4). https://doi.org/10.3390/rs9040327
Martinez, G., Pachepsky, Y. A., Vereecken, H., Hardelauf, H., Herbst, M., & Vanderlinden, K. (2013). Modeling local control effects on the temporal stability of soil water content. *Journal of Hydrology*, *481*, 106–118. https://doi.org/10.1016/j.jhydrol.2012.12.024
Mascaro, G., Vivoni, E. R., & Deidda, R. (2010). Downscaling soil moisture in the southern Great Plains through a calibrated multifractal model for land surface modeling applications. *Water Resources Research*, *46*(8), 1–18. https://doi.org/10.1029/2009WR008855
McColl, K. A., Alemohammad, S. H., Akbar, R., Konings, A. G., Yueh, S., & Entekhabi, D. (2017). The global distribution and dynamics of surface soil moisture. *Nature Geoscience*, *10*(2), 100–104. https://doi.org/10.1038/ngeo2868
Miernecki, M., Wigneron, J. P., Lopez-Baeza, E., Kerr, Y., De Jeu, R., De Lannoy, G. J. M., … Richaume, P. (2014). Comparison of SMOS and SMAP soil moisture retrieval approaches using tower-based radiometer data over a vineyard field. *Remote Sensing of Environment*, *154*(1), 89–101. https://doi.org/10.1016/j.rse.2014.08.002
Mishra, V., Ellenburg, W. L., Griffin, R. E., Mecikalski, J. R., Cruise, J. F., Hain, C. R., & Anderson, M. C. (2018). An initial assessment of a SMAP soil moisture disaggregation scheme using TIR surface evaporation data over the continental United States. *International Journal of Applied Earth Observation and Geoinformation*, *68*(November 2017), 92–104. https://doi.org/10.1016/j.jag.2018.02.005
Montzka, C., Bogena, H. R., Zreda, M., Monerris, A., Morrison, R., Muddu, S., & Vereecken, H. (2017).

Validation of spaceborne and modelled surface soil moisture products with Cosmic-Ray Neutron Probes. *Remote Sensing*, *9*(2), 1–30. https://doi.org/10.3390/rs9020103

Montzka, C., Bogena, H. R., Zreda, M., Monerris, A., Uhqfk, Q. G. R., Iru, H. O. O., … Wr, F. (2017). Cosmic-ray neutron probes for satellite soil moisture validation. *IEEE International Geoscience and Remote Sensing Symposium (IGARSS)*, 3–6. https://doi.org/10.1109/IGARSS.2017.8127866

Montzka, C., Rötzer, K., Bogena, H. R., Sanchez, N., & Vereecken, H. (2018). A new soil moisture downscaling approach for SMAP, SMOS, and ASCAT by predicting sub-grid variability. *Remote Sensing*, *10*(3). https://doi.org/10.3390/rs10030427

Muñoz-Sabater, J., De Rosnay, P., Jiménez, C., Isaksen, L., & Albergel, C. (2014). SMOS brightness temperature angular noise: Characterization, filtering, and validation. *IEEE Transactions on Geoscience and Remote Sensing*, *52*(9), 5827–5839. https://doi.org/10.1109/TGRS.2013.2293200

Nasta, P., Penna, D., Brocca, L., Zuecco, G., & Romano, N. (2018). Downscaling near-surface soil moisture from field to plot scale: A comparative analysis under different environmental conditions. *Journal of Hydrology*, *557*, 97–108. https://doi.org/10.1016/j.jhydrol.2017.12.017

Ogutu, J. O., Owen-Smith, N., Piepho, H. P., & Said, M. Y. (2011). Continuing wildlife population declines and range contraction in the Mara region of Kenya during 1977-2009. *Journal of Zoology*, *285*(2), 99–109. https://doi.org/10.1111/j.1469-7998.2011.00818.x

Owe, M., & Van De Griend, A. A. (1998). Comparison of soil moisture penetration depths for several bare soils at two microwave frequencies and implications for remote sensing. *Water Resources Research*, *34*(9), 2319–2327. https://doi.org/10.1029/98WR01469

Peng, J., Loew, A., Merlin, O., & Verhoest, N. E. C. (2017). A review of spatial downscaling of satellite remotely sensed soil moisture. *Reviews of Geophysics*, *55*(2), 341–366. https://doi.org/10.1002/2016RG000543

Peng, J., Niesel, J., & Loew, A. (2015). Evaluation of soil moisture downscaling using a simple thermal-based proxy – the REMEDHUS network (Spain) example. *Hydrology and Earth System Sciences*, *19*(12), 4765–4782. https://doi.org/10.5194/hess-19-4765-2015

Pierdicca, N., Pulvirenti, L., Fascetti, F., Crapolicchio, R., & Talone, M. (2013). Analysis of two years of ASCAT- and SMOS-derived soil moisture estimates over Europe and North Africa. *European Journal of Remote Sensing*, *46*(1), 759–773. https://doi.org/10.5721/EuJRS20134645

Qu, W., H.R.Bogena, J.A.Huisman, J.Vanderborght, M.Schuh, E.Priesack, and H. V. (2015). Predicting subgrid variability of soil water content from basic soil information. *Geophysical Research Letters*, 0–7. https://doi.org/10.1002/2014GL062496

R. Baatz, H. R. Bogena, H.-J. Hendricks Franssen, J. A. Huisman, C. Montzka, and H. V. (2007). An empirical vegetation correction for soil water content quantification using cosmic ray probes. *Water Resources Research*, *5*(3), 2–2. https://doi.org/10.1111/j.1752-1688.1969.tb04897.x

Ranney, K. J., Niemann, J. D., Lehman, B. M., Green, T. R., & Jones, A. S. (2015). A method to downscale soil moisture to fine resolutions using topographic, vegetation, and soil data. *Advances in Water Resources*, *76*, 81–96. https://doi.org/10.1016/j.advwatres.2014.12.003

Rawls, W. J., & Brakensiek, D. L. (n.d.). Prediction of soil water properties for hydrologic modeling. In *Proceedings of the Symposium on Watershed Management in the Eighties, New York, NY, USA, 1985, 293–299, 1985*.

Ren, J., Xie, L., Li, W. W., & Bourne, P. E. (2010). SMAP-WS: A parallel web service for structural proteome-wide ligand-binding site comparison. *Nucleic Acids Research*, *38*(SUPPL. 2), 441–444. https://doi.org/10.1093/nar/gkq400

Robinson, D. A., Campbell, C. S., Hopmans, J. W., Hornbuckle, B. K., Jones, S. B., Knight, R., … Wendroth, O. (2008). Soil moisture measurement for ecological and hydrological watershed-scale observatories: A review. *Vadose Zone Journal*, *7*(1), 358–389. https://doi.org/10.2136/vzj2007.0143

Rüdiger, C., Calvet, J.-C., Gruhier, C., Holmes, T. R. H., de Jeu, R. A. M., & Wagner, W. (2009). An Intercomparison of ERS-Scat and AMSR-E Soil Moisture Observations with Model Simulations over France. *Journal of Hydrometeorology*, *10*(2), 431–447. https://doi.org/10.1175/2008JHM997.1

Schaap, M. G., & van Genuchten, M. T. (2006). A Modified Mualem–van Genuchten Formulation for Improved Description of the Hydraulic Conductivity Near Saturation. *Vadose Zone Journal*, *5*(1), 27. https://doi.org/10.2136/vzj2005.0005

Schlenz, F., Dall'Amico, J. T., Mauser, W., & Loew, A. (2012). Analysis of SMOS brightness temperature and vegetation optical depth data with coupled land surface and radiative transfer models in Southern Germany. *Hydrology and Earth System Sciences*, *16*(10), 3517–3533. https://doi.org/10.5194/hess-16-3517-2012

Schrön, M., Köhli, M., Scheiffele, L., Iwema, J., Bogena, H. R., Lv, L., … Zacharias, S. (2017). Improving calibration and validation of cosmic-ray neutron sensors in the light of spatial sensitivity. *Hydrology and Earth System Sciences*, *21*(10), 5009–5030. https://doi.org/10.5194/hess-21-5009-2017

Scipal, K., Dorigo, W., & De Jeu, R. (2010). Triple collocation - A new tool to determine the error structure of global soil moisture products. *International Geoscience and Remote Sensing Symposium (IGARSS)*, *3*(2), 4426–4429. https://doi.org/10.1109/IGARSS.2010.5652128

Sm, L. P., Sm, L. P., & Neill, P. O. (2012). Soil Moisture Active Passive (SMAP) Algorithm Theoretical Basis Document (ATBD) SMAP Level 2 & 3 Soil Moisture (Passive), 1–75.

Srivastava, P. K., Han, D., Ramirez, M. R., & Islam, T. (2013). Machine Learning Techniques for Downscaling SMOS Satellite Soil Moisture Using MODIS Land Surface Temperature for Hydrological Application. *Water Resources Management*, *27*(8), 3127–3144. https://doi.org/10.1007/s11269-013-0337-9

Stoffelen, A. (1998). Toward the true near-surface wind speed: Error modeling and calibration using triple collocation. *Journal of Geophysical Research: Oceans*, *103*(C4), 7755–7766. https://doi.org/10.1029/97JC03180

Susha Lekshmi, S. U., Singh, D. N., & Shojaei Baghini, M. (2014). A critical review of soil moisture measurement. *Measurement: Journal of the International Measurement Confederation*, *54*, 92–105. https://doi.org/10.1016/j.measurement.2014.04.007

Teuling, A. J., & Troch, P. A. (2005). Improved understanding of soil moisture variability dynamics. *Geophysical Research Letters*, *32*(5), 1–4. https://doi.org/10.1029/2004GL021935

Velde, R. Van Der, Salama, M. S., Eweys, O. A., Wen, J., & Wang, Q. (2014). Soil Moisture Mapping Using Combined Active/Passive Microwave Observations Over the East of the Netherlands. *IEEE*, *8*(9). https://doi.org/10.1109/JSTARS.2014.2353692

Vereecken, H., Kamai, T., Harter, T., Kasteel, R., Hopmans, J., & Vanderborght, J. (2007). Explaining soil moisture variability as a function of mean soil moisture: A stochastic unsaturated flow perspective. *Geophysical Research Letters*, *34*(22), 1–6. https://doi.org/10.1029/2007GL031813

Vereecken, H., Schnepf, A., Hopmans, J. W., Javaux, M., Or, D., Roose, T., … Young, I. M. (2016). Modeling Soil Processes: Review, Key Challenges, and New Perspectives. *Vadose Zone Journal*, *15*(5), 57. https://doi.org/10.2136/vzj2015.09.0131

Vereencken, M. & F. (1988). Perioperative alcohol withdrawal syndrome associated with a myocardial revascularization procedure. *Journal of Cardiothoracic Anesthesia*, *2*(4), 492–496. https://doi.org/10.1097/00010694-199001000-00001

Wagner, B., Tarnawski, V. R., Hennings, V., Müller, U., Wessolek, G., & Plagge, R. (2001). Evaluation of pedo-transfer functions for unsaturated soil hydraulic conductivity using an independent data set. *Geoderma*, *102*(3–4), 275–297. https://doi.org/10.1016/S0016-7061(01)00037-4

Wagner, W., Bartalis, Z., Naeimi, V., Park, S. E., Figa-Saldaña, J., & Bonekamp, H. (2010). Status of the Metop ASCAT soil moisture product. *International Geoscience and Remote Sensing Symposium (IGARSS)*, 276–279. https://doi.org/10.1109/IGARSS.2010.5653358

Wagner, W., Hahn, S., Kidd, R., Melzer, T., Bartalis, Z., Hasenauer, S., … Rubel, F. (2013). The ASCAT soil moisture product: A review of its specifications, validation results, and emerging applications. *Meteorologische Zeitschrift*, *22*(1), 5–33. https://doi.org/10.1127/0941-2948/2013/0399

Wang, T. (2014). Modeling the impacts of soil hydraulic properties on temporal stability of soil moisture under a semi-arid climate. *Journal of Hydrology*, *519*(PA), 1214–1224. https://doi.org/10.1016/j.jhydrol.2014.08.052

Wang, T., Franz, T. E., Zlotnik, V. A., You, J., & Shulski, M. D. (2015). Investigating soil controls on soil moisture spatial variability: Numerical simulations and field observations. *Journal of Hydrology*, *524*, 576–586. https://doi.org/10.1016/j.jhydrol.2015.03.019

Wen, J., & Su, Z. (2003). A time series based method for estimating relative soil moisture with ERS wind scatterometer data. *Geophysical Research Letters*, *30*(7). https://doi.org/10.1029/2002GL016557

Wösten, J. H. M., Lilly, A., Nemes, A., & Le Bas, C. (1999). Development and use of a database of hydraulic properties of European soils. *Geoderma*, *90*(3–4), 169–185. https://doi.org/10.1016/S0016-7061(98)00132-3

Xu, C., Qu, J. J., Hao, X., Cosh, M. H., Prueger, J. H., Zhu, Z., & Gutenberg, L. (2018). Downscaling of surface soil moisture retrieval by combining MODIS/Landsat and in situ measurements. *Remote Sensing*, *10*(2). https://doi.org/10.3390/rs10020210

Zhang, D., Wallstrom, T. C., & Winter, C. L. (1998). Stochastic analysis of steady-state unsaturated flow in heterogeneous media: Comparison of the Brooks-Corey and Gardner-Russo models, *34*(c), 1–3.

Zhao, H., Zeng, Y., Lv, S., & Su, Z. (2018). Analysis of soil hydraulic and thermal properties for land surface modeling over the Tibetan Plateau. *Earth System Science Data*, *10*(2), 1031–1061. https://doi.org/10.5194/essd-10-1031-2018

Zhao, W., Sánchez, N., Lu, H., & Li, A. (2018). A spatial downscaling approach for the SMAP passive surface soil moisture product using random forest regression. *Journal of Hydrology*, *563*(April), 1009–1024. https://doi.org/10.1016/j.jhydrol.2018.06.081

Zreda, M., Desilets, D., Ferré, T. P. A., & Scott, R. L. (2008). Measuring soil moisture content non-invasively at intermediate spatial scale using cosmic-ray neutrons. *Geophysical Research Letters*, *35*(21), 1–5. https://doi.org/10.1029/2008GL035655

Zreda, M., Shuttleworth, W. J., Zeng, X., Zweck, C., Desilets, D., Franz, T., & Rosolem, R. (2012). COSMOS: The cosmic-ray soil moisture observing system. *Hydrology and Earth System Sciences*, *16*(11), 4079–4099. https://doi.org/10.5194/hess-16-4079-2012

APPENDIX A

SMAP

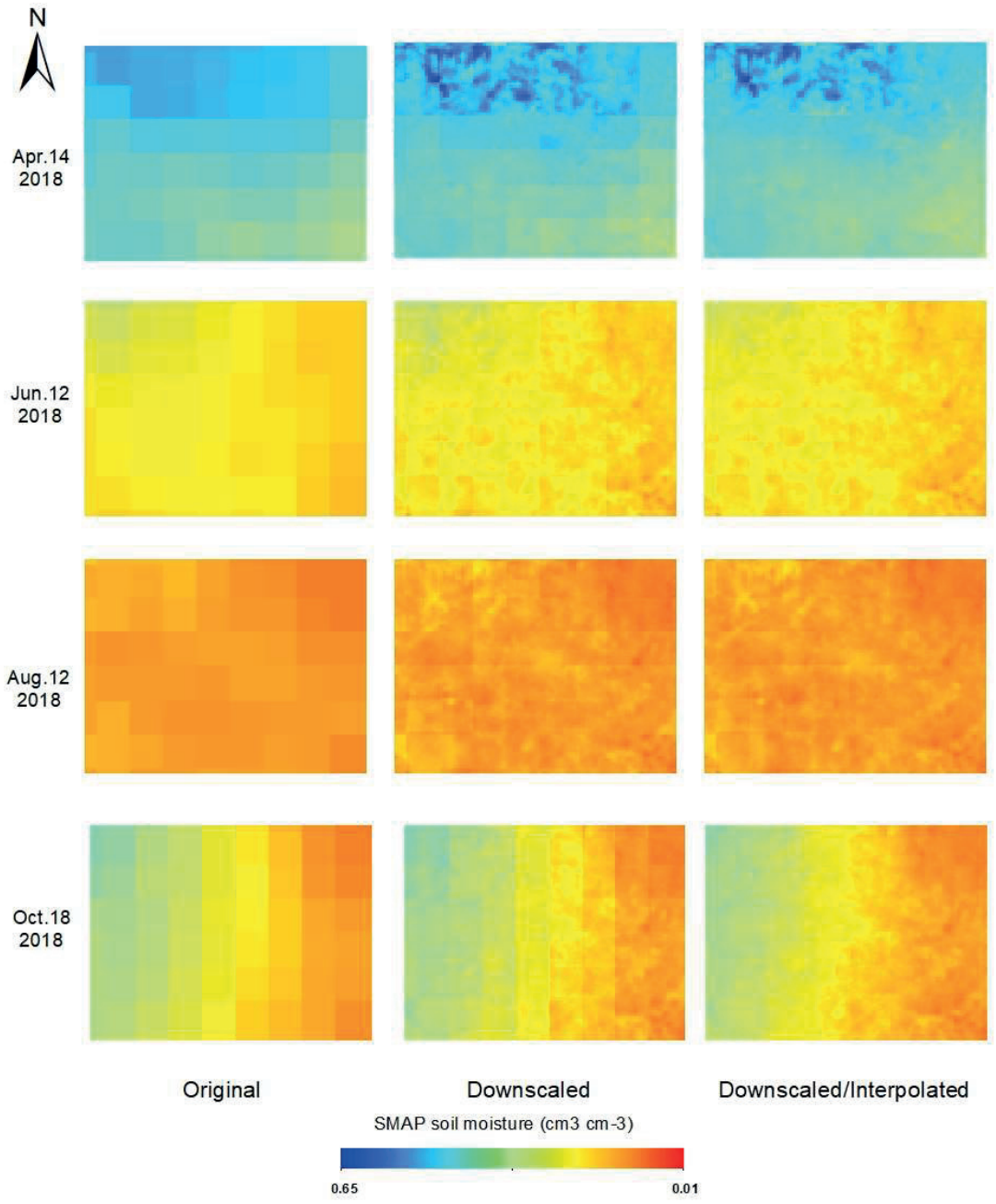

SMOS

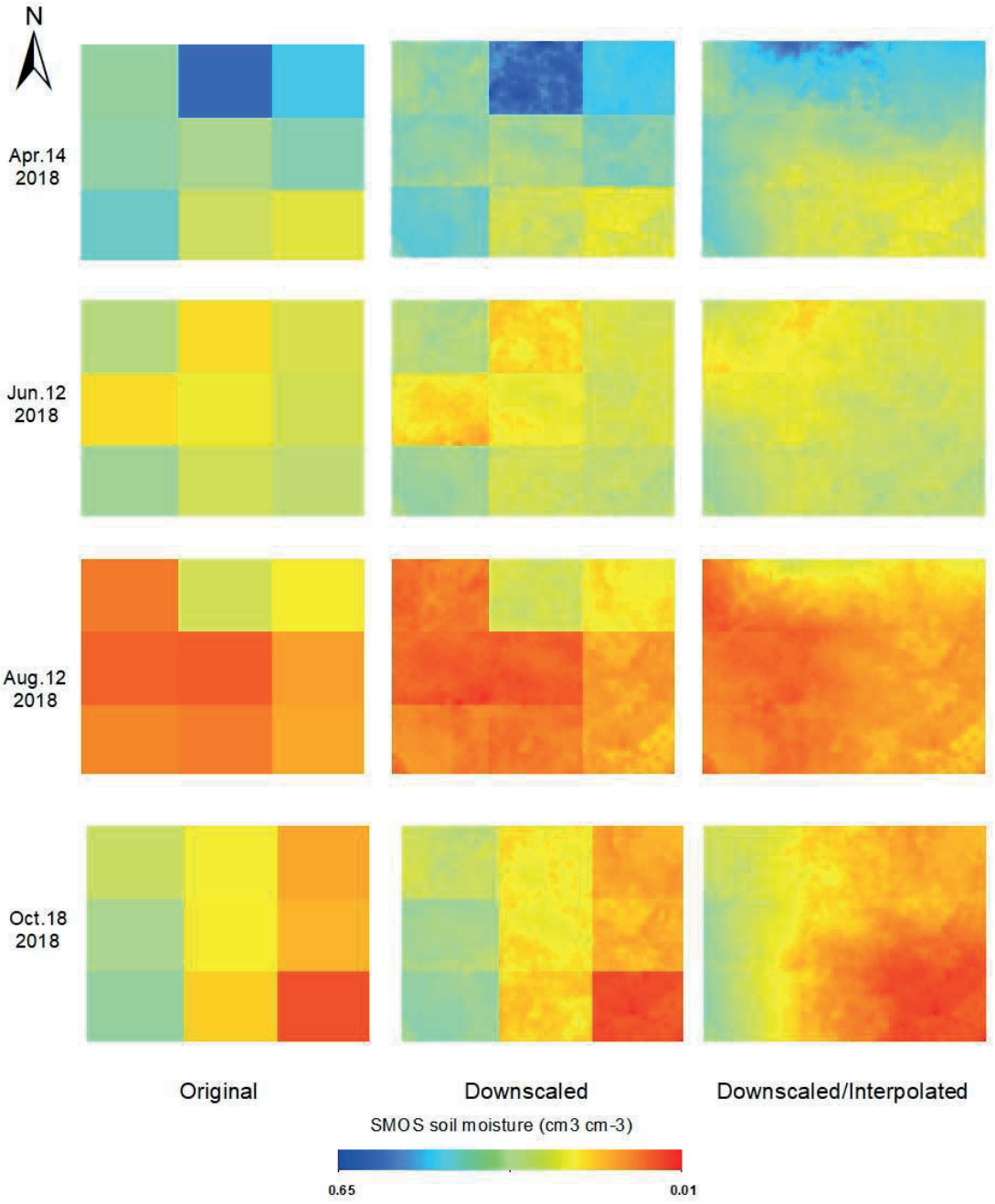
N
Apr.14
2018
Jun.12
2018
Aug.12
2018
Oct.18
2018
Original
Downscaled
Downscaled/Interpolated
SMOS soil moisture (cm3 cm-3)
0.65
0.01

ASCAT

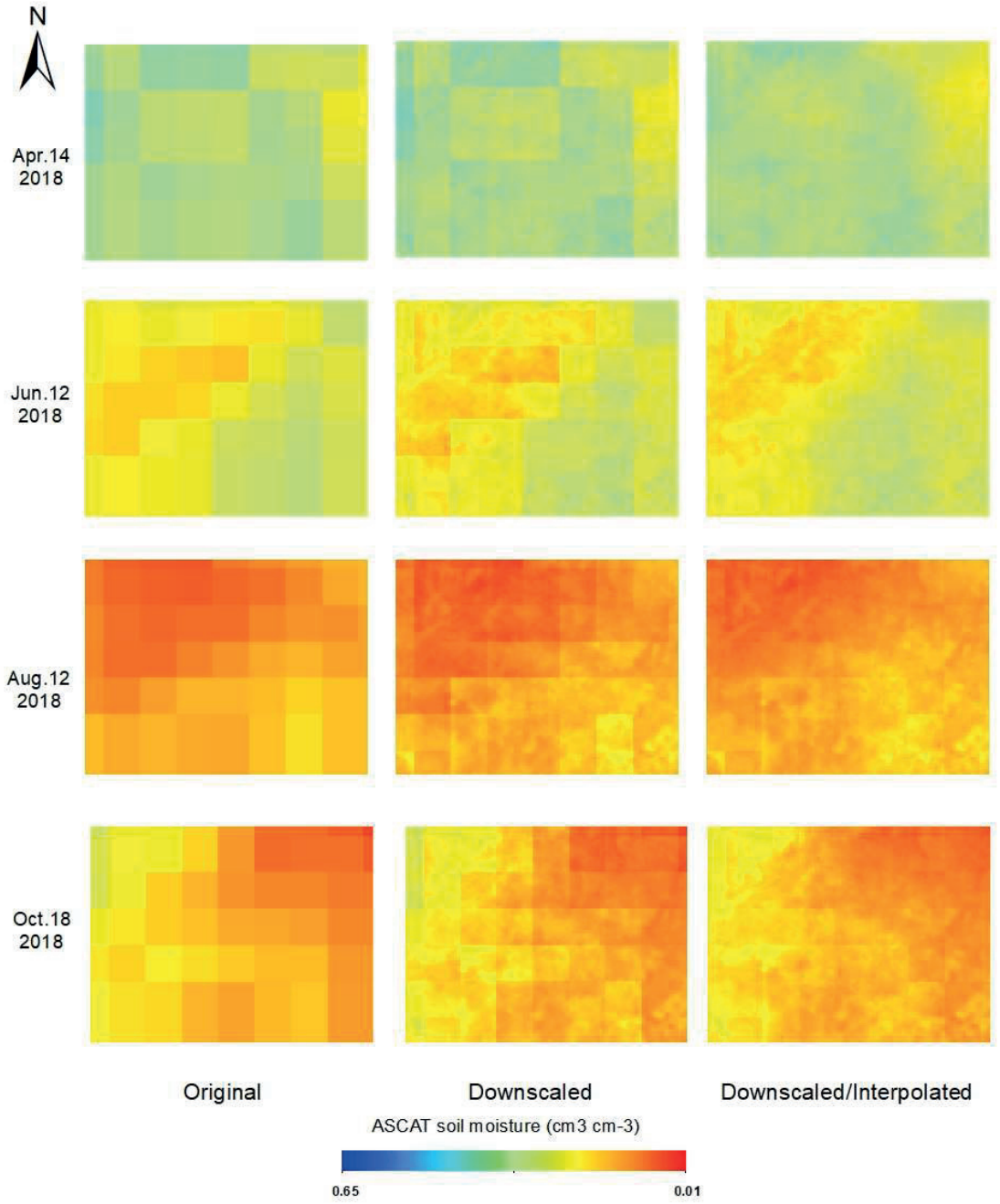

Appendix 1 SM downscaling image result

APPENDIX B

Talek station

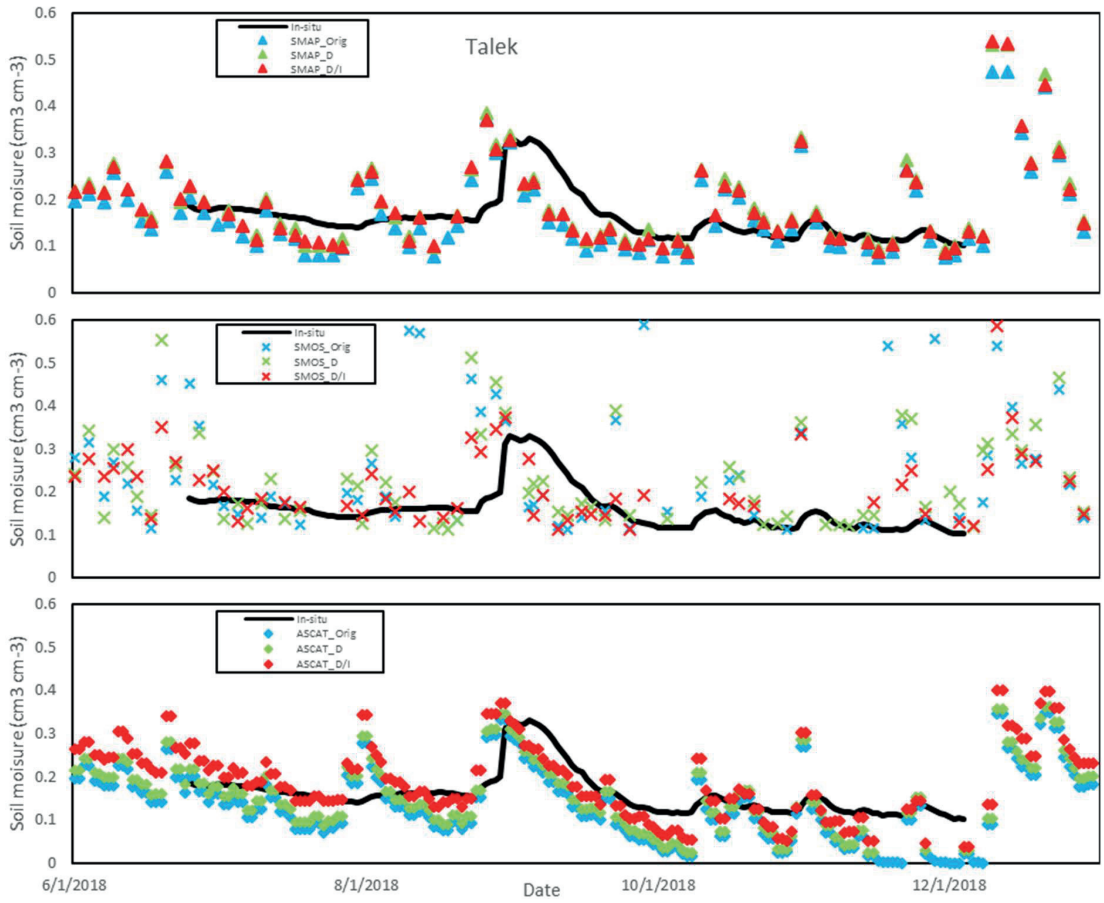

V-section

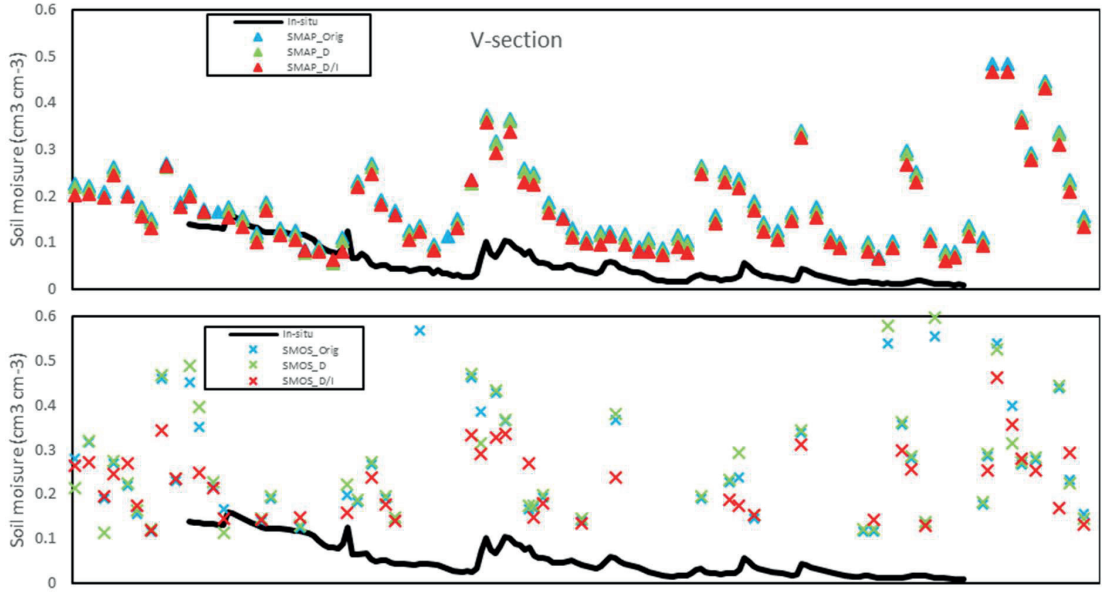

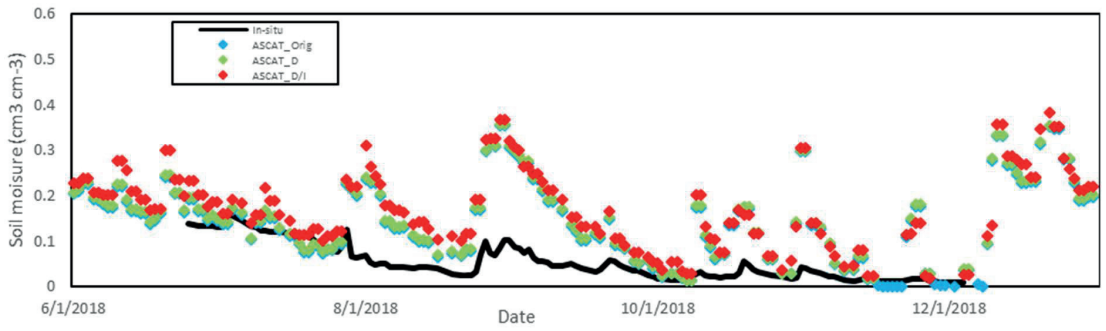

Helicopter

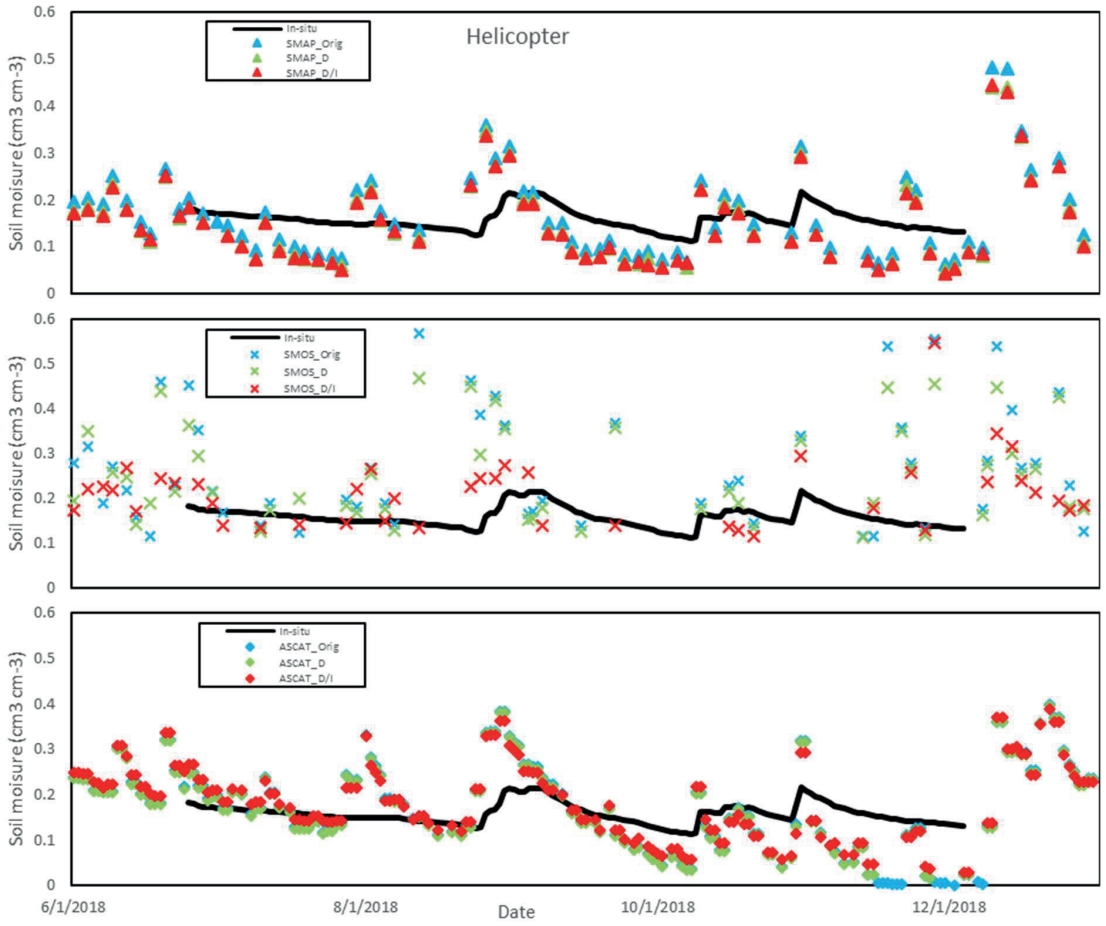

Kissinger

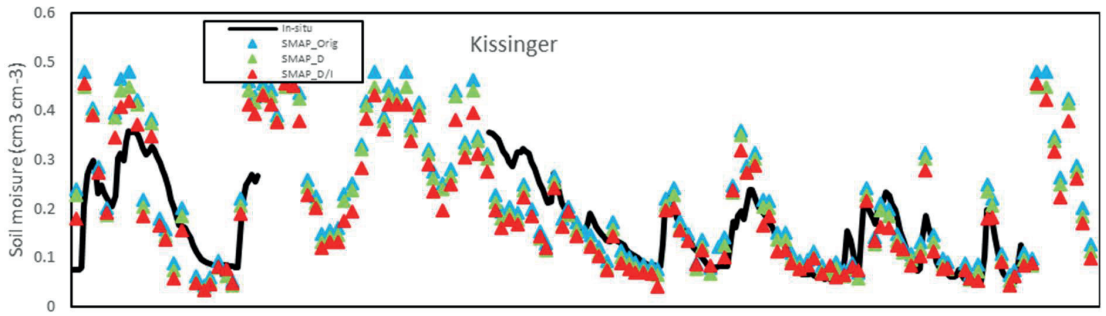

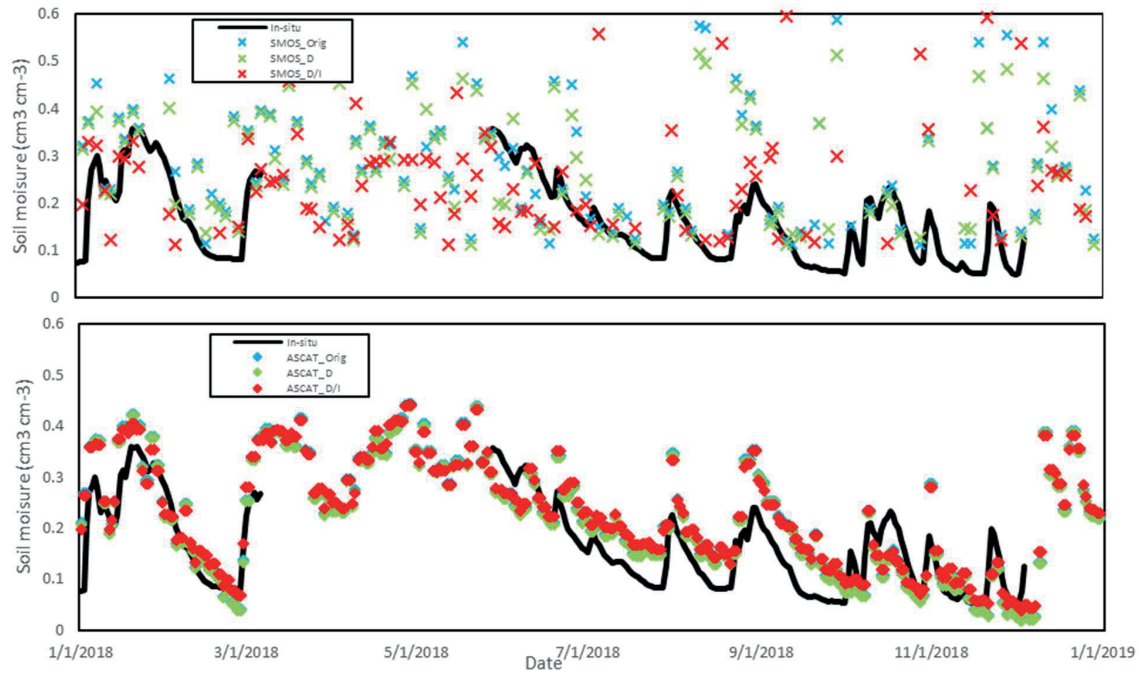
In-situ
SMOS_Orig
SMOS_D
SMOS_D/I
Soil moisure (cm3 cm-3)
0
0.1
0.2
0.3
0.4
0.5
0.6
In-situ
ASCAT_Orig
ASCAT_D
ASCAT_D/I
Soil moisure (cm3 cm-3)
1/1/2018
3/1/2018
5/1/2018
7/1/2018
9/1/2018
11/1/2018
1/1/2019
Date

Olimsigiol

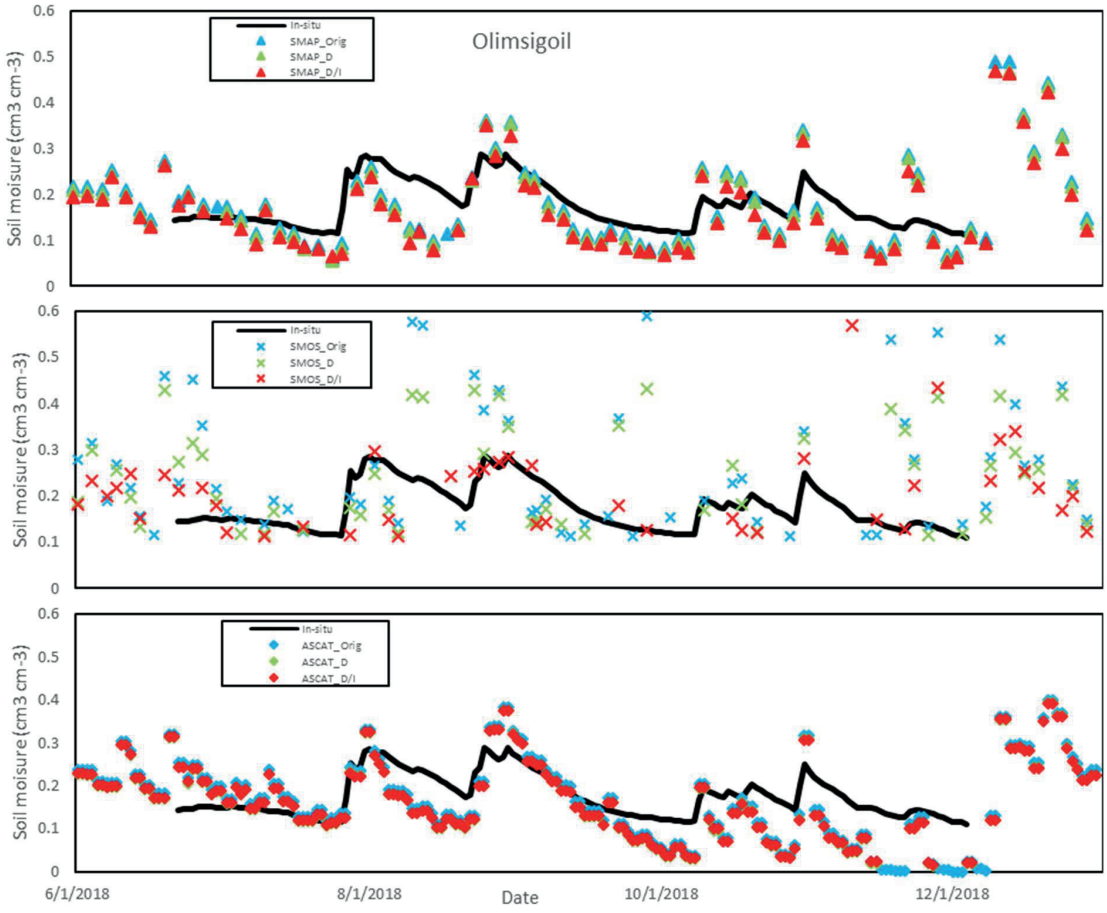
Olimsigoil
In-situ
SMAP_Orig
SMAP_D
SMAP_D/I
Soil moisure (cm3 cm-3)
In-situ
SMOS_Orig
SMOS_D
SMOS_D/I
Soil moisure (cm3 cm-3)
In-situ
ASCAT_Orig
ASCAT_D
ASCAT_D/I
Soil moisure (cm3 cm-3)
0
0.1
0.2
0.3
0.4
0.5
0.6
6/1/2018
8/1/2018
10/1/2018
12/1/2018
Date

Upstream

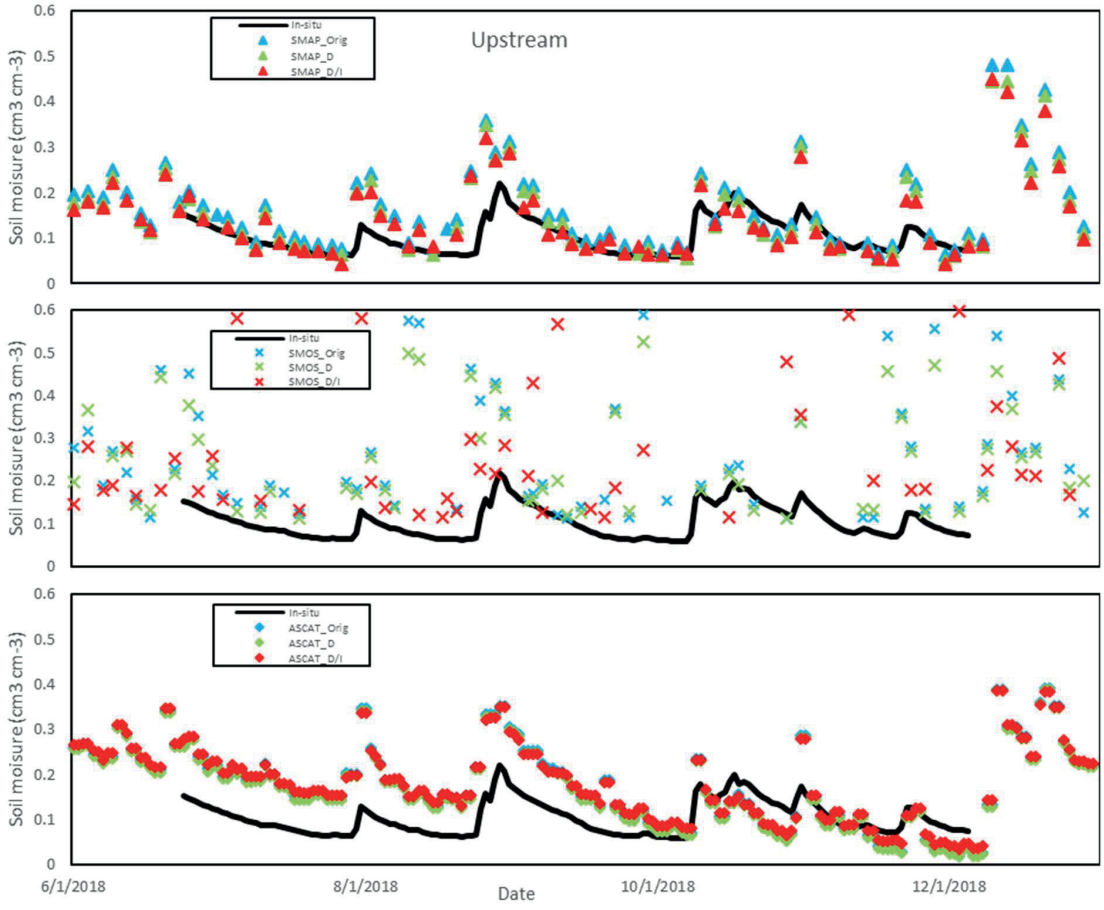

Ashnil

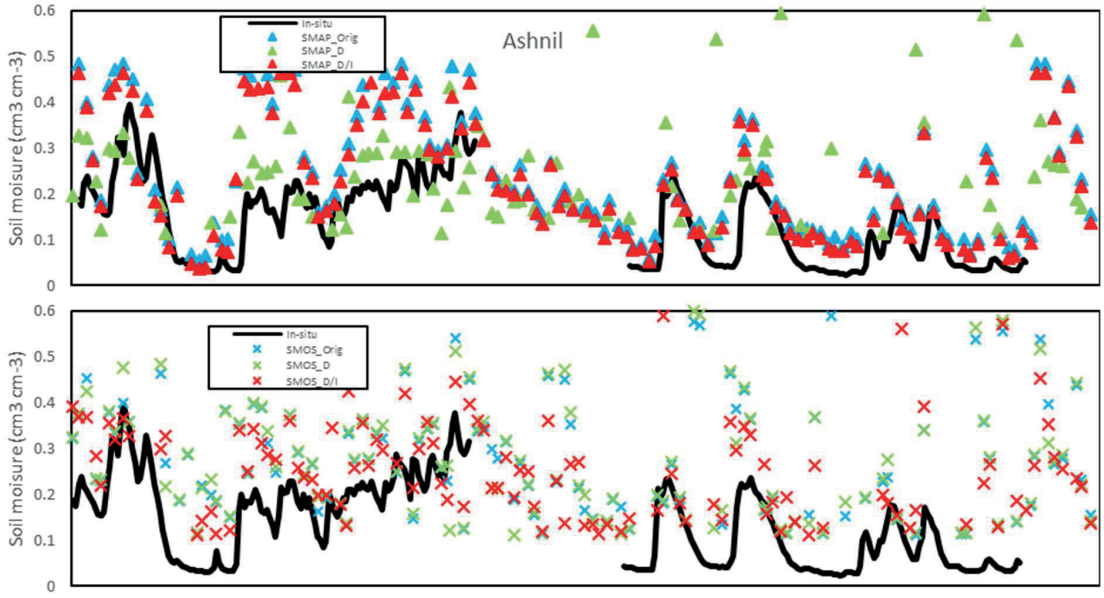

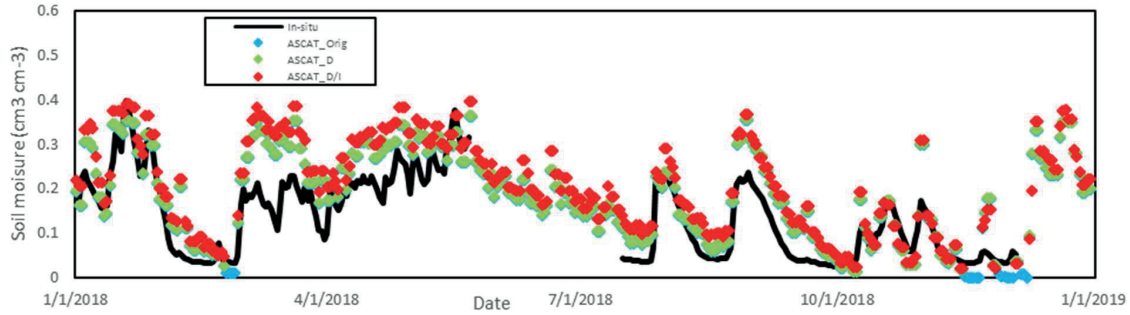

Nice-bridge

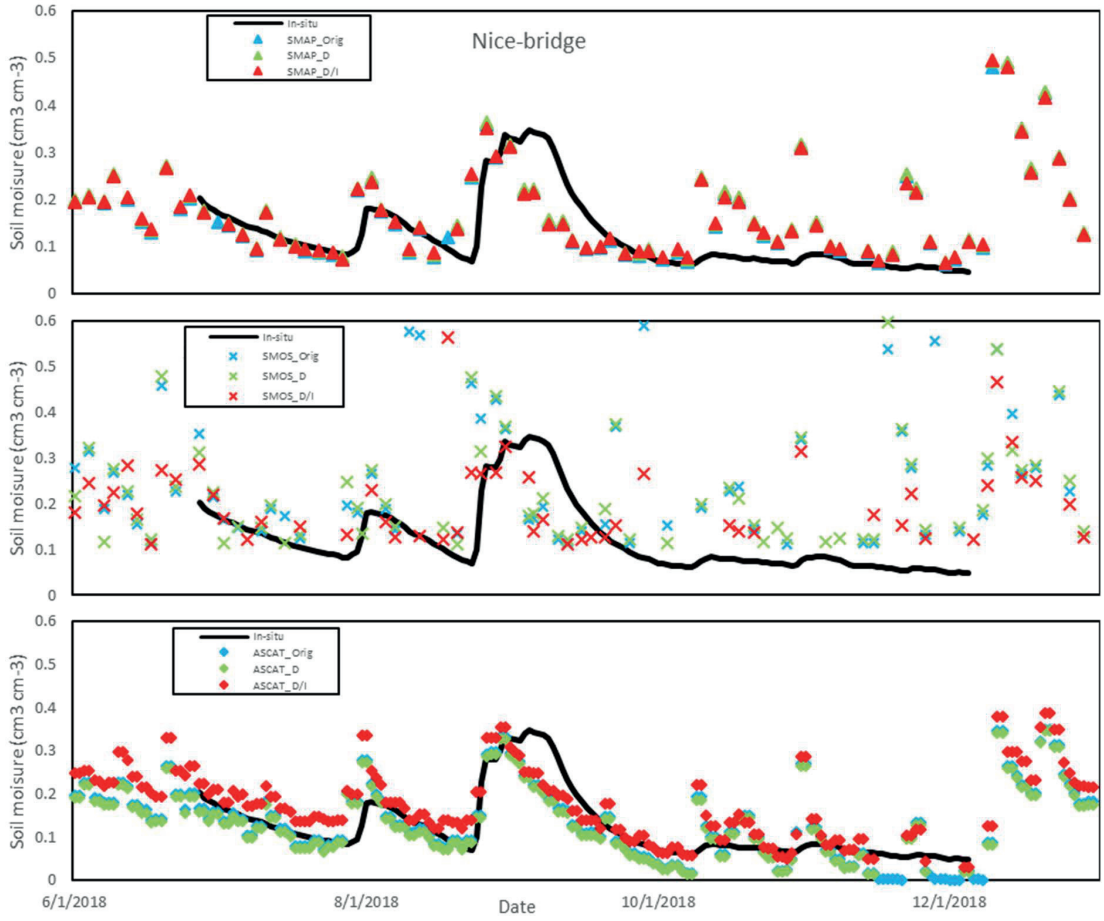

Appendix 2 Time series plot for each station

APPENDIX C

Because of the same land cover used, it cannot be the dominant factor to show the difference between SM products. Based on the soil texture map from FAO, only Mara-bridge station belongs to vertisol soil texture, which contains more clay fraction. Therefore, Mara-bridge station was chosen here to do the comparison of the Main station.

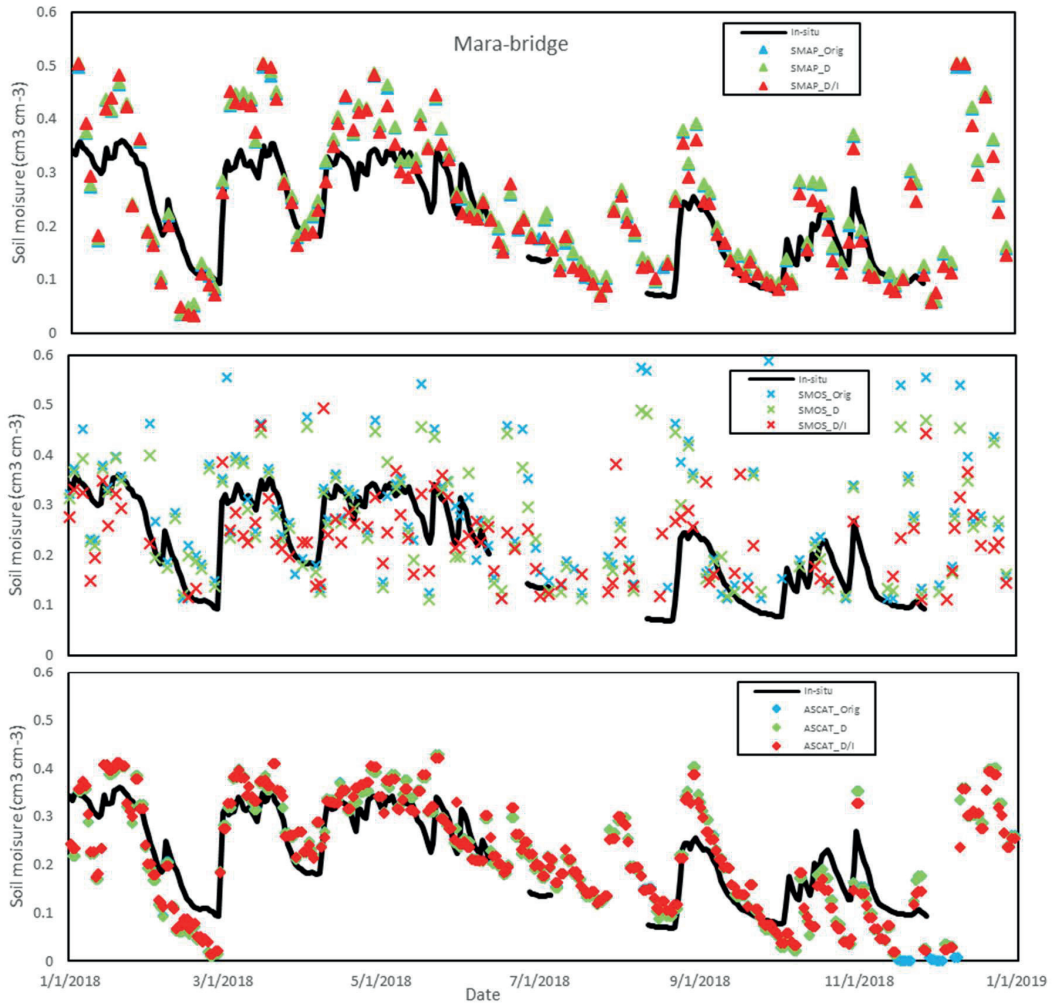

Appendix 3 Time series plot for SMAP, SMOS and ASCAT against point data in Mara-bridge station

Appendix 3 indicates the time series plot for three satellites against in-situ measurement in station Mara-bridge. The SM trend is similar to the Main station, with wetter value occurs during raining events for SMAP and SMOS and underestimated value for ASCAT. Even the in-situ measurement is similar to the Main station. It means the study area in this research is very homogeneity, the static parameters cannot be the significant influence factor for each station. After checking the Appendix B, for all the station time series plot, except V-section stations, other eight stations show similar in-situ SM dynamic change. Thus, the V-section station may made mistake during the in-situ measurement.